Journal of Pharmacological Sciences 136 (2018) 51–56

Contents lists available at ScienceDirect

Journal of Pharmacological Sciences

journal homepage: www.elsevier.com/locate/jphs

Full paper

Cytotoxic activities and effects of atractylodin and β-eudesmol on the cell cycle arrest and apoptosis on cholangiocarcinoma cell line

Kanawut Kotawong [a], Wanna Chaijaroenkul [a], Phunuch Muhamad [b], Kesara Na-Bangchang [a, *]

[a] Chulabhorn International College of Medicine, Thammasat University, Paholyothin Road, Klonglung, Pathum Thani, 12120, Thailand
[b] Drug Discovery and Development Center, Thammasat University, Paholyothin Road, Klonglung, Pathum Thani, 12120, Thailand

ARTICLE INFO

Article history:
Received 4 March 2017
Received in revised form
1 August 2017
Accepted 8 September 2017
Available online 12 January 2018

Keywords:
Cholangiocarcinoma
Atractylodin
β-Eudesmol
Cytotoxicity
Cell cycle arrest
Cell apoptosis

ABSTRACT

Cholangiocarcinoma (CCA) is the cancer of bile duct with high mortality rate particularly in Thailand. The clinical efficacy of the standard chemotherapeutics remains unsatisfactory, and therefore, discovery and development of the new alternative drugs with high efficacy and tolerability is needed. The aim of the study was to investigate cytotoxic activity as well as the underlying mechanisms through which atractylodin and β-eudesmol exert their activities on CCA cell growth inhibition, cell cycle arrest, and cell apoptosis. Effects of the compounds on cell cytotoxicity, cell cycle arrest, and cell apoptosis were analyzed using MTT assay, BD Cycletest™ Plus DNA kit, and FITC Annexin V Apoptosis Detection Kit I, respectively. The cytotoxic activities of both compounds were concentration- and time-dependent. The IC_{50} [mean (SD)] of atractylodin and β-eudesmol were 41.66 (2.51) and 39.33 (1.15) μg/ml respectively. Both promoted cell cycle arrest at G1 phase, and induced cell apoptosis through activation of caspase-3/7. The highest activity was observed at 48 h of exposure. Results suggest that these mechanisms are at least in part, explain the cell cytotoxic and anti-CCA activity of atractylodin and β-eudesmol shown *in vitro* and *in vivo* models.

© 2018 The Authors. Production and hosting by Elsevier B.V. on behalf of Japanese Pharmacological Society. This is an open access article under the CC BY-NC-ND license (http://creativecommons.org/licenses/by-nc-nd/4.0/).

1. Introduction

Cholangiocarcinoma (CCA) is the cancer of bile duct arising from epithelial cells and develops along the biliary tree. CCA is classified in several types based on anatomical location, microscopic pattern of growth, microscopic feature, and origin cell.[1] In the United States, CCA accounts for 3% of all gastrointestinal cancers with approximately 5000 new cases annually.[2] The highest incidence and mortality rates are reported from Thailand, particularly in the northeastern region of the country. Current standard treatments of CCA with conventional drugs include 5-fluorouracil (5-FU), gemcitabine, and cisplatin, either as single drug or combination therapies.[3,4] Nevertheless, their clinical efficacy remains unsatisfactory, and therefore, discovery and development of the new alternative drugs with high efficacy and tolerability is needed.

The rhizome of *Atractylodes lancea* (*A. lancea*) is used ethnobotanically in China, Japan and Thailand for treatment several diseases or conditions such as rheumatic, digestive disorders, night blindness, influenza, fever, and common cold.[5] Moreover, various studies also demonstrated potential property of the rhizome extract of this plant for treatment of cancers.[6–8] The anticancer potential of the rhizome extract of *A. lancea* against CCA was also reported both *in vitro* and *in vivo* models.[9–13] In the present study, we further investigated the cytotoxic activity as well as the underlying mechanisms through which the two major isolated compounds, *i.e.*, atractylodin (Fig. 1A, 14% of total content) and β-eudesmol (Fig. 1B, 6% of total content) exert their activities on CCA cell growth inhibition, cell cycle arrest, and cell apoptosis.

2. Material and methods

2.1. Cell lines and culture

The CCA cell lines (CL-6 and HUCC-T1), and normal (OUMS) human cell line were used in the study. The CL-6 cell originally isolated from a patient with CCA, was kindly provided by Associate Professor Dr. Adisak Wongkajornsilp, Faculty of Medicine, Siriraj

* Corresponding author.
E-mail address: kesaratmu@yahoo.com (K. Na-Bangchang).
Peer review under responsibility of Japanese Pharmacological Society.

https://doi.org/10.1016/j.jphs.2017.09.033
1347-8613/© 2018 The Authors. Production and hosting by Elsevier B.V. on behalf of Japanese Pharmacological Society. This is an open access article under the CC BY-NC-ND license (http://creativecommons.org/licenses/by-nc-nd/4.0/).

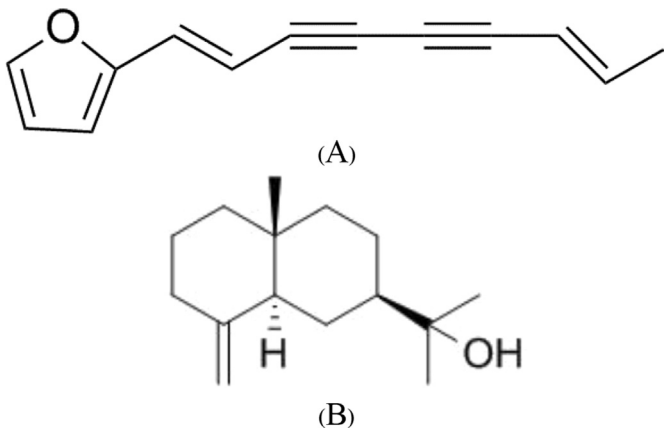

Fig. 1. The chemical structures of atractylodin (A) and β-eudesmol (B).

Hospital, Mahidol University, Thailand. HUCC-T1 and OUMS were purchased from Japanese Collection of Research Bioresources (JCRB) cell bank, Japan. All cell lines were cultured with RPMI 1640 medium (Gibco Co. Ltd., NY, USA) and Dulbecco's Modified Eagle Medium (DMEM: Gibco Co. Ltd., NY, USA), respectively. The culture medium was supplemented with 10% (v/v) heated fetal bovine serum (FBS) and 100 IU/ml of antibiotic-antimycotic solution (Gibco Co. Ltd., NY, USA). All cells were maintained at 37 °C in 5% CO_2 atmosphere and 95% humidity (HERACELL 150i, Thermo scientific, MA, USA).

2.2. Cytotoxic assay

The CCA, HUCC-T1, and OUMS cell lines were treated with varying concentrations (250, 125, 62.5, 31.25, 15.6, 7.8, 3.9, and 1.95 μg/ml) of atractylodin, β-eudesmol, and 5-FU (WAKO, Osaka, Japan) in a 96-well microtiter plate (Corning, NY, USA) for 48 h 5-FU (WAKO, Osaka, Japan) was used as a positive control (concentration range 250–1.95 μg/ml). Effects of all compounds on the survival of all cell lines were determined using MTT assay.[14] Briefly, the cells (CL-6, HUCC-T1, or OUMS) were seeded onto each well of the 96-well microtiter plate (10,000 cells/well) and incubated for 24 h (37 °C, 5% CO_2 atmosphere, and 95% humidity) before exposing to atractylodin, β-eudesmol, or 5-FU. Following 48 h incubation, the MTT reagent (20 μl of 5 mg/ml solution: Sigma Co. Ltd., MO, USA) was added into each well and the plate was further incubated for 4 h. The culture medium of each well was discarded and DMSO (100 μl) was added, and the plate was incubated at 25 °C in the dark room for 15 min. The absorbance was measured at 570 nM (Varioscan Flash, Thermo, Finland).

Cell viability and corresponding IC_{50} (concentration of each compound that produces 50% inhibitory effect on cell growth relative to control) were determined using CalcuSyn™ v2.11 software (Biosoft, Cambridge, UK). The selectivity index (SI) was determined as the ratio of IC_{50} of atractylodin, β-eudesmol, or 5-FU in the OUMS and that in the CCA cell.

2.3. Effect of time on cytotoxic activity of atractylodin and β-eudesmol

To determine the effect of time on the cytotoxic activity of atractylodin and β-eudesmol in CL-6, HUCC-T1, and OUMS cells, the cells were seeded onto a 96-well plate (10,000 cells/well) and incubated for 24 h. Following exposure to atractylodin or β-eudesmol at the IC_{50} concentration of each compound for 12, 24, and 48 h, cell viability was determined using MTT assay as described above.

2.4. Effects of atractylodin and β-eudesmol on cell cycle arrest

The CL-6, HUCC-T1, and OUMS cells were exposed to atractylodin and β-eudesmol at the IC_{25} (concentration of each compound that produces 25% inhibitory effect relative to control) of each compound (20 and 23 μg/ml for atractylodin and β-eudesmol, respectively) for 12, 24, and 48 h and DNA contents were identified by BD Cycletest™ Plus DNA kit (BD biosciences, CA, USA). Briefly, the cells were harvested after the exposure to each compound, washed three times with buffer solution, and cell number was adjusted to 1.0×10^6 cells/ml. Following sequential incubation (10 min each) in the dark room with Solution A (trypsin buffer), Solution B (trysin inhibitor and RNase buffer), and Solution C (PI stain solution), the deoxyribonucleic acid (DNA) content of CL-6 was analyzed by flow cytometry (BD FACSVerse™ flow cytometer, BD, USA). Each study was performed in three independent experiments, triplicate each.

2.5. Effects of atractylodin and β-eudesmol on cell apoptosis and caspase 3/7 activation

The CL-6, HUCC-T1, and OUMS cells were exposed to atractylodin and β-eudesmol at the IC_{25} and IC_{50} concentrations of each compound (IC_{25}: 20 and 23 μg/ml for atractylodin and β-eudesmol, respectively; IC_{50}: 40 and 40 μg/ml for atractylodin and β-eudesmol, respectively) for 12, 24, and 48 h, and cell apoptosis and caspase-3/7 activation was investigated using FITC Annexin V Apoptosi Detection Kit I and CellEvent™ Caspase-3/7 Green Flow Cytometry Assay Kit. Briefly, the cells were harvested after exposure to each compound, washed three times with PBS solution, and cell number was adjusted to 1.0×10^5 cells/ml. The cells were mixed with CellEvent™ Caspase-3/7 Green Detection Reagent and incubated at 37 °C for 30 min in the dark room. Finally, the cells were mixed with SYTOX™ AADvanced™ in DMSO and analyzed by flow cytometry (BD FACSVerse™ flow cytometer, BD, USA). Each study was performed in three independent experiments, triplicate each.

3. Results

3.1. Cytotoxic activity

The IC_{50} [mean (SD)] values of atractylodin in CL-6, HUCC-T1, and OUMS cell lines were 41.66 (2.51), 38.78 (1.07) and 64.33 (2.08) μg/ml, respectively. The corresponding values of the IC_{50} for β-eudesmol were 39.33 (1.15), 35.22 (0.98) and 53.15 (3.90) μg/ml, respectively. The SI values of both compounds for the CL-6 vs. HUCC-T1 cells were 1.54 vs. 1.66 and 1.35 vs. 1.50, respectively.

3.2. Effect of time on cytotoxic activity of atractylodin and β-eudesmol

Both atractylodin and β-eudesmol exhibited time-dependent cytotoxic activity in both CL-6 and HUCC-T1 cells over the exposure period 12–48 h. The IC_{50} [mean (SD)] values of atractylodin following 12, 24, and 48 h exposure of the CL-6 vs. HUCC-T1 cells were 80.33 (4.50) vs. 76.41 (2.22), 66.33 (3.05) vs. 60.20 (2.79), and 41.66 (2.51) vs. 37.00 (1.22) μg/ml, respectively. The corresponding IC_{50} [mean (SD)] values of β-eudesmol were 61.33 (2.51) vs. 58.29 (2.01), 50.00 (2.00) vs. 45.11 (3.02) and 39.33 (1.15), 35.11 (1.09) μg/ml, respectively (Fig. 2A and B).

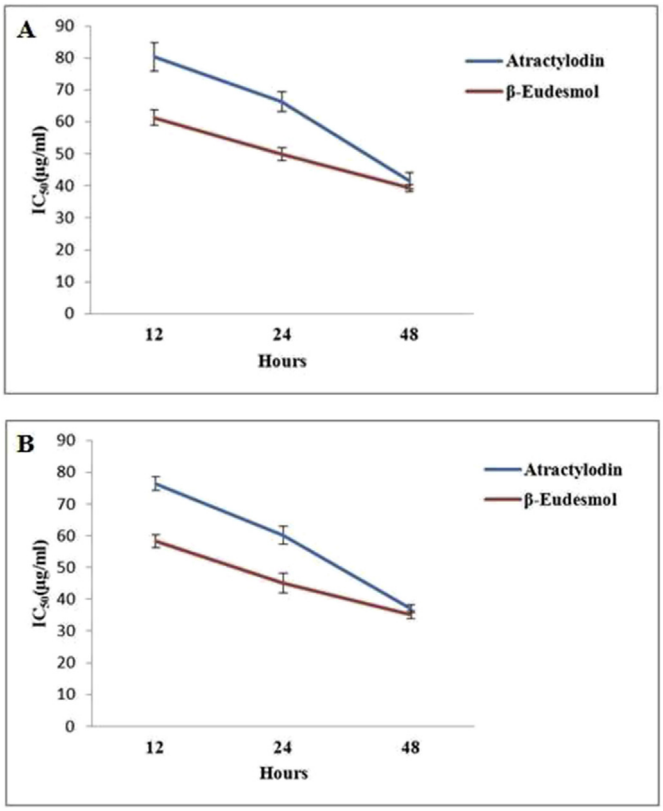

Fig. 2. Time-dependent cytotoxic activities of atractylodin and β-eudesmol over the period 12–48 h in (A) CL-6 cells, and (B) HUCC-T1 cells. Data are presented as percent change of the IC_{50} of each compound at each time point, compared with control (three independent experiments, triplicate each).

3.3. *Effects of atractylodin and β-eudesmol on cell cycle arrest*

The effects of atractylodin and β-eudesmol on CL-6, HUCC-T1, and OUMS cell cycle arrest were investigated for the underlying mechanisms of cytotoxicity of both compounds. After the exposure of the cells to each compound at the IC_{25} for 12, 24, and 48 h, the DNA content of CL-6 was measured by flow cytometry. Both atractylodin (IC_{25}: 20 μg/ml) and β-eudesmol (IC_{25}: 23 μg/ml) significantly induced CL-6 and HUCC-T1 cell cycle arrest at G1 phase. For atractylodin, the DNA contents of G1 phase of CL-6 vs. HUCC-T1 cells [mean (SD)] at 12, 24, and 48 h exposure were increased from baseline to 68.97 (0.29) vs. 72.11 (0.31), 81.51 (0.06) vs. 83.25 (0.12) and 79.55 (1.40) vs. 85.14 (2.02)%, respectively. The corresponding DNA contents following β-eudesmol exposure were 68.67 (3.04) vs. 66.44 (3.32), 69.78 (1.76) vs. 70.12 (1.86) and 75.87 (4.7) vs. 76.46 (3.98) %, respectively (Fig. 3A, B, C, and D). In the control cell (OUMS), both compounds produced no significant effect cell cycle arrest.

3.4. *Effects of atractylodin and β-eudesmol on cell apoptosis*

The effects of atractylodin and β-eudesmol on CL-6, HUCC-T1, and OUMS cell apoptosis were investigated by flow cytometry after staining with Annexin V and propidium iodide. Results showed that both compounds significantly induced cell apoptosis with highest potency at 48 h of exposure. For atractylodin at the concentration of 20 μg/ml (IC_{25}), the mean (SD) Annexin V staining ratio (Annexin V staining of sample: Annexin V staining of control) in CL-6 vs. HUCC-T1 cells following 12, 24 and 48 h exposure were 1.5 (0.19) vs. 1.4 (0.23), 1.47 (0.29) vs. 1.59 (0.30) and 2.59 (0.47) vs. 2.77 (0.52), respectively. At higher concentration of 40 μg/ml (IC_{50}), the annexin V staining ratios were decreased to 1.56 (0.25) vs. 1.69 (0.32), 1.34 (0.39) vs. 1.26 (0.30) and 2.99 (0.14) vs. 2.87 (0.16), respectively. For β-eudesmol at the concentration of 20 μg/ml (IC_{25}), the staining ratios in CL-6 vs. HUCC-T1 cells following 12, 24 and 48 h exposure were 1.39 (0.31) vs. 1.44 (0.28), 0.92 (0.13) vs. 1.10 (0.20) and 1.99 (0.44) vs. 2.01 (0.45), respectively. At higher concentration of 40 μg/ml (IC_{50}), the staining ratios were 1.07 (0.18) vs. 1.05 (0.16), 1.3 (0.3) vs. 1.1 (0.29) and 5.30 (1.44) vs. 4.88 (1.36), respectively. In the control cell (OUMS), both compounds produced no significant effect on cell apoptosis.

To demonstrate mechanisms underlying apoptotic induction, the activities of apoptosis-related proteins in CL-6 and HUCC-T1 treated cells were investigated. The caspase 3/7 activity of both cells following exposure to atractylodin and β-eudesmol were significantly increased compared with untreated control cells. Results suggested that both atractylodin and β-eudesmol enhanced CCA cell apoptosis through caspase-3/7 activation.

4. Discussion

The cell cycle in eukaryotic cells is regulated by expression and sequential activation of cell cycle-dependent cyclins, CDKs, and CDK inhibitors.[15,16] Activation of cell cycle arrest may finally lead to cell apoptosis if unrepaired. Results from the present study indicated that both atractylodin and β-eudesmol significantly induced CL-6 cell cycle arrest at the G1 phase. Several factors are involved in G1 phase cell arrest. The flavonoid cyclin inhibitor, casticin, exerted its anti-inflammatory and anticancer activities *via* inhibiting cyclin D1 and CDK4 through activation of p27 in gall bladder cells, leading to cell cycle arrest at G1 phase.[17] The induction of cell cycle arrest at G1 phase in human ovarian cancer cells by LY294002 was associated with the PI3K/AKT/mTOR pathway.[18] Exposure of linalool, the biologically active compound from Plantaginaceae, to human AML (acute myeloid leukemia) cell line, increased the levels of p16, p21, p27, and p53 proteins, leading to the induction of cancer cell arrest at G1 phase.[19] Atractylodin and β-eudesmol were shown in the present study to induce CCA cell cycle arrest at G1 phase similar to that observed with berberine and sho-saiko-to isolated from *Berberis vulgaris* and combination of seven herbs (*Bupleuri radix, Pinelliae tuber, Scutellariae radix, Zizyphi fructus, Ginseng radix, Glycyrrhizae radix,* and *Zingiberis rhizoma*) in human CCA cell (QBC939) and human hepatocellular carcinoma cell (KIM-1), respectively.[20,21] On the other hand, cell cycle arrest can also be activated at other cell cycle phases. The cytotoxic activity of *Cratoxylum formosum* Dyer on CCA cells was associated with an induction of cell apoptosis and induction of cell cycle arrest at the G2/M phase and downregulation of cyclin A and Cdc25A protein expression. It also potently suppressed the migration and invasion properties of CCA cells which were associated with the suppression of NF-kB and STAT3 nuclear translocation and transcriptional activity, and downregulation of genes involving in cancer progression and metastasis.[22] Moreover, forbesione isolated from *Garcinia hanburyi*, and decitabine, a DNA-hypomethylating agent, induced the cell cycle arrest of CCA cell at S and G2 phase, respectively.[23,24]

Tumorigenesis and metastasis generally involves increased expression of anti-apoptotic, cytoprotective, and cell proliferation-associated genes.[25,26] Cell apoptosis plays an important role in maintaining tissue homeostasis and eliminating unwanted cells in multicellular organisms.[27] Targeting cell apoptosis is therefore one of the promising approaches for cancer chemotherapeutic. This program cell death starts with changing in cell nuclear morphology (chromatin condensation and fragmentation), cell shrinking, plasma membrane blebbing, and apoptotic body formation. Two major signaling pathways are involved in cell apoptosis, *i.e.*, the intrinsic and extrinsic pathways. The Bcl-2, Bax, cytochrome *c*, caspase-3, and

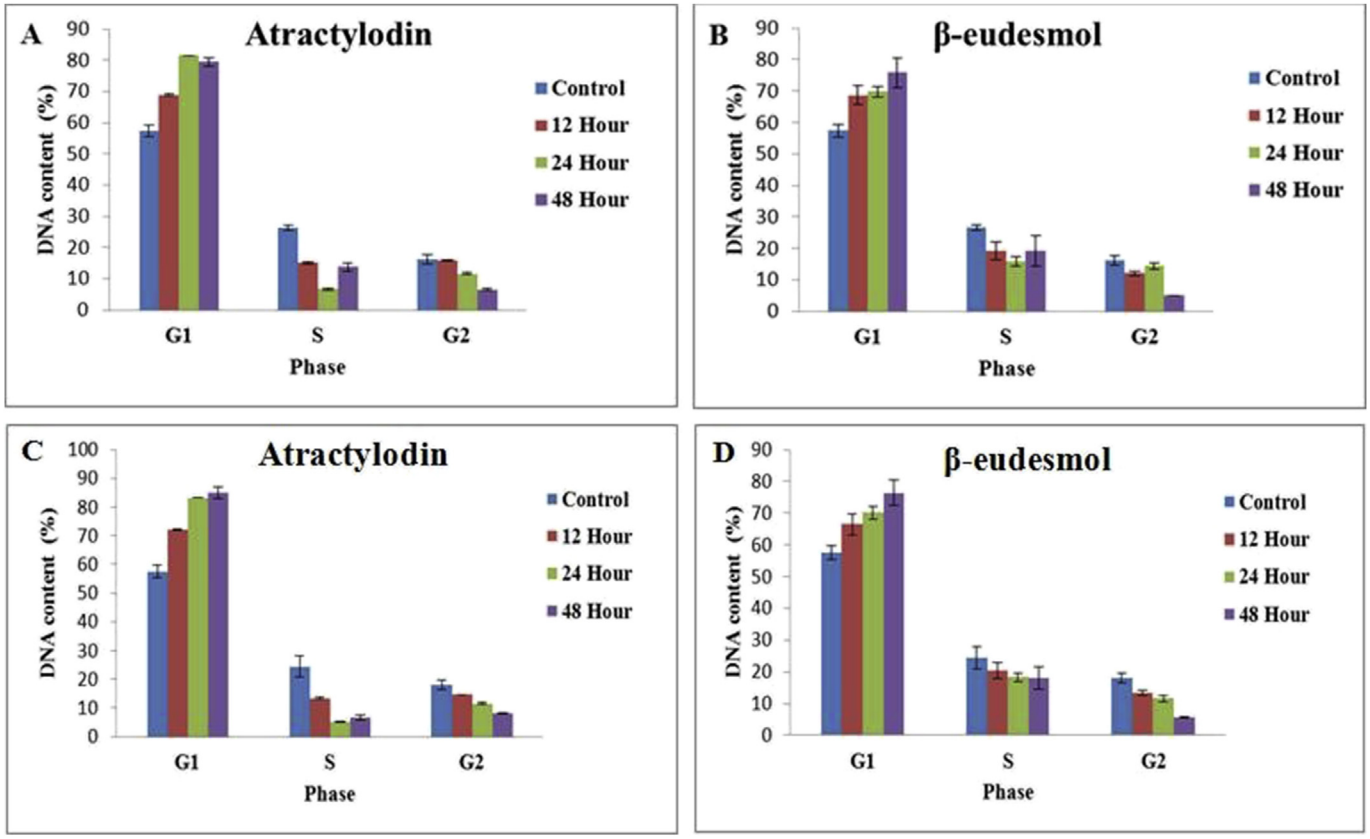

Fig. 3. The DNA content (%) of CL-6 [mean (SD) of three independent experiments, triplicate each] following exposure of (A,B) CL-6 cells and (C,D) HUCC-T1 cells to 20 μg/ml of atractylodin and 23 μg/ml of β-eudesmol (B) for 12, 24, and 48 h.

caspase-9 are involved in the intrinsic pathway (mitochondrial-mediated pathway), whereas CD147, TNF-α, FASL, TRAIL, TRAF2, caspase-8, and caspase-3 are involved in the extrinsic pathway (death receptor pathway).[28–32] Induction of CCA cell apoptosis by several compounds has been demonstrated including ESC-3 (isolated from crocodile bile),[33] mifepristone (a progesterone receptor antagonist),[34] and luteolin (a flavonoid from vegetables and fruits).[35,36] The mechanism of induction of CCA cell apoptosis by ECS-3 and mifepristone is linked to the intrinsic pathway by down-regulation of Bcl-2 and up-regulation of Bax level, whereas that involved in the induction by luteolin is through JAK/STAT3 (janus kinase/signal transducer and activator of transcription signaling pathway).[35] Moreover, targeting phosphatidylinositol 3-kinase/AKT mammalian target of rapamycin (PI3K/AKT/mTOR) pathway by the mTOR inhibitors RAD001 and MK-2206 was shown to significantly inhibited CCA cell proliferation.[37] CCA cell cytotoxicity following treatment with LY294002, a potent inhibitor of PI3K, was shown to be linked with decrease in expression of survivin and Bcl-2 and the increase in caspase-3 levels.[38] *Resina Draconis*, the Chinese herb commonly used to treat coronary heart disease, angina, and acute myocardial infarction, was shown to inhibit CCA cell proliferation and trigger apoptotic cell death through activation of intracellular caspase-8 and poly (ADP-ribose) polymerase. In addition, it significantly downregulated antiapoptotic protein survivin expression and upregulated pro-apoptotic protein Bak expression.[37] The ethanolic extract of *Andrographis paniculata* induced CCA cell cycle arrest at the G0/G1 and G2/M phases resulting in cell apoptosis. The expressions of cyclin-D1, Bcl-2, and the inactive proenzyme form of caspase-3 were reduced by the ethanolic extract of *A. paniculata,* while a proapoptotic protein Bax was increased.[38] The purified compound from *Kaemperia parviflora* Wall. Ex Baker, 5,7,4-trimethoxyflavone (KP.8.10), was shown to exhibit progressive cytotoxic activity on CCA via caspase-3 mitochondrial enzyme activation.[39]

In the present study, the mechanism underlying CCA cell apoptosis induced by atractyodin and β-eudesmol through induction of caspase cascade was initially determined. Caspases are intracellular cysteine protease enzymes that play major role in apoptotic mechanism and caspase-3/7 is the final step in both the intrinsic or extrinsic pathways of apoptosis.[40] Both compounds significantly activated caspase-3/7 compared to untreated control cells, suggesting the potentiating cytotoxic effect of β-eudesmol on CCA cells in the final stage of apoptosis. In a previous study, β-eudesmol was shown to suppress the angiogenesis, proliferation, and growth of several cancers including CCA.[6,11,41] For atractylodin, its inhibitory activity on CCA cells was reported to be through inhibition of the pro-inflammatory cytokine interleukin-6 (IL-6).[42] The mechanism was *via* blocking NPM-ALK activation and MAPKs.[43] Recently, inhibitory effect of β-eudesmol on CCA cell growth was shown to be associated with suppression of heme oxygenase-1 (HO-1) production, STAT1/3 activation, and NF-κB.[44] HO-1 is a critical cytoprotective enzyme known to promote anti-apoptotic activities and chemotherapeutic resistance in several types of tumor cells.[45] JAK/STAT3 signaling is constitutively activated in CCA and represents an important target for treatment of this disease.[46] Inhibition of STAT3 signaling by sorafenib, a multi-kinase inhibitor was found to sensitize CCA cells to tumor necrosis factor-related apoptosis-inducing ligand-mediated apoptosis and suppress CCA tumor growth.[47] Inactivation of JAK/STAT3 signaling in CCA was shown to mediate the cytotoxic effects of the flavonoids

quercetin and epigallocatechin-3-gallate (EGCG) as well as matrine, the alkaloid isolated from traditional Chinese herb *Sophora flavescens* ait. in CCA cells.[48,49]

In conclusion, results from this preliminary present suggest that the two major active constituents of *A. lancea* rhizomes, atractylodin and β-eudesmol, play important role in anticancer activity observed in various *in vivo* models in dimethylnitrosamine/CCA-induced hamsters and CCA-xenografted nude mice.[10–13] Promotion of cell cycle arrest at the G1 phase together with induction of cell apoptosis are involved in their cytotoxic activities. The mechanisms through which β-eudesmol and atractylodin exert their inducing activity on cell cycle arrest and apoptosis in CCA cells, including confirmation in animal model are being investigated in details.

Conflict of interest

Authors declare no conflict of interest.

Acknowledgements

The study was supported by Chulabhorn International College of Medicine (CICM) of Thammasat University, Center of Excellence in Pharmacology and Molecular Biology of Malaria and Cholangiocarcinoma of Thammasat University (1/2556), National Research Council of Thailand (NRCT) (042/2558 and 49/2559) and National Research University Project of Thailand (NRU) (6/2559), Office of Higher Education Commission of Thailand. KK received supports from Thammasat University for Ph.D. program and Thammasat University Research Fund under the TU Research Scholar (2560).

References

1. Cardinale V, Bragazzi MC, Carpino G, et al. Cholangiocarcinoma: increasing burden of classifications. *Hepatobiliary Surg Nutr*. 2013;2(5):272–280.
2. Gatto M, Alvaro D. New insights on cholangiocarcinoma. *World J Gastrointest Oncol*. 2010;2(3):136–145.
3. Ebata T, Ercolani G, Alvaro D, Ribero D, Di Tommaso L, Valle JW. Current status on cholangiocarcinoma and gallbladder cancer. *Liver Cancer*. 2016;6(1):59–65.
4. Giuliani F, Gebbia V, Maiello E, Borsellino N, Bajardi E, Colucci G. Gemcitabine and cisplatin for inoperable and/or metastatic biliary tree carcinomas: a multicenter phase II study of the Gruppo Oncologico dell'Italia Meridionale (GOIM). *Ann Oncol Off J Eur Soc Med Oncol ESMO*. 2006;17(Suppl 7):vii73–vii77.
5. Koonrungsesomboon N, Na-Bangchang K, Karbwang J. Therapeutic potential and pharmacological activities of *Atractylodes lancea* (Thunb.) DC. *Asian Pac J Trop Med*. 2014;7(6):421–428.
6. Ma EL, Li YC, Tsuneki H, et al. Beta-eudesmol suppresses tumour growth through inhibition of tumour neovascularisation and tumour cell proliferation. *J Asian Nat Prod Res*. 2008;10(1–2):159–167.
7. Masuda Y, Kadokura T, Ishii M, Takada K, Kitajima J. Hinesol, a compound isolated from the essential oils of *Atractylodes lancea* rhizome, inhibits cell growth and induces apoptosis in human leukemia HL-60 cells. *J Nat Med*. 2015;69(3):332–339.
8. Zhao M, Wang Q, Ouyang Z, et al. Selective fraction of *Atractylodes lancea* (Thunb.) DC. and its growth inhibitory effect on human gastric cancer cells. *Cytotechnology*. 2014;66(2):201–208.
9. Mahavorasirikul W, Viyanant V, Chaijaroenkul W, Itharat A, Na-Bangchang K. Cytotoxic activity of Thai medicinal plants against human cholangiocarcinoma, laryngeal and hepatocarcinoma cells in vitro. *BMC Complement Altern Med*. 2010;10:55.
10. Plengsuriyakarn T, Eursitthichai V, Labbunruang N, et al. Ultrasonography as a tool for monitoring the development and progression of cholangiocarcinoma in *Opisthorchis viverrini*/dimethylnitrosamine-induced hamsters. *Asian Pac J Cancer Prev APJCP*. 2012;13(1):87–90.
11. Plengsuriyakarn T, Karbwang J, Na-Bangchang K. Anticancer activity using positron emission tomography-computed tomography and pharmacokinetics of beta-eudesmol in human cholangiocarcinoma xenografted nude mouse model. *Clin Exp Pharmacol Physiol*. 2015;42(3):293–304.
12. Plengsuriyakarn T, Matsuda N, Karbwang J, Viyanant V, Hirayama K, Na-Bangchang K. Anticancer activity of *Atractylodes lancea* (Thunb.) DC in a hamster model and application of PET-CT for early detection and monitoring progression of cholangiocarcinoma. *Asian Pac J Cancer Prev APJCP*. 2015;16(15):6279–6284.
13. Plengsuriyakarn T, Viyanant V, Eursitthichai V, et al. Anticancer activities against cholangiocarcinoma, toxicity and pharmacological activities of Thai medicinal plants in animal models. *BMC Complement Altern Med*. 2012;12:23.
14. Mosmann T. Rapid colorimetric assay for cellular growth and survival: application to proliferation and cytotoxicity assays. *J Immunol Methods*. 1983;65(1–2):55–63.
15. Lim S, Kaldis P. Cdks, cyclins and CKIs: roles beyond cell cycle regulation. *Development (Cambridge, England)*. 2013;140(15):3079–3093.
16. Lavecchia A, Di Giovanni C, Novellino E. CDC25 phosphatase inhibitors: an update. *Mini Rev Med Chem*. 2012;12(1):62–73.
17. Song XL, Zhang YJ, Wang XF, et al. Casticin induces apoptosis and G0/G1 cell cycle arrest in gallbladder cancer cells. *Cancer Cell Int*. 2017;17:9.
18. Gao N, Flynn DC, Zhang Z, et al. G1 cell cycle progression and the expression of G1 cyclins are regulated by PI3K/AKT/mTOR/p70S6K1 signaling in human ovarian cancer cells. *Am J Physiol Cell Physiol*. 2004;287(2):C281–C291.
19. Chang MY, Shieh DE, Chen CC, Yeh CS, Dong HP. Linalool induces cell cycle arrest and apoptosis in leukemia cells and cervical cancer cells through CDKIs. *Int J Mol Sci*. 2015;16(12):28169–28179.
20. He W, Wang B, Zhuang Y, Shao D, Sun K, Chen J. Berberine inhibits growth and induces G1 arrest and apoptosis in human cholangiocarcinoma QBC939 cells. *J Pharmacol Sci*. 2012;119(4):341–348.
21. Yano H, Mizoguchi A, Fukuda K, et al. The herbal medicine sho-saiko-to inhibits proliferation of cancer cell lines by inducing apoptosis and arrest at the G0/G1 phase. *Cancer Res*. 1994;54(2):448–454.
22. Senggunprai L, Thammaniwit W, Kukongviriyapan V, Prawan A, Kaewseejan N, Siriamornpun S. *Cratoxylum formosum* extracts inhibit growth and metastasis of cholangiocarcinoma cells by modulating the NF-kappaB and STAT3 pathways. *Nutr Cancer*. 2016;68(2):328–341.
23. Boueroy P, Hahnvajanawong C, Boonmars T, et al. Antitumor effect of forbesione isolated from *Garcinia hanburyi* on cholangiocarcinoma in vitro and in vivo. *Oncol Lett*. 2016;12(6):4685–4698.
24. Wang B, Li H, Yang R, Zhou S, Zou S. Decitabine inhibits the cell growth of cholangiocarcinoma in cultured cell lines and mouse xenografts. *Oncol Lett*. 2014;8(5):1919–1924.
25. Zhao S, Yao D, Chen J, Ding N, Ren F. MiR-20a promotes cervical cancer proliferation and metastasis in vitro and in vivo. *PLoS One*. 2015;10(3), e0120905.
26. Chieng CK, Say YH. Cellular prion protein contributes to LS 174T colon cancer cell carcinogenesis by increasing invasiveness and resistance against doxorubicin-induced apoptosis. *Tumour Biol J Int Soc Oncodev Biol Med*. 2015;36(10):8107–8120.
27. Elmore S. Apoptosis: a review of programmed cell death. *Toxicol Pathol*. 2007;35(4):495–516.
28. Karimian H, Arya A, Fadaeinasab M, et al. *Kelussia odoratissima* Mozaff. activates intrinsic pathway of apoptosis in breast cancer cells associated with S phase cell cycle arrest via involvement of p21/p27 in vitro and in vivo. *Drug Des Dev Ther*. 2017;11:337–350.
29. Zeriouh W, Nani A, Belarbi M, et al. Phenolic extract from oleaster (*Olea europaea var. Sylvestris*) leaves reduces colon cancer growth and induces caspase-dependent apoptosis in colon cancer cells via the mitochondrial apoptotic pathway. *PLoS One*. 2017;12(2), e0170823.
30. Wang C, Fok KL, Cai Z, Chen H, Chan HC. CD147 regulates extrinsic apoptosis in spermatocytes by modulating NFkappaB signaling pathways. *Oncotarget*. 2017;8(2):3132–3143.
31. Mughal MJ, Xi P, Yi Z, Jing F. Aflatoxin B1 invokes apoptosis via death receptor pathway in hepatocytes. *Oncotarget*. 2017;8(5):8239–8249.
32. Yu X, Ling J, Liu X, et al. Cordycepin induces autophagy-mediated c-FLIPL degradation and leads to apoptosis in human non-small cell lung cancer cells. *Oncotarget*. 2017;8(4):6691–6699.
33. Song W, Shen DY, Kang JH, et al. Apoptosis of human cholangiocarcinoma cells induced by ESC-3 from *Crocodylus siamensis* bile. *World J Gastroenterol WJG*. 2012;18(7):704–711.
34. Sun QL, Zhang XG, Xing QT, et al. A study of mifepristone/IFN-gamma-induced apoptosis of human cholangiocarcinoma cell line FRH-0201 in vitro. *Onco-Targets Ther*. 2012;5:335–342.
35. Aneknan P, Kukongviriyapan V, Prawan A, Kongpetch S, Sripa B, Senggunprai L. Luteolin arrests cell cycling, induces apoptosis and inhibits the JAK/STAT3 pathway in human cholangiocarcinoma cells. *Asian Pac J Cancer Prev APJCP*. 2014;15(12):5071–5076.
36. Lopez-Lazaro M. Distribution and biological activities of the flavonoid luteolin. *Mini Rev Med Chem*. 2009;9(1):31–59.
37. Wen F, Zhao X, Zhao Y, Lu Z, Guo Q. The anticancer effects of Resina Draconis extract on cholangiocarcinoma. *Tumour Biol J Int Soc Oncodev Biol Med*. 2016;37(11):15203–15210.
38. Suriyo T, Pholphana N, Rangkadilok N, Thiantanawat A, Watcharasit P, Satayavivad J. Andrographis paniculata extracts and major constituent diterpenoids inhibit growth of intrahepatic cholangiocarcinoma cells by inducing cell cycle arrest and apoptosis. *Planta Med*. 2014;80(7):533–543.
39. Leardkamolkarn V, Tiamyuyen S, Sripanidkulchai BO. Pharmacological activity of *Kaempferia parviflora* extract against human bile duct cancer cell lines. *Asian Pac J Cancer Prev APJCP*. 2009;10(4):695–698.
40. McIlwain DR, Berger T, Mak TW. Caspase functions in cell death and disease. *Cold Spring Harb Perspect Biol*. 2013;5(4), a008656.
41. Tsuneki H, Ma EL, Kobayashi S, et al. Antiangiogenic activity of beta-eudesmol in vitro and in vivo. *Eur J Pharmacol*. 2005;512(2–3):105–115.

42. Wehbe H, Henson R, Meng F, Mize-Berge J, Patel T. Interleukin-6 contributes to growth in cholangiocarcinoma cells by aberrant promoter methylation and gene expression. *Cancer Res*. 2006;66(21):10517–10524.
43. Chae HS, Kim YM, Chin YW. Atractylodin inhibits Interleukin-6 by blocking NPM-ALK activation and MAPKs in HMC-1. *Molecules*. 2016;21(9).
44. Mathema VB, Chaijaroenkul W, Karbwang J, Na-Bangchang K. Growth inhibitory effect of beta-eudesmol on cholangiocarcinoma cells and its potential suppressive effect on heme oxygenase-1 production, STAT1/3 activation, and NF-kappaB downregulation. *Clin Exp Pharmacol Physiol*. 2017;44(11):1145–1154.
45. Otterbein LE, Soares MP, Yamashita K, Bach FH. Heme oxygenase-1: unleashing the protective properties of heme. *Trends Immunol*. 2003;24(8):449–455.
46. Heits N, Heinze T, Bernsmeier A, et al. Influence of mTOR-inhibitors and mycophenolic acid on human cholangiocellular carcinoma and cancer associated fibroblasts. *BMC Cancer*. 2016;16:322.
47. Blechacz BR, Smoot RL, Bronk SF, Werneburg NW, Sirica AE, Gores GJ. Sorafenib inhibits signal transducer and activator of transcription-3 signaling in cholangiocarcinoma cells by activating the phosphatase shatterproof 2. *Hepatology*. 2009;50(6):1861–1870.
48. Senggunprai L, Kukongviriyapan V, Prawan A, Kukongviriyapan U. Quercetin and EGCG exhibit chemopreventive effects in cholangiocarcinoma cells via suppression of JAK/STAT signaling pathway. *Phytother Res PTR*. 2014;28(6):841–848.
49. Yang N, Han F, Cui H, et al. Matrine suppresses proliferation and induces apoptosis in human cholangiocarcinoma cells through suppression of JAK2/STAT3 signaling. *Pharmacol Rep PR*. 2015;67(2):388–393.

Journal of Pharmacological Sciences 136 (2018) 57–65

Contents lists available at ScienceDirect

Journal of Pharmacological Sciences

journal homepage: www.elsevier.com/locate/jphs

Full paper

The effect of ethanol extract of *Glycyrrhiza uralensis* on the voltage-gated sodium channel subtype 1.4

Guangwei Zhu [a, *], Shengjun Ma [b], Xiwen Li [a], Peng Zhang [a], Lin Tang [c], Lijuan Cao [c], Aoxue Liu [d], Toru Sugita [e], Takehisa Tomoda [e]

[a] Institute of Chinese Materia Medica, China Academy of Chinese Medicinal Sciences, Beijing 100700, China
[b] School of Food Sciences and Pharmacy, Xinjiang Agriculture University, Urumqi, 830052, China
[c] China Medico Corporation, Tianjin, 300301, China
[d] School of Chinese Materia, Beijing University of Chinese Medicine, Beijing, 100102, China
[e] Tsmuura & Co., Tokyo, 107-8521, Japan

ARTICLE INFO

Article history:
Received 20 September 2017
Received in revised form
7 November 2017
Accepted 21 November 2017
Available online 1 December 2017

Keywords:
Glycyrrhiza uralensis (*G. uralensis*)
Skeletal muscle
Gastrocnemius spasm
Nav1.4 voltage-gated sodium channels (VGSCs)
Patch-clamp

ABSTRACT

To investigate the inhibitory effect of *Glycyrrhiza uralensis* (*G. uralensis*) and its monomeric compounds on Nav1.4 voltage-gated sodium channels (VGSCs) and analyze the relationship between the content of its marker compounds and the inhibitory rate. Based on this study, we found that 4 mg/ml ethanol extract of *G. uralensis* at 30%, 50%, 70% and 90% (v/v) exhibited 77.00 ± 0.03%, 34.75 ± 0.09%, 100.00 ± 0.01% and 2.00 ± 0.01% inhibitory rates on $I_{Nav}1.4$ respectively, and 8 mg/ml ethanol extract of *G. uralensis* at 30%, 50%, 70% and 90% (v/v) exhibited 99.00 ± 0.01%, 97.10 ± 0.02%, 100.00 ± 0.01% and 17.00 ± 0.04% inhibitory rates on $I_{Nav}1.4$ respectively. Isoliquiritigenin, echinatin, liquiritin and glycyrrhizic acid exhibited higher inhibitory rates of 39.98 ± 4.55%, 33.20 ± 1.61%, 22.62 ± 0.30% and 20.54 ± 4.82% respectively. However, liquiritigenin, formononetin, neoisoliquiritin and glycyrrhetinic acid exhibited lower inhibitory rates of less than 20%. Further, liquiritin apioside, isoliquiritin and neoliquiritin exhibited almost no effect on $I_{Nav}1.4$. These findings showed that glycyrrhizic acid reached a maximum concentration of 49.15 μg/ml, while echinatin had the lowest concentration. The ethanol extract of *G. uralensis* has significant inhibitory effects on Nav1.4 VGSCs. This may be an important mechanism in the treatment of gastrocnemius spasm and could guide further research regarding material basis and mechanism of the treatment of gastrocnemius spasm with peony and licorice decoction.

© 2018 The Authors. Production and hosting by Elsevier B.V. on behalf of Japanese Pharmacological Society. This is an open access article under the CC BY-NC-ND license (http://creativecommons.org/licenses/by-nc-nd/4.0/).

1. Introduction

VGSCs are important since they are responsible for the initiation and propagation of action potentials in the nerve, heart, and muscles.[1] VGSCs are composed of an α-subunit, which forms a Na^+ conducting pore, and a β-subunit, which acts as a modulator for the biophysical properties of the channel. So far, 9 different α-subunits (Nav1.1~1.9) and 4 different β-subunits (β1~β4) have been identified in mammalian systems.[2] However, Nav1.4 can be primarily observed in skeletal muscles.[3]

The expression of Nav1.4 is essentially in the skeletal muscle. Mutations in the SCN4A gene encoding the human skeletal muscle Nav1.4 channel have been proven to cause five different skeletal muscle disorders, including potassium-aggravated myotonia (PAM), paramyotonia congenita (PMC), hyperkalemic periodicparalysis (HyperPP), hypokalemic periodic paralysis (HypoPP), and a form of congenital myasthenic syndrome (CMS).[4,5] Thus, this channel is considered a target for the treatment of abnormal muscle contractility, spasm and paralysis.[6]

The gastrocnemius muscle is a typical skeletal muscle tissue; it is frequently used to study the motor system because it is an important compound of the motor system.[7] Gastrocnemius muscle lesions can lead to many unexpected consequences, such as gastrocnemius spasm, which is called calf cramp in Traditional

* Corresponding author.
E-mail addresses: gwzhu@icmm.ac.cn (G. Zhu), wlmqmsj@sina.com (S. Ma), xwli@icmm.ac.cn (X. Li), pzhang@icmm.ac.cn (P. Zhang), tanglin@linmura.com.cn (L. Tang), caolijuan@linmura.com.cn (L. Cao), 20150931764@bucm.edu.cn (A. Liu), sugita_tooru@mail.tsumura.co.jp (T. Sugita), tomoda_takehisa@mail.tsumura.co.jp (T. Tomoda).

Peer review under responsibility of Japanese Pharmacological Society.

https://doi.org/10.1016/j.jphs.2017.11.008
1347-8613/© 2018 The Authors. Production and hosting by Elsevier B.V. on behalf of Japanese Pharmacological Society. This is an open access article under the CC BY-NC-ND license (http://creativecommons.org/licenses/by-nc-nd/4.0/).

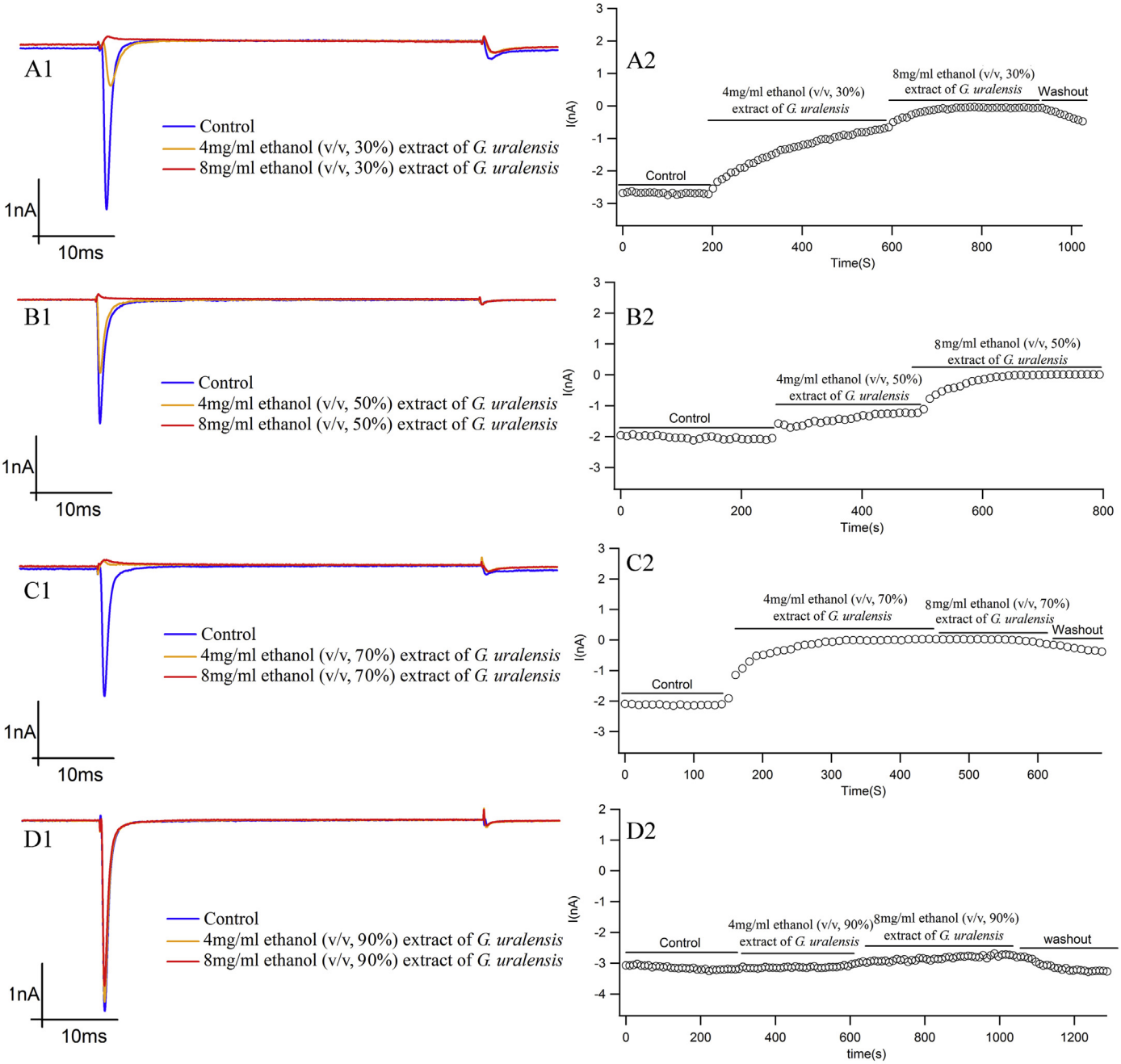
A1
Control
4mg/ml ethanol (v/v, 30%) extract of G. uralensis
8mg/ml ethanol (v/v, 30%) extract of G. uralensis
1nA
10ms
A2
I(nA)
Control
4mg/ml ethanol (v/v, 30%) extract of G. uralensis
8mg/ml ethanol (v/v, 30%) extract of G. uralensis
Washout
Time(S)
B1
Control
4mg/ml ethanol (v/v, 50%) extract of G. uralensis
8mg/ml ethanol (v/v, 50%) extract of G. uralensis
1nA
10ms
B2
I(nA)
Control
4mg/ml ethanol (v/v, 50%) extract of G. uralensis
8mg/ml ethanol (v/v, 50%) extract of G. uralensis
Time(s)
C1
Control
4mg/ml ethanol (v/v, 70%) extract of G. uralensis
8mg/ml ethanol (v/v, 70%) extract of G. uralensis
1nA
10ms
C2
I(nA)
Control
4mg/ml ethanol (v/v, 70%) extract of G. uralensis
8mg/ml ethanol (v/v, 70%) extract of G. uralensis
Washout
Time(S)
D1
Control
4mg/ml ethanol (v/v, 90%) extract of G. uralensis
8mg/ml ethanol (v/v, 90%) extract of G. uralensis
1nA
10ms
D2
I(nA)
Control
4mg/ml ethanol (v/v, 90%) extract of G. uralensis
8mg/ml ethanol (v/v, 90%) extract of G. uralensis
washout
time(s)

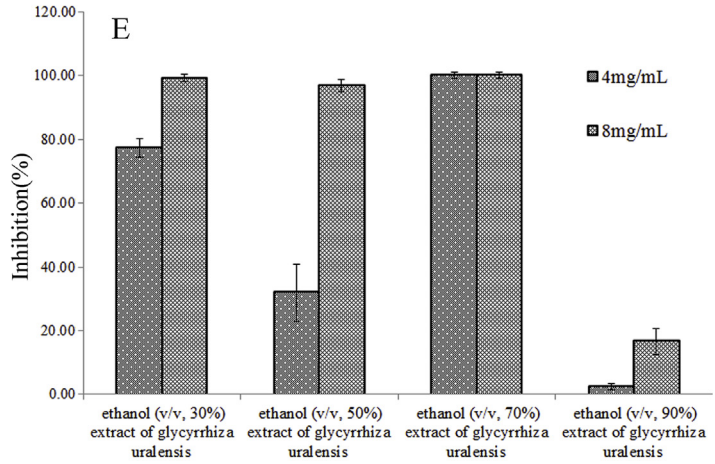
E
Inhibition(%)
4mg/mL
8mg/mL
ethanol (v/v, 30%) extract of glycyrrhiza uralensis
ethanol (v/v, 50%) extract of glycyrrhiza uralensis
ethanol (v/v, 70%) extract of glycyrrhiza uralensis
ethanol (v/v, 90%) extract of glycyrrhiza uralensis

Chinese Medicine. Also, it is one of the most common types of painful spasms.[8] There are many causes of spasticity in the gastrocnemius muscle. One of the most convincing explanation is the VGSCs theory, which holds that the mutation of Nav1.4, an α-subunit of the VGSCs encoded by the SCN4A gene, can lead to a fast inactivation of sodium channel after it opens and add steady current to the interior, resulting in constant muscle depolarization and excessive muscle fiber stimulation, and eventually causing muscle spasms.[9]

Peony and licorice decoction is a traditional Chinese medicine. It has the effects of harmonizing the liver and spleen as well as relieving spasm and pain. It also has a considerable therapeutic effect on gastrocnemius spasm and is a classic prescription for the treatment of gastrocnemius spasm.[10,11] In ancient China, it was used in clinical applications for thousands of years. Modern research shows that peony and licorice decoction has the function of relaxing muscle tissue and relaxing the uterine smooth muscle.[12] It also has a considerable therapeutic effect on painful muscle spasm caused by diabetic neuropathy and lumbar spinal stenosis, and muscle spasticity in dialysis patients.[13] Research have confirmed that the analgesic effect of peony and licorice decoction is mainly attributed to peony, and the basis of the analgesic substance is the total glucoside content of peony, while the antispasmodic effect of peony and licorice decoction is mainly attributed to licorice (*Glycyrrhiza uralensis*), and the basis of the spasmolytic substance is the total glucoside of *G. uralensis* (such as liquiritin, echinatin, isoliquiritigenin, etc.) and the triterpenoid saponin content (such as glycyrrhizic acid, etc.). Experiments have shown that all the compounds mentioned above have antispasmodic effects, and isoliquiritigenin has the strongest antispasmodic effect.

In summary, based on the conclusions above, we speculate that the active substances in *G. uralensis* play an antispasmodic role by inhibiting the Nav1.4 VGSCs. However, there is little or no information about whether *G. uralensis* can block the Nav1.4 VGSCs, which are expressed in skeletal muscles, or not. In this study, we investigated the effects of 4 mg/ml and 8 mg/ml ethanol (30%, 50%, 70% and 90%, v/v) extract of *G. uralensis* on human Nav1.4 VGSCs, which are stably expressed in CHO cells. Additionally, by using UPLC-DAD method, we determined the four marker compounds of *G. uralensis* in order to study the material basis and mechanism of the treatment of gastrocnemius spasm with peony and licorice decoction.

2. Materials and methods

2.1. Drugs, chemicals and reagents

Medicinal materials, which were cultivated for three years, were purchased from Aksu of Xinjiang Uygur Autonomous Region, and were identified as *G. uralensis* Fisch.

The reference compounds of glycyrrhizic acid (purity≥98%, No. 150407), liquiritin (purity≥98%, No. 151013), isoliquiritin (purity≥98%, No. 150714), liquiritigenin (purity≥98%, No. 150511), isoliquiritigenin (purity≥98%, No. 141020), echinatin (purity≥98%, No. 160417), formononetin (purity≥98%, No. 160821), neo-isoliquiritin (purity≥98%, No. 150913), glycyrrhetinic acid (purity≥98%, No. 150723), liquiritin apioside(purity≥98%, No. 160408) and neoliquiritin (purity≥98%, No. 150819)were purchased from Chengdu Pufeide Biotech Co., Ltd. of China (Chengdu, China).

The extracellular solution was of the following composition: 140 mM NaCl, 40 mM tetraethylammonium-Cl, 4 mM KCl, 1 mM $MgCl_2$, 2 mM $CaCl_2$, 5 mM D-Glucose monohydrate and 10 mM HEPES and was adjusted to pH = 7.4 with NaOH. The internal pipette solution was of the following composition: 145 mM $CsCl_2$, 0.1 mM $CaCl_2$, 2 mM $MgCl_2$, 10 mM NaCl, 0.5 mM Na2-GTP, 2 mM Mg-ATP, 1.1 mM EGTA and 10 mM HEPES and was adjusted to pH 7.2 with CsOH.

2.2. Cell culture

Recombinant voltage-gated sodium channel subtype 1.4 alpha subunit (SCN4A) was expressed in CHO cells. The SCN4A cDNA was strictly similar to GenBank accession number NM_000334.4. Cells expressing channels were cultured in F12 medium supplemented with 10% FBS and 0.8 mg/ml G418 in culture flasks. Cells grew in a humidified incubator at 37 °C under 5% carbon dioxide. For patch clamp experiment, seed 3×10^3 cells into 24-well plate (final medium volume: 500 μl) with 1 coverslip in each well and test 18 h after incubation at 37 °C under 5% carbon dioxide.

2.3. Stable expression of human Nav1.4 in CHO cells

Nav1.4 cDNA (cDNA strictly similar to GenBank accession number: NM_000334.4) was subcloned into pCDNA3.1vector (Thermo Fisher Scientific). This vector contains a CMV promoter and a SV40 promoter, which drive the expression of the inserted target cDNA and geneticin-resistant gene, respectively. The CHO-K1 cells were transfected with this construct using Lipofectamine 2000 Transfection Reagent purchased from Thermo Fisher Scientific After transfection, allow cells to grow and to express the protein for antibiotic resistance under nonselective conditions.

48 h post-transfection, remove medium and rinse the cells once with PBS and detach the adherent cells using TrypL Express solution (Gibco). The cells were harvested using HAM'S F12 culture medium (HyClone) supplemented with 10% fetal bovine serum (Gibco) and 1.6 mg/ml antibiotic pretested for the host cell. Plate cells in a 96-well plate with no more than two cells in each wells. It is important to thoroughly suspend cells before seeding, but avoid harsh treatment by frequent pipetting. Incubate cells under standard conditions and feed cells after two weeks with fresh selection medium. The host cell was also prepared in parallel as null control. Cell clones were test as soon as cells in the non-transfected control wells have completely died.

Once identify the resistant clones, expand the cells culture into 6-well plate and assay for the expression of gene of interest by using manual patch clamp test. Positive clones were expended and cryopreserved timely, stable cell line was maintained at half concentration of antibiotic routinely.

2.4. Instrumentations

The instruments used in this study include gene sequencer (3730, Applied Biosystems, USA), PCR instrument (2720, Applied Biosystems, USA), micropipette puller (P97, Sutter Instruments, USA), capillary glass tube (BF150-86-10, Sutter Instruments, USA), microscope (IX71, Olympus, Japan), microelectrode manipulator (MP285, Sutter Instruments, USA), amplifier (EPC10, HEKA, Germany), electronic analytical balance (BP110S, Sartorius, Germany).

Fig. 1. Effect of ethanol extract of *G. uralensis* on I_{Nav}1.4. *A1, B1, C1, D1)* I_{Nav}1.4 recorded from CHO cells expressing human Nav1.4 VGSCs before *G. uralensis* treatment (control), under treatment, and after washing out *G. uralensis*. *A2, B2, C2, D2)* Time course of inhibition of the I_{Nav}1.4 evoked by depolarization from a holding potential of −120 mV to a test potential of +10 mV by sequential exposure to *G. uralensis*. The amplitude of the I_{Nav}1.4 was measured every 20 s. The ordinate shows the I_{Nav}1.4 relative to the control current during exposure of the cell to *G. uralensis* and during wash-out of *G. uralensis*. *E)* The inhibitory effect of ethanol extract of *G. uralensis* on I_{Nav}1.4. *A1, A2*: 4 mg/ml and 8 mg/ml ethanol extract of *G. uralensis* at 30% (v/v). *B1, B2*: 4 mg/ml and 8 mg/ml ethanol extract of *G. uralensis* at 50% (v/v). C1, C2: 4 mg/ml and 8 mg/ml ethanol extract of *G. uralensis* at 70% (v/v). *D1, D2:* 4 mg/ml and 8 mg/ml ethanol extract of *G. uralensis* at 90% (v/v). *E:* 4 mg/ml and 8 mg/ml ethanol extract of *G. uralensis* at 30%, 50%, 70% and 90% (v/v).

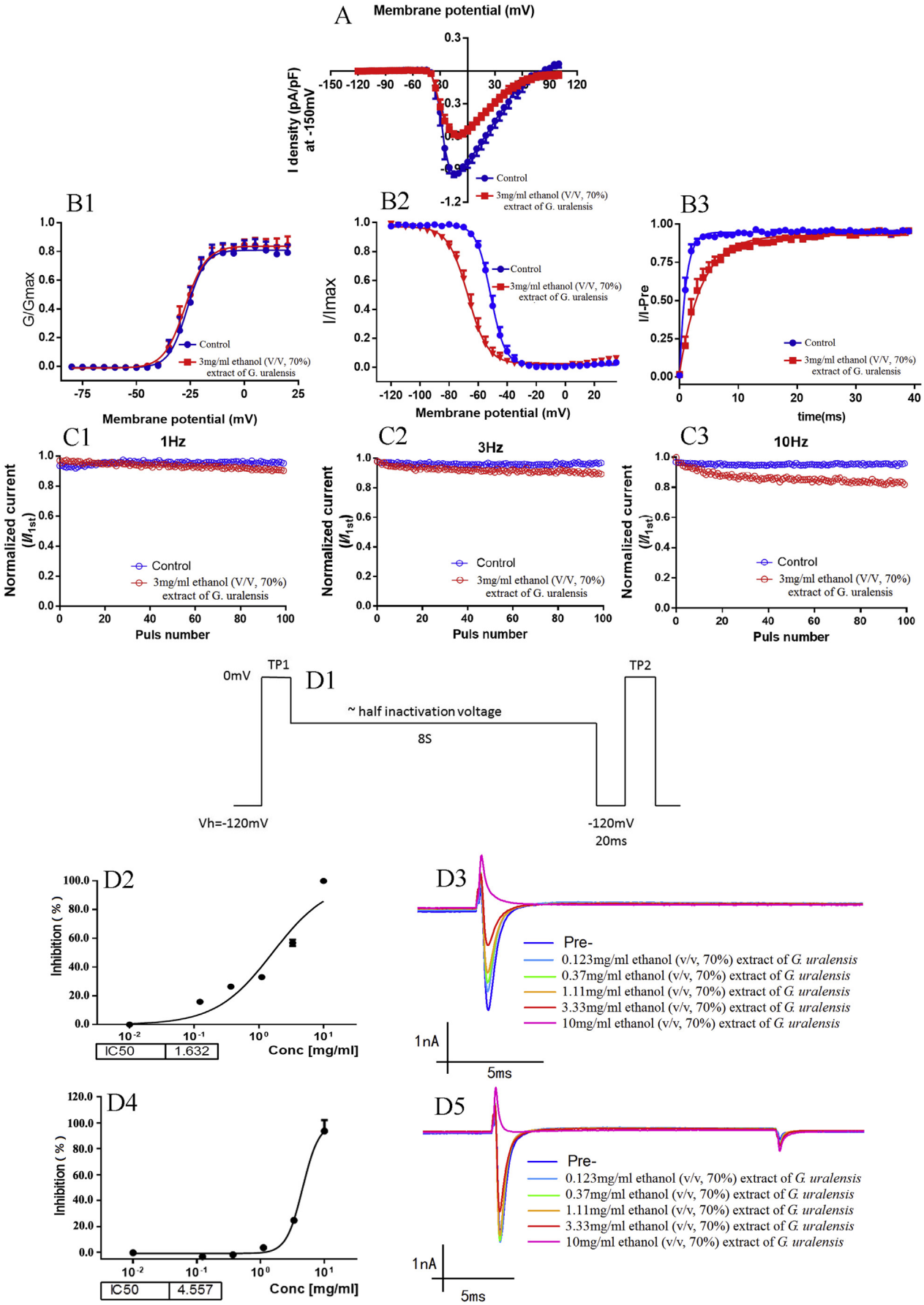
A
Membrane potential (mV)
I density (pA/pF) at -150mV
Control
3mg/ml ethanol (V/V, 70%) extract of G. uralensis
B1
G/Gmax
Membrane potential (mV)
B2
I/Imax
Membrane potential (mV)
B3
I/I-Pre
time(ms)
C1
1Hz
C2
3Hz
C3
10Hz
Normalized current (I/I_{1st})
Puls number
D1
0mV
TP1
TP2
~ half inactivation voltage
8S
Vh=-120mV
-120mV
20ms
D2
Inhibition (%)
Conc [mg/ml]
IC50
1.632
D3
Pre-
0.123mg/ml ethanol (v/v, 70%) extract of G. uralensis
0.37mg/ml ethanol (v/v, 70%) extract of G. uralensis
1.11mg/ml ethanol (v/v, 70%) extract of G. uralensis
3.33mg/ml ethanol (v/v, 70%) extract of G. uralensis
10mg/ml ethanol (v/v, 70%) extract of G. uralensis
1nA
5ms
D4
Inhibition (%)
Conc [mg/ml]
IC50
4.557
D5
Pre-
0.123mg/ml ethanol (v/v, 70%) extract of G. uralensis
0.37mg/ml ethanol (v/v, 70%) extract of G. uralensis
1.11mg/ml ethanol (v/v, 70%) extract of G. uralensis
3.33mg/ml ethanol (v/v, 70%) extract of G. uralensis
10mg/ml ethanol (v/v, 70%) extract of G. uralensis
1nA
5ms

Liquid chromatographic analysis was performed on an Agilent UPLC-DAD system (1290 Infinity II, Agilent Technologies, USA), which was equipped with an Agilent DAD detector (G7117A, Agilent Technologies, USA), an Agilent 1290 auto-sampler (G7167B, Agilent Technologies, USA), an Agilent 1290 infinity column heater (G7166B, Agilent Technologies, USA) and a Thermo-C18 (1.5 mm × 210 mm, 2.6 μm) column (Thermo Fisher Scientific, USA).

2.5. Species identification

The species identification was performed using a gene sequencer based on Appendix IIA of Pharmacopoeia of the People's Republic of China. All the sequences obtained in the research were determined using the DNA barcode identification system (http://www.tcmbarcode.cn) of Chinese herbal medicine by using the BLAST (Basic Local Alignment Search Tool) method.

2.6. Electrophysiology

2.6.1. Sample preparation

Medicinal materials were immersed in ethanol (w/v, 1:7) at concentrations of 30%, 50%, 70% and 90% (v/v) and boiled twice for 60 min at each time. Thereafter, the solutions were filtered with a screen mesh of 75 μm aperture and concentrated to 0.5 g/ml liquid extraction (calculated with medicinal herbs). Finally, they were converted to freeze-dried powder by freeze-drying.

For electrophysiology studies, each freeze-dried powder was dissolved in DMSO to make 4 mg/ml and 8 mg/ml stock solutions.

2.6.2. Electrophysiological recordings

The electrophysiological recordings were obtained under visual control of a microscope. The amplifier EPC10 was used for recording the electrophysiological signal. Offset potentials were nulled directly before formation of a seal. No leak subtraction was performed. Fast capacitance (in pF) compensation was performed after a high seal was achieved. Cell capacitance (in pF) compensation was performed from whole-cell capacitance compensation after the whole cell mode was achieved. All experiments were performed at room temperature.

To measure the Nav1.4 channels, the membrane potential was held at −90 mV, and then depolarized to −10 mV for 50 ms to activate Nav1.4 currents. An interpulse interval of 10 s allows recovery from inactivation. The depolarized plus was confirmed by IV test.

Cells were incubated with the test article for 5 min, or until the current reached a steady-state level. Two concentrations of the test article were tested. The test and control solutions flowed into a recording chamber mounted on the stage of an inverted microscope via a gravity-fed solution delivery system.

The data which were stored and analyzed with Patch master and Igor Pro were represented by $\overline{X} \pm S$ and analyzed by paired T test. $P < 0.05$ indicates a significant difference. Sodium currents from activation were converted to sodium conductance [$G = I/(V-Vrev)$] and plotted as a function of test potential using the Boltzmann equation [$G/Gmax = 1/(1 + \exp((Vh-V)/K)$] to give values for Vh (potential causing half-maximal activation) and K (slope factor). Similarly, currents from steady-state inactivation were also plotted as a function of prepulse potential and fitted with the Boltzmann equation [$I/Imax = 1/(1 + \exp((V-Vh)/K)$] to give values for Vh (potential causing half-maximal activation) and K (slope factor). Currents from steady-state recovery process curves were plotted as a function of prepulse potential and fitted with the Boltzmann equation [$I = A_1\exp(-t/\tau)+A_0$] to give values for τ (recovery time).

2.7. UPLC-DAD determination

2.7.1. Sample preparation

For UPLC analysis, the solution was dissolved in methanol (v/v, 1:1), with sufficient mixing. Before injection, it was centrifuged at 12,000 rpm for 5 min at 4 °C and filtered through a 0.22 μm filter.

2.7.2. Separation conditions

The binary gradient elution system consisted of solvent A (0.1% formic acid water) and solvent B (acetonitrile). Optimum separation was achieved by using the gradient program described as follows: 0~5 min, 5%–10%(B); 5–10 min, 10%–15%(B); 10–18 min, 15%–20%(B); 18–25 min, 20%–25%(B); 25–35 min, 25%–40%(B); 35–36 min, 40%–95%(B); 36–46 min, 95%(B). The column temperature was maintained at 30 °C. The autosampler was conditioned at 25 °C and the injection volume was 3 μl. The flow rate was 0.4 ml/min. The raw data was detected by a UPLC-DAD (Agilent1290 Infinity II, USA), and the wavelengths was 230 nm for glycyrrhizic acid, 270 nm for liquiritin, and 360 nm for isoliquiritigenin and echinatin.

2.7.3. Preparation of standard solutions

The appropriate amounts of liquiritin, echinatin, isoliquiritigenin and glycyrrhizic acid were separately weighed and dissolved together in methanol to achieve a standard working solution of four different concentrations; the concentrations of the four standard substances were 66 μg/ml, 68 μg/ml, 76 μg/ml and 88 μg/ml. The calibration curves were constructed by analyzing the mixed solution, and the series of working solutions were within the ranges of 1.32–18.48 μg/ml for liquiritin, 1.36–19.04 μg/ml for echinatin, 1.52–21.28 μg/ml for isoliquiritigenin and 1.76–24.64 μg/ml for glycyrrhizinc acid. All solutions were prepared in dark brown calibrated flasks and stored at 4 °C.

2.7.4. Method validation

The UPLC method was validated in terms of linearity, precision, stability, repeatability and recovery. The validation was performed based on the relative peak areas (RPAs). Linear regression analysis was employed to construct calibration curves. The data was expressed as mean ± standard deviation, and the relative standard deviation (RSD) was used to evaluate precision, stability, repeatability and recovery.

3. Results

3.1. DNA barcoding

After sequencing, the splicing sequence was compared with the database and standard reference sequence of *G. uralensis*. Also, the biological origin of the sample was further confirmed.

Fig. 2. Effect of the ethanol extract of *G. uralensis* on I_{Nav}1.4 and kinetics. *A)* The voltage dependent effect of *G. uralensis* on I_{Nav}1.4 density. *B1)* Effect of 3 mg/ml ethanol extract of *G. uralensis* at 70% (v/v) on steady-state activation kinetics of I_{Nav}1.4. Data obtained from I-U relationship. *B2)* Effect of 3 mg/ml ethanol extract of *G. uralensis* at 70% (v/v) on steady-state inactivation kinetics of I_{Nav}1.4. The steady-state inactivation curves of I_{Nav}1.4 were obtained by means of a double-pulse protocol; a 1 s conditioning prepulse depolarized to various potentials (from −90 mV to 0 mV, holding potential at −80 mV) was followed by a 200 ms test pulse to 0 mV. B3) Effect of 3 mg/ml ethanol extract of *G. uralensis* at 70% (v/v) on the recovery curve of I_{Nav}1.4 from steady-state inactivation. Using a standard two-pulse protocol, a 200 ms prepulse to 0 mV from holding potential of −40 mV was followed by various recovery durations and then by a test pulse to 0 mV for 200 ms. *C1, C2 and C3)* The use-dependent inhibition protocol: the membrane potential was held at −90 mV, then depolarized to −10 mV and maintained for 50 ms, recorded at frequencies 1 Hz, 3 Hz and 10 Hz. *D1, D2, D3, D4 and D5)* The concentration dependent protocol.

(1) ITS2 test sequence of *G. uralensis*: CAGACCGTTGCCCGATGC-CAATTGCCTCGCG ATAGGTACTTTGGTTGTGCAGGGTGAATG TTGGCTTCCCGTGAGCATTGCGGCCTCACGGTTGGCTCAAAA CTGAGTCCATGGTAGGGTTTGGCATGATCGATGGTGGTTGAGT-GACGCTCGAGACCAATCATGTGTGACTCCACTGAGTTTGGGCT CTGTAACCAATAGGCGTCTTTGAACGCTCGTGATG。

(2) PsbA-trnH test sequence of *G. uralensis:* CCATCTA-TAAATGGATAATATTTTGGTTT TAAAGAAGGATACGAGGTTTTG AAAGTAAAGGAGTAATATCAACATTGTTGATATTACTCCCTT CTTGACTTTTACTTTTCTTAGTAGTCTATATATGTATATATATACA TACATATTGTAATACATATGACTTCACAATGTAAAATCAGAAA AAAAGAAATGTTTTCTTATTTTTTCTGATTTTCTCGTATTTTA GAAGACGCGTAAGAACTTAAAAGAGAAGAAAATAAGTG ATAATGAAAAAGTCTAAATGGAAAGTTAGATAATTTATACAT

3.2. Effect of ethanol (30%, 50%, 70% and 90%, v/v) extract of G. uralensis on Nav1.4

In this study, whole-cell patch clamp technique was performed to investigate the effect of ethanol (30%, 50%, 70% and 90%, v/v) extract of *G. uralensis* on the $I_{Nav}1.4$. The peak current decreased significantly after treatment with 4 mg/ml and 8 mg/ml ethanol extracts of *G. uralensis* at 30% (v/v) compared with the control ($p < 0.05$, $n = 3$); the $I_{Nav}1.4$ decreased from −289.32 ± 10.21 pA/pF to −66.74 ± 5.65 pA/pF and −1.50 ± 0.65 pA/pF respectively, and the inhibitory effect on $I_{Nav}1.4$ were 77.00 ± 0.03% and 99.00 ± 0.01% respectively. The inhibition rate of the 8 mg/ml group was significantly higher than that of the 4 mg/ml group ($p < 0.05$, $n = 3$) (Fig. 1A1). This inhibitory effect of ethanol extract of *G. uralensis* at 30% (v/v) on the $I_{Nav}1.4$ appeared within 6 min after the start of perfusion of the bath solution containing ethanol extract of *G. uralensis* at 30% (v/v) (Fig. 1A2).

The peak current decreased significantly after treatment with 4 mg/ml and 8 mg/ml ethanol extracts of *G. uralensis* at 50% (v/v) compared with the control ($p < 0.05$, $n = 3$); the $I_{Nav}1.4$ decreased from −241.08 ± 12.33 pA/pF to −170.53 ± 11.28 pA/pF and −7.44 ± 0.98 pA/pF respectively, and the inhibitory effects on $I_{Nav}1.4$ were 34.75 ± 0.09% and 97.10 ± 0.02% respectively. The inhibition rate of the 8 mg/ml group was significantly higher than that of the 4 mg/ml group ($p < 0.05$, $n = 3$) (Fig. 1B1). This inhibitory effect of ethanol extract of *G. uralensis* at 50% (v/v) on the $I_{Nav}1.4$ appeared within 3 min after the start of perfusion of the bath solution containing ethanol extract of *G. uralensis* at 50% (v/v) (Fig. 1B2).

The peak current decreased significantly after the treatment with 4 mg/ml and 8 mg/ml ethanol extracts of *G. uralensis* at 70% (v/v) compared with the control ($p < 0.05$, $n = 3$); the $I_{Nav}1.4$ decreased from −85.22 ± 9.23 pA/pF to 0.46 ± 0.08 pA/pF and 0.75 ± 0.09 pA/pF respectively, and the inhibitory effects on $I_{Nav}1.4$ were 100.00 ± 0.01% and 100.00 ± 0.01%, respectively. There was no significant difference in the inhibition rate between the 8 mg/ml and the 4 mg/ml groups ($p > 0.05$, $n = 3$) (Fig. 1C1). This inhibitory effect of ethanol (v/v, 70%) extract of *G. uralensis* at 70% (v/v) on the $I_{Nav}1.4$ appeared within 2.5 min after starting perfusion of the bath solution containing ethanol extract of *G. uralensis* at 70% (v/v) (Fig. 1C2).

The peak current decreased after treatment with 4 mg/ml and 8 mg/ml ethanol extracts of *G. uralensis* at 90% (v/v) from −133.71 ± 4.73 pA/pF to −130.46 ± 9.38 pA/pF and −112.11 ± 5.79 pA/Pf respectively. There was no significant difference between the two groups ($p > 0.05$, $n = 3$) (Fig. 1D1, D2). The inhibitory effects on $I_{Nav}1.4$ were 2.00 ± 0.01% and 17.00 ± 0.04% respectively.

After washing out *G. uralensis*, the inhibitory effect of *G. uralensis* on $I_{Nav}1.4$ was abolished quickly (Fig. 1A2, B2 and C2). The inhibitory effect of *G. uralensis* on $I_{Nav}1.4$ is shown in Fig. 1E.

3.3. Activation and inactivation kinetics, recovery curve, frequency and concentration dependent inhibition effect of ethanol extract of G. uralensis at 70% (v/v) on Nav1.4

Fig. 3A demonstrates the effect of 3 mg/mL ethanol extract of *G. uralensis* at 70% (v/v) on current voltage relationship of $I_{Nav}1.4$. The result shows that 3 mg/ml ethanol extract of *G. uralensis* at 30% (v/v) significantly inhibited the $I_{Nav}1.4$ peak current. It decreased the $I_{Nav}1.4$ by more than 40% compared with the control (Fig. 1E) after which the inhibition persisted with further depolarization potentials. However, the *G. uralensis* did not affect the activation property and reversal potential of $I_{Nav}1.4$ (Fig. 2A).

The study showed that treatment with 3 mg/ml ethanol extract of *G. uralensis* at 70% (v/v) did not affect the Nav1.4 activation curve. The V_h values (in mV) were −25.1 ± 1.2 mV for pre-treatment and −25.2 ± 1.1 mV for post-treatment, ($P > 0.05$), and the K values were 9.5 ± 1.1 mV for pre-treatment and 9.2 ± 1.6 mV for post-treatment, ($P > 0.05$) (Fig. 2B1). It did not change the V_h values (in mV) and the K values.

Treatment with 3 mg/mL ethanol extract of *G. uralensis at* 70% (v/v) has the following effects: the Nav1.4 inactivation curve shifted to the hyperpolarization side and the voltage of half-maximal inactivation shifted to the hyperpolarization side by 16.5 mV; compared with the control (Fig. 2 B2). The data showed that 3 mg/mL ethanol extract of *G. uralensis* at 70% (v/v) can significantly affect the Nav1.4 inactivation curve, which changed the V_h values (in mV) from −51.3 ± 1.2 mV to −68.7 ± 1.3 mV ($P < 0.05$) and the K values from 7.6 ± 1.1 mV to 4.5 ± 1.6 mV ($P < 0.05$).

Meanwhile, 3 mg/mL ethanol extract of *G. uralensis* at 70% (v/v) can significantly affect the Nav1.4 recovery curve from steady-state inactivation and increased the recovery time from 15.3 ± 2.3 ms for pre-treatment to 26.5 ± 5.3 ms for post-treatment ($P < 0.05$) (Fig. 2 B3).

The use-dependent inhibition of 3 mg/mL ethanol extract of *G. uralensis* at 70% (v/v) was studied under the following protocol: the membrane potential was held at −90 mV, then depolarized to −10 mV and maintained for 50 ms. The use-dependent inhibition was recorded at frequencies 1 Hz, 3 Hz and 10 Hz. 3 mg/ml ethanol extract of *G. uralensis* at 70% (v/v) showed a weak use-dependent inhibitory effect ($P > 0.05$) (Fig. 2 C1, C2 and C3). Therefore, the concentration of 3 mg/ml did not show a frequency dependent inhibitory effect of the ethanol extract of *G. uralensis* at 70% (v/v).

The concentration dependence of ethanol extract of *G. uralensis* at 70% (v/v) on Nav1.4 current was measured under a two-pulse protocol. From a holding potential of −120 mV, the first depolarizing test pulse was followed by a hyperpolarizing conditioning of inter pulse to half inactivation voltage (8 s interval), followed by 20 ms of recovery period at −120mv, and then a second depolarizing test pulse to 0 mV for 20 ms. The inhibition of Nav1.4 current at the resting state (TP1) and half inactivating state (TP2) were calculated (Fig. 2 D1). The IC50 of ethanol extract of *G. uralensis* at 70% (v/v) was 4.56 mg/ml at the resting state (Fig. 3 D2, D3) and 1.63 mg/ml at the half inactivating state (Fig. 2 D4, D5).

3.4. Effect of eleven compounds of G. uralensis on Nav1.4

This study showed the inhibitory effects of eleven compounds of *G. uralensis* on the $I_{Nav}1.4$ at a concentration of 10 μmol/l. Treatment with isoliquiritigenin, echinatin, liquiritin, glycyrrhizic acid, liquiritigenin, formononetin, neoisoliquiritin and glycyrrhetinic acid had inhibitory effects on $I_{Nav}1.4$ and decreased the $I_{Nav}1.4$ by 39.98 ± 4.55%, 33.20 ± 1.61%, 22.62 ± 0.30%, 20.54 ± 4.82%, 19.89 ± 3.15%, 18.63 ± 0.53%, 15.02 ± 3.24% and 14.90 ± 1.98%

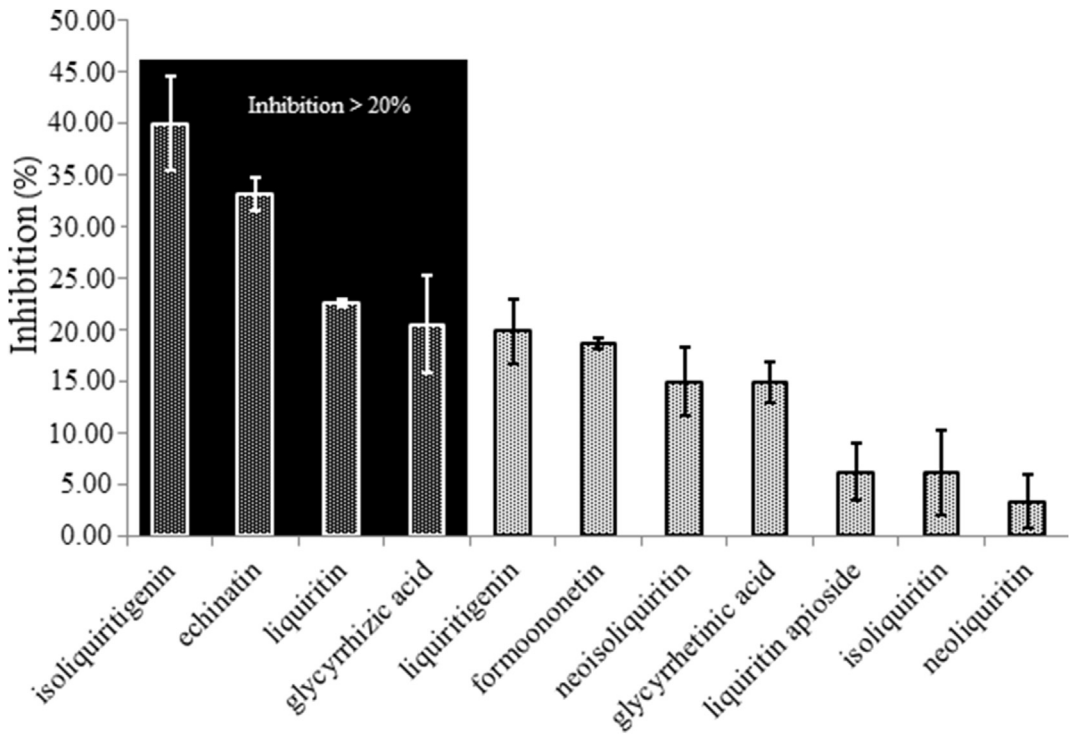

Fig. 3. Inhibition of the eleven compounds on $I_{Nav}1.4$.

respectively. In contrast, liquiritin apioside, isoliquiritin and neoliquiritin had almost no effect on $I_{Nav}1.4$ (Table 1) (Fig. 3).

3.5. Contents of isoliquiritigenin, echinatin, liquiritin and glycyrrhizic acid in ethanol extract of G. uralensis

3.5.1. Calibration curves

Linearity was evaluated by analyzing six injection quantities of standard solutions, and the calibration curves were constructed by plotting the peak areas and the injection quantity of 5 μl of each compound with six different concentrations. Linear regression equation for liquiritin, echiantin, isoliquiritigenin and glycyrrhizic acid are y = 3,697,762.509x+2.241, y = 4768324.747x+ 5.726, y = 8823821.909x+5.948, y = 1112094.785x-1.900. Correlation coefficients are 1.000, 0.998, 1.000 and 1.000. Linear range are 1.32–18.48 μg/ml, 1.36–19.04 μg/ml, 1.52–21.28 μg/ml, 1.76–24.64 μg/ml.

Table 1
Effect of the eleven compounds of *G. uralensis* on peak current of Nav1.4

Compounds	Pre- treatment (pA)	Post- treatment (pA)	Inhibition (%)
isoliquiritigenin	−5187.75 ± 439.04	−3128.05 ± 597.43*	39.98 ± 4.55
echinatin	−1206.61 ± 865.77	−796.18 ± 550.87*	33.20 ± 1.61
liquiritin	−1427.88 ± 1182.59	−1107.36 ± 921.14*	22.62 ± 0.30
glycyrrhizic acid	−3748.10 ± 2095.58	−3049.85 ± 1920.86*	20.54 ± 4.82
liquiritigenin	−631.98 ± 68.92	−507.81 ± 83.40*	19.89 ± 3.15
formononetin	−1334.00 ± 721.54	−1088.15 ± 597.15*	18.63 ± 0.53
neoisoliquiritin	−2231.96 ± 1874.31	−1939.55 ± 1694.87*	15.02 ± 3.24
glycyrrhetinic acid	−4123.25 ± 987.90	−3495.05 ± 725.14*	14.90 ± 1.98
liquiritin apioside	−1497.16 ± 789.76	−1387.76 ± 681.00	6.26 ± 2.80
isoliquiritin	−2946.90 ± 853.05	−2741.00 ± 627.06	6.13 ± 4.17
neoliquiritin	−1817.06 ± 1413.85	−1728.81 ± 1298.52	3.42 ± 2.60

*$p < 0.05$, n = 3.

3.5.2. Precision, stability, repeatability and recovery

Precision was tested by six replicate determinations of the standard working solution. Stability was evaluated by analyzing the solutions stored at room temperature (about 25 °C) at different time points (0, 4, 8, 12 and 24 h after preparation). The solutions used in the stability test included mixed solutions of reference standard and *G. uralensis* sample solutions. Six replicates were performed for the test. The obtained data confirmed that the four compounds were stable within 24 h at 25 °C and their RSD values were between 0.79% and 1.03%. Repeatability was examined by six replications of a sample. In the recovery test, samples were prepared at three concentration levels in triplicate by spiking known quantities of each of the four standards into the *G. uralensis* sample, after which extraction and analysis were done according to the described procedures. The validation data are shown in Table 2.

3.5.3. Content

The UPLC-DAD data demonstrated that liquiritin, echiantin, isoliquiritigenin and glycyrrhizic acid are present in the ethanol extract of *G. uralensis* (Figs. 4 and 5). The contents of the four marker compounds in the ethanol extract of *G. uralensis* at 70% (v/v) are shown in Table 3.

Table 2
Precision, repeatability, stability and recovery of the four standard substances.

Standard Substance	Precision RSD (%) (n = 6)	Repeatability RSD (%) (n = 6)	Stability RSD (%) (n = 6)	Recoveries[a] (%) RSD (%) (n = 9)
liquiritin	1.58%	1.02%	0.79%	98.56% 1.48%
echinatin	1.46%	0.97%	1.03%	98.89% 2.11%
isoliquiritigenin	1.49%	1.01%	1.01%	99.49% 1.63%
glycyrrhizic acid	1.22%	0.95%	0.88%	99.63% 2.01%

[a] Recovery (%) = 100*(amount found-original amount)/amount spiked.

4. Discussion

In this study, we investigated the inhibitory effect of the ethanol extract of *G. uralensis* on $I_{Nav}1.4$. The results showed that 4 mg/ml and 8 mg/ml ethanol extracts of *G. uralensis* at 30% and 70% (v/v) had a stronger inhibitory effect on $I_{Nav}1.4$, with inhibitory rates of 77.29%–100%. Further, 8 mg/ml ethanol extract of *G. uralensis* at 50% (v/v) had a stronger inhibitory effect on $I_{Nav}1.4$, with inhibitory rate of 95%. However, the inhibitory rate decreased to 31.98% at the concentration of 4 mg/ml. Treatment with 4 mg/ml and 8 mg/ml ethanol extracts of *G. uralensis* at 90% (v/v) showed a lower inhibitory effect on $I_{Nav}1.4$, which decreased to 2.2% and 16.63% respectively.

In order to further investigate its blocking effect on $I_{Nav}1.4$ and the channel dynamics, 3 mg/ml ethanol extract of *G. uralensis* at 70% (v/v) was also studied. Based on the results, we found that it did not alter the shape of the *I-U* curve or the reversal potential. Also, it did not affect the Nav1.4 activation curve. So, the ethanol extract of *G. uralensis* at 70% (v/v) does not have a significant inhibitory effect on the activation state of Nav1.4. However, it can significantly affect the Nav1.4 inactivation and recovery curves; it can shift the inactivation curve to the hyperpolarization side and obviously increase the recovery time of Nav1.4 from the inactivation state. We can draw a conclusion from the results above that ethanol extract of *G. uralensis* at 70% (v/v) can alter the inactivation characteristics of Nav1.4 and increase the recovery time of Nav1.4 from the inactivating state to the resting state.

In this study, eleven chemical compounds of ethanol extract of *G. uralensis* were selected in order to clarify their different degrees of inhibition with respect to $I_{Nav}1.4$. They include isoliquiritigenin, echinatin, liquiritin, glycyrrhizic acid, liquiritigenin, formononetin, neoisoliquiritin, glycyrrhetinic acid, liquiritin apioside, isoliquiritin and neoliquiritin. The results showed that treatments with 10 μmol/l isoliquiritigenin, echinatin, liquiritin and glycyrrhizic acid decreased the $I_{Nav}1.4$ by more than 20% compared with the control; the values were 39.98 ± 4.55%, 33.20 ± 1.61%,

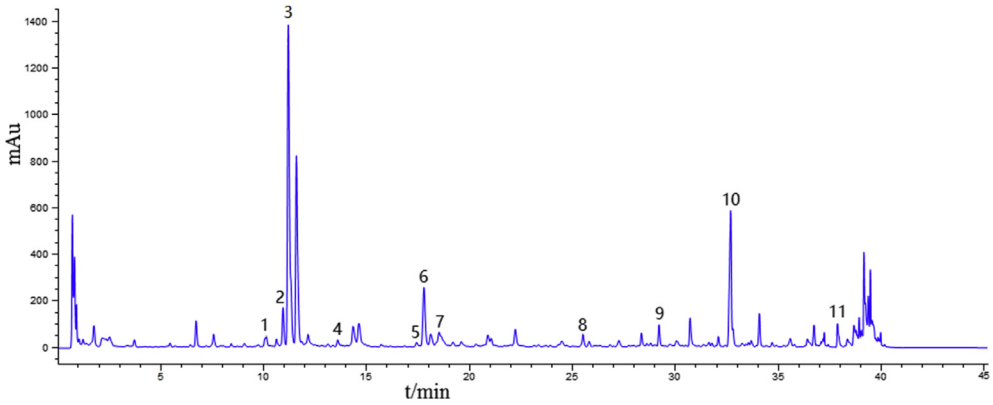

Fig. 4. UPLC-DAD chromatogram of the ethanol extract of *G. uralensis* at 50% (v/v) at a wavelength of 270 nm. The vertical axis represents response value (mAu) and the horizontal axis represents retention time (min). 1. formononetin, 2. liquiritin apioside, 3. liquiritin, 4. neoliquiritin, 5. neoisoliquiritin, 6. isoliquiritin, 7. liquiritigenin, 8. echinatin, 9. isoliquiritigenin, 10. glycyrrhizic acid, 11. glycyrrhetinic acid.

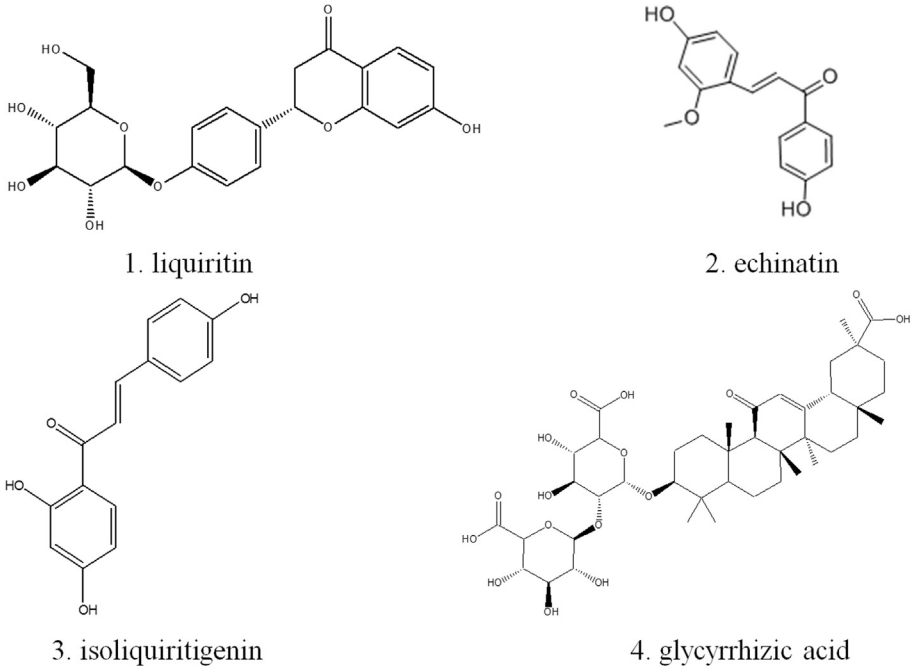

Fig. 5. Chemical structures of the four marker substances of *G. uralensis*.

Table 3
The contents of the four compounds in the ethanol extract of *G. uralensis*.

Groups	Concentration mg/ml	Liquiritin μg/ml	Echinatin μg/ml	Isoliquiritigenin μg/ml	Glycyrrhizic acid μg/ml
ethanol (v/v, 30%) extract of *G. uralensis*	4	10.67	0.08	0.13	24.58
	8	21.34	0.16	0.26	49.15
ethanol (v/v, 50%) extract of *G. uralensis*	4	10.70	0.09	0.13	21.00
	8	21.41	0.18	0.26	41.99
ethanol (v/v, 70%) extract of *G. uralensis*	4	10.83	0.09	0.15	22.67
	8	21.67	0.19	0.29	45.34
ethanol (v/v, 90%) extract of *G. uralensis*	4	7.42	0.05	0.09	4.40
	8	14.84	0.11	0.17	8.80

22.62 ± 0.30% and 20.54 ± 4.82% respectively. The other seven compounds showed a lower inhibitory rate. Therefore, isoliquiritigenin, echinatin, liquiritin and glycyrrhizic acid were selected as the marker substances in inhibiting $I_{Nav}1.4$. Based on the research results mentioned above, further investigation was carried out for quantitative analysis of the four components of 4 mg/ml and 8 mg/ml ethanol (v/v, 30%, 50%, 70%, 90%) extract of *G. uralensis*. The result of the investigation showed that glycyrrhizic acid reached the maximum concentration of 49.15 μg/ml, while echinatin had the lowest concentration, with a maximum value of 0.08 μg/ml only. There was no obvious correlation between the concentration of the marker substances of the ethanol extracts of *G. uralensis* and the inhibitory rate on $I_{Nav}1.4$. A traditional Chinese medicine theory holds that there is a synergistic effect between the compounds of this Chinese medicine, which leads to a therapeutic effect.[14–16] The four compounds may have synergistic effects and eventually play a role in the inhibition of Nav1.4 VGSCs currents, or there may be many other compounds besides these eleven chemical compounds that have been studied previously, one or more of them may have an inhibition effect on $I_{Nav}1.4$ and work in coordination with each other to play a therapeutic role. Therefore, it is difficult to determine which compound is most responsible for the inhibitory effect of ethanol extract of *G. uralensis* on Nav1.4 VGSCs currents in this experimental condition. Even so, we can still conclude that isoliquiritigenin, echinatin, liquiritin and glycyrrhizic acid play a key role in the inhibition of Nav1.4 VGSCs currents. Further research is in progress to provide scientific explanation of such phenomenon.

In summary, $I_{Nav}1.4$ was blocked by ethanol extract of *G. uralensis* treatment in a dose-dependent manner. Moreover, the inactivation curve shifted to the hyperpolarization side. Further studies are needed to resolve the electrophysiological mechanisms of the inhibitory effect of ethanol extract of *G. uralensis* on Nav1.4 VGSCs. In addition, eight other *a*-subunits (Nav1.1~1.3, 1.5–1.9) and 4 different β-subunits (β1~β4) should be investigated. Meanwhile, the inhibitory effects of *Glycyrrhiza inflata* and *Glycyrrhiza glabra* on $I_{Nav}1.4$ should also be investigated to analyze the correlation between the three different species of licorice. This will enhance the scientific elucidation of the significance of different sources of licorice in the treatment of diseases.

Conflict of interests

The authors declare no conflict of interests.

Acknowledgments

The authors acknowledge financial supports from “the Fundamental Research Funds for the Central public welfare research institutes” (NO: ZXKT15037) and “Study on the development of classical prescriptions of peony and liquorice decoction” (NO: H2016072-03). Thanks are due to Dr. Li and Dr. Zhang (ICE Bioscience Inc.) for assistance with the experiments.

Appendix A. Supplementary data

Supplementary data related to this article can be found at https://doi.org/10.1016/j.jphs.2017.11.008.

References

1. Nakatani Y, Masuko H, Amano T. The effect of lamotrigine on Nav1.4 voltage-gated sodium channels. *Jpn J Pharmacol*. 2013;123(2):203–206.
2. Goral RO, Leipold E, Nematian-Ardestani E, et al. Heterologous expression of Na V 1.9 chimeras in various cell systems. *Pflugers Arch Eur J Physiol*. 2015;467(12):2423–2435.
3. Ekberg J, Adams DJ. Neuronal voltage-gated sodium channel subtypes: key roles in inflammatory and neuropathic pain. *Int J Biochem Cell Biol*. 2006;38:2005–2010.
4. Torbergsen T, Jurkat-Rott K, Stalberg EV, et al. Painful cramps and giant myotonic discharges in a family with the Nav1.4-G1306A mutation. *Muscle Nerve*. 2015;52(4):680–683.
5. Karnebeek CDV, Ye XC, Abdelsayed M, et al. MG-115 Compd heterozygous SCN4A Mutat underlies severe Congenit Hypot biophysical Alter encoded voltage-gated Nav1.4 sodium channel 2015;52(Suppl 1):A3.2–A4.
6. Ammar T, Renaud JM. Diaphragm of hyperkalemic periodic paralysis mouse has No contractility abnormality compared to the robust abnormalities in EDL and soleus. *Faseb J*. April 2015;29(Suppl 1).
7. Tiryakioglu O, Erkoc K, Tunerir B, et al. The effect of Iloprost and N-Acetylcysteine on skeletal muscle Injury in an acute aortic Ischemia-reperfusion model: an experimental study. *Biomed Res Int*. 2015;2015:453748.
8. Goeckmann V, Rothammer S, Medugorac I. Bovine spastic paresis: a review of the genetic background and perspectives for the future. *Vet J*. 2016;216:64–71.
9. Zhang B, Li M, Wang L, et al. The association between the polymorphisms in a sodium channel gene SCN7A and essential hypertension: a case-control study in the Northern han Chinese. *Ann Hum Genet*. 2015;79(1):28–36.
10. Zhang Y, Zun-Ji KE, Yang J, et al. The outline on the study of the mechanism of peony and licorice decoction and its active components to protect brain. *Prog Mod Biomed*. 2014;14(34):6773–6777.
11. Zhu G, Zhang G, Wang M, et al. Simultaneous determination of nine active compounds of the traditional Chinese medicinal prescription shaoyao-gancao-tang and analysis of the relationship between therapeutical effect and compatibility of medicines. *Evi Base Compl Alternative Med eCAM*. 2014;2014:521038.
12. Dan H, Le XU, Junkui LI, et al. Effect of peony and Licorice Decoction on New Zealand rabbits with Desmodium excised ureteral smooth muscle tension. *Clin J Tradit Chin Med*. 2015;(2):238–241.
13. Jhang JF, Kuo HC. Novel treatment of chronic bladder pain syndrome and other pelvic pain disorders by Onabotulinumtoxin A injection. *Toxins*. 2015;7(6):2232–2250.
14. Liu Y, Kong JM, Chia LS, et al. Synergistic effect of traditional Chinese medicine. *Asian J Chem*. 2007;19(2):867–882.
15. Guo MH, Hai-Tao LI, Zhu H, et al. The research progress on the synergistic effect of traditional Chinese medicine monomer and antifungal drug. *J Pract Dermatol*. 2016;9(5):326–328.
16. Zhang A, Hui S, Ye Y, et al. An in vivo analysis of the therapeutic and synergistic properties of Chinese medicinal formula Yin-Chen-Hao-Tang based on its active constituents. *Fitoterapia*. 2011;82(8):1160–1168.

Journal of Pharmacological Sciences 136 (2018) 66–72

Contents lists available at ScienceDirect

Journal of Pharmacological Sciences

journal homepage: www.elsevier.com/locate/jphs

Full paper

Dracorhodin perchlorate regulates fibroblast proliferation to promote rat's wound healing

Xiaowen Jiang [a, 1], Lin Liu [a, 1], Lu Qiao [a], Binqing Zhang [a], Xuewei Wang [a], Yuwen Han [a], Wenhui Yu [a, b, *]

[a] College of Veterinary Medicine, Northeast Agricultural University, Harbin, 150030, PR China
[b] Key Laboratory of the Provincial Education Department of Heilongjiang for Common Animal Disease Prevention and Treatment, PR China

ARTICLE INFO

Article history:
Received 13 June 2017
Received in revised form
30 November 2017
Accepted 5 December 2017
Available online 7 February 2018

Keywords:
Dracorhodin perchlorate
Fibroblasts
ERK
Rat model
Wound healing

ABSTRACT

In recent years, plant-derived extracts are increasing interest from researchers worldwide due to good efficacy and lower side effects. Among the different plant extracts, Dracorhodin perchlorate (DP) is originated from *Dragon's blood* which has long been used as a natural medicine with various pharmacological activities. In the present study, we have explored the potential regulation of DP on fibroblast proliferation which promotes wound healing both *in vitro* and *in vivo*. DP at treatment of 12–24 h significantly induced fibroblast proliferation which is associated with increasing level of phosphorylated-extracellular signal-regulated kinase (ERK). Moreover, if ERK is halted with siRNA, DP cannot induce fibroblast proliferation. *In vivo*, DP ointment treatment at low- (2.5 μg/mL), medium- (5 μg/mL) and high- (10 μg/mL) doses, rat wounds healed more rapidly compared with the control group. After DP treatment for 7 days, Serpin family H member 1 (SERPINH1) staining confirmed enhanced fibroblast proliferation in the wound tissue. Finally, phosphorylated-ERK in the wound tissue remarkably increased with DP ointment treatment. Therefore, DP may be developed into a potential lead compounds for the treatment of wounds in clinical trials in the near future.

© 2018 The Authors. Production and hosting by Elsevier B.V. on behalf of Japanese Pharmacological Society. This is an open access article under the CC BY-NC-ND license (http://creativecommons.org/licenses/by-nc-nd/4.0/).

1. Introduction

With the rapid development of medical field research, more and more natural plants are used to study in treating clinical ailments. The most well-known of them is artemisinin, extracted from the stem of Artemisia annua, which has saved millions of malaria patients' lives.[1] In addition, ginseng extracts are widely used for various treatment of ailments including cancer.[2] Berberine can inhibit bacterial growth.[3] Morphine has analgesic effects.[4] *Dragon's blood* is a resin obtained from the fruit of a number of palmae plants predominantly distributed throughout Asia and Indonesia.[5] *Dragon's blood* is regarded as a natural medicine for improving blood circulation and reducing pain.[6] Research also showed that *Dragon's blood* possessed several pharmacological effects, including immunoregulatory,[7] anti-inflammation,[8] antidiarrheic,[9] antibacterial,[10] antiviral,[11] antioxidant,[12] and anticancer,[13] and so on. Interestingly, *Dragon's blood* can stimulate epithelial regeneration and wound healing by promoting fibroblasts proliferation and collagen synthesis.[14] *Dragon's blood* extracts comprise of many active compounds, mainly flavonoids and terpene resin acid. As the extract of the *Dragon's Blood*, *Dracorhodin* always exists in the form of a particular salt, which is called Dracorhodin perchlorate (DP). Recent research has demonstrated that DP promotes vascular endothelial cell proliferation and angiogenesis.[15] However, research on whether DP promote wound healing has not been reported. The purpose of this study was to determine the effects of DP on wound healing using both *in vitro* and *in vivo* models.

Skin damage initiates a series of biological reactions to achieve self-healing, including hemostasis, granulation tissue regeneration, and tissue reconstruction.[16] Various kinds of cells including fibroblasts, endothelial cells, keratinocytes, macrophages and platelets play key roles together in wound healing process. This process involves cell proliferation and migration, collagen production, and vascular formation. Fibroblasts are the most vital cells for

* Corresponding author. College of Veterinary Medicine, Northeast Agricultural University, Harbin, 150030, PR China.
E-mail address: yuwenhui@neau.edu.cn (W. Yu).
Peer review under responsibility of Japanese Pharmacological Society.
[1] These authors contributed equally to this work and should be considered co-first authors.

https://doi.org/10.1016/j.jphs.2017.12.003
1347-8613/© 2018 The Authors. Production and hosting by Elsevier B.V. on behalf of Japanese Pharmacological Society. This is an open access article under the CC BY-NC-ND license (http://creativecommons.org/licenses/by-nc-nd/4.0/).

extracellular matrix production and remodeling, which are beneficial for forming wound granulation tissues in wound healing.[17,18] At the same time, wound healing process is regulated by a large number of cytokines and growth factors, which are important regulators to elicit the cell growth, proliferation, migration, differentiation and adhesion, ECM deposition and proteinase activation. Moreover, significant study has demonstrated that cell proliferation is mediated by ERK signaling pathway in the process of wound healing.[19,20] We thus hypothesized that DP may activate cellular functions through ERK pathways, and the activation of ERK signaling pathway may alleviate the proliferation and migration of fibroblasts.

SERPINH1 (serpin peptidase inhibitor, clade H, member 1, also known as HSP47), a 47-kDa heat-shock protein, is a collagen-specific molecular chaperone localized in the endoplasmic reticulum research showed that SERPINH1-positive cells were regarded as fibroblasts in skin specimens.[21] Therefore, we selected the SERPINH1 antibody as a marker of fibroblast in skin tissues samples. This study aimed to identify the mechanisms whether DP induces proliferation and migration of fibroblasts during wound healing. Our results demonstrated that DP may be considered as potential treatments for wound healing and provided a basis for further clinical experiments.

2. Materials and methods

2.1. Cell viability and cell proliferation assays

DP was purchased from Shanghai yuanye Bio-Technology Co., Ltd (R20J6F1, Shanghai, China). NIH/3T3 fibroblasts were purchased from the Cell Bank of the Chinese Academy of Sciences (Shanghai, China). Fibroblasts at passage 5–9 were used experimentally. Trypsin (0.25%, Gibco, Germany) was used to digest the fibroblasts until the cells were all resuspended. Fibroblasts were seeded into 96-well plates at a density of 1×10^4 cells per well and incubated for 12 h in Dulbecco's Modified Eagle's Medium (DMEM) (Hyclone, USA) containing 10% fetal bovine serum (FBS) (complete medium) (Gibco, Germany) at 37 °C in a humidified, 5% CO_2 atmosphere. After 12 h incubation, the complete medium was removed from each well and replaced with DMEM in absence of FBS (starvation medium) prior to a further 3 h incubation under identical growth conditions. After starvation for 3 h, complete medium containing DP at concentrations of 0 (control), 0.625, 1.25, 2.5, 5, 10, 20, and 40 μg/mL (n = 5 wells in triplicate plates) was added into every well respectively with 24 h treatment. In addition, 50 ng/mL epidermal growth factor (EGF) was regarded as the positive control group. At present, it has been reported that EGF gel promoted wound healing in rat model.[22] Many studies have reported that EGF significantly stimulated fibroblast proliferation, which is beneficial for wound healing.[23] After DP treatment, the cell counting kit-8 (CCK-8) assay was used to assess cell viability. Viable cells were measured at an absorbance (Abs) of 450 nm using enzyme-linked immune detector (Gene, China). Effective concentrations of DP were identified using the above experiment. NIH/3T3 cells were also treated with 0 (control), 1.25, 2.5, and 5 μg/mL DP for 0, 6, 12, 24 and 36 h separately and cell proliferation was determined using the CCK-8 as described previously. Cell viability was determined as follows:

$$\text{Cell viability}(\%) = \frac{\text{Abs of DP treated group}}{\text{Abs of control group}} \times 100\%$$

2.2. Western blot analysis

Phosphorylation of ERK in NIH/3T3 fibroblasts was determined after treatment with 2.5 μg/mL DP for 0, 15, 30, 60, and 120 min. At each time point, the total protein in cells was harvested and the proteins concentrations was detected dividely by using the Enhanced BCA Protein Assay Kit. The rest of the cell suspension was then aspirated and mixed with the sodium dodecyl sulfate polyacrylamide gel electrophoresis (SDS-PAGE) loading buffer in a ratio of 1: 4. Equal amounts of proteins were separated by SDS-PAGE and electrotransferred to polyvinylidene fluoride (PVDF) membranes. The membranes were incubated in tris-buffered saline (TBS) containing 5% skimmed milk and 0.1% Tween-20 for 60 min, and blotted with primary antibodies at 4 °C overnight.

The following primary antibodies were used: anti-phospho-ERK1/2 (1:1000, No. 4370, Cell Signaling Technology, MA, USA), anti-ERK1/2 (1:1000, No. 4695, Cell Signaling Technology), and anti-GAPDH (glyceraldehyde-3-phosphate dehydrogenase, 1:1000, No. 97166, Cell Signaling Technology). The membranes were incubated for 2 h with anti-mouse or anti-rabbit horseradish peroxidase-conjugated secondary antibodies (1:2000, Cell Signaling Technology). Reaction products were visualized by detection of chemiluminescence using an ECL Western Blotting Detection System (GE Healthcare, Piscataway, NJ, USA). Quantification of relative band densities was performed by scanning densitometry using Image J software (National Institute of Health, Bethesda, MD, USA). Gray intensity of p-ERK/ERK was calculated by the following formula:

$$\text{Gray intensity of p}-\text{ERK/ERK} = \frac{\text{Gray intensity of p}-\text{ERK}}{\text{Gray intensity of ERK}}$$

2.3. RNA interference experiments

To further verify whether DP promoted fibroblast proliferation via the ERK pathway, siRNA for ERK (No. 6560, Cell Signaling Technology, USA) was selected to block ERK signal (forward sequence: CCUCCAACCUGCUCAUCAA; reverse sequence: UUGAUGAGCAGGUUGGAGG). NIH/3T3 fibroblasts were transfected with ERK siRNA using Lipofectamine2000 (Lipo2000, Invitrogen, Japan) and OPTI-MEM (Invitrogen, Japan) according to the manufacturer's protocol. The final concentration of siRNA (ERK) was 100 nM, siRNA control (No. 6568, Cell Signaling Technology, USA) and Lipo2000 were used as control groups. The transfected cells were used experimentally after 48 h. All cells were treated with or without 2.5 μg/mL DP. The experiments were divided into control groups (siRNA control using Lipo2000, with or without DP treatment), Lipo2000 control groups (only Lipo2000, with or without DP treatment) and siRNA ERK groups (siRNA ERK using Lipo2000, with or without DP treatment). The ERK expression was detected after 120 min drug treatment and cell viability was detected after 24 h drug treatment.

PD98059 (9900S, Cell Signaling Technology, USA) is regarded as an ERK signal inhibitor and can reduce the level of ERK phosphorylation. The four experimental groups included[1] control group (without DP and inhibitor),[2] inhibitor group (PD98059 only),[3] drug-treated group (2.5 μg/mL DP only), and[4] drug-inhibitor group (2.5 μg/mL DP + PD98059). The inhibitor was diluted with complete medium and exposed to cells for 24 h. And then every group was treated with or without DP for 120 min. Densities of p-ERK and ERK were examined by Image J software. The density ratio of p-ERK/ERK was calculated and cell viability was assessed by CCK-8 in all groups.

2.4. In vivo rat wound models to determine the effect of DP in wound healing

The design of the current experiment had restrictively followed the guidelines of the Association for Assessment and Accreditation of Laboratory Animal Care, International. After getting the

permission to conduct the Committee on Research Animal Care of Northeast Agricultural University, a total of one hundred Wister rats (male and female, aged 6–8 weeks, weighing 240–260 g) were used in the study. Animals were maintained under standard laboratory conditions and fed food and water freely for a week. DP ointment was made by dissolving DP in dimethyl sulfoxide (DMSO) and Vaseline. Firstly, different qualities (50, 100 and 200 μg) of DP were dissolved in 1 mL DMSO. The final concentrations of solution were 50 μg/mL, 100 μg/mL and 200 μg/mL respectively. And then 1 mL above solutions were mixed with 19 mL Vaseline (16 g) respectively. The DP ointment concentrations were 2.5 μg/mL, 5 μg/mL and 10 μg/mL. The experiment included control group (Vaseline), DMSO group (1 mL DMSO was mixed with 16 g Vaseline), low- (2.5 μg/mL), middle- (5 μg/mL) and high- (10 μg/mL) dose DP groups. After sectionalization, rats were anesthetized by intraperitoneal injection with 10% chloral hydrate (0.35 mL/100 g). Following dorsum shaving and antisepsis, two circular full-thickness wounds were performed by biopsy punch (10 mm diameter). Rats (n = 20/group) were given ointment treatment twice daily. Wound images were captured using a camera (Cannon) at 0, 3, 7, and 14 days, and a ruler was used as a reference criterion. Wound healing area was analyzed using IPP software to calculate the wound healing rate using the formula:

$$\text{Wound healing rate} = \frac{\text{Wound area}(0) - \text{Wound area}(t)}{\text{Wound area}(0)} \times 100\%$$

2.5. Immunohistochemical analysis of SERPINH1 and calculation of fibroblasts density

After treatment with or without DP for 7 days in rat wound models, skin tissue samples were stained with anti-rabbit SERPINH1 (1:500; CST SERPINH1-positive cells were identified as fibroblasts). After several washes in PBST, samples were incubated for 30 min at 37 °C with anti-rabbit IgG (1:500; Molecular Probes, Life Technologies). The positive cells were then colored by DAB and hematoxylin. Sections were then sealed with neutral resin and mounted with cover slips. Images were captured using NIS-Elements F2.3 software and the proliferation density was calculated as the mean number of positive cells in five randomly selected high-power fields of view.

2.6. Western blot analysis

Rat wound skin tissues were collected at day 7 and homogenized in a glass pestle in 1 mL RIPA buffer containing 10 μL protease inhibitor and 10 μL Na_3VO_4 at 4 °C. ERK protein detection was carried out as described previously in Section *In vivo* rat wound models to determine the effect of DP in wound healing above.

2.7. Statistical analysis

Data were analyzed by SPSS16.0 software. All data were expressed as means ± standard deviation (SD). The t test was used to identify differences between two groups and one way ANOVA was used to identify differences among multi-groups, followed by LSD test. A p value < 0.05 was considered statistically significant.

3. Results

3.1. DP promoted NIH-3T3 cell proliferation

As shown in Fig. 1A, we found that EGF (positive control group) significantly stimulated fibroblast proliferation ($p < 0.01$ vs. control group). DP promoted fibroblast proliferation at a concentration range of 0.625–10 μg/mL, with a peak at 2.5 μg/mL. However, when DP was used at a concentration >20 μg/mL, fibroblast proliferation was inhibited ($p < 0.01$). These data demonstrated that DP positively influenced fibroblast proliferation at an optimal concentration range. Furthermore, when DP was at a concentration range of 1.25–5 μg/mL, cell viability was significantly increased compared with other groups ($p < 0.01$). Consequently, the cell proliferation assays were carried out in accordance to these data and determined that cell viability was higher in the DP-treated groups compared with the control group after 12 h treatment ($p < 0.01$). After this time point, the positive effect of DP on cell proliferation was more obvious. In the three drug-treated groups, DP at 2.5 μg/mL was identified as the best treatment concentration (Fig. 1B), which was used for subsequent experiments.

3.2. DP stimulated NIH/3T3 proliferation via the ERK signaling pathway

To further explore the molecular mechanism of DP-induced cell proliferation, Total ERK and p-ERK were detected at 0, 15, 30, 60, and 120 min in the absence or presence of DP (Fig. 2A and B). As shown in Fig. 2A, DP treatment did not change total ERK immunoreactivity, however, p-ERK significantly increased after DP treatment in a time-dependent manner ($p < 0.01$).

In the following experiment, fibroblasts were transfected with ERK siRNA using Lipo2000 and Opti-MEM, as shown in Fig. 2C, expression of ERK in fibroblasts was decreased obviously compared with cells transfected with siRNA control or Lipo2000 ($p < 0.01$). Moreover, SiRNA-mediated knockdown of ERK1/2 expression blocked DP-induced fibroblasts proliferation ($p < 0.01$). Additionally, we found that Lipo2000 had no influence on DP-treated fibroblasts proliferation and ERK expression in cells ($p > 0.05$). When Lipo2000 acted alone on cells and the DP-treated cells increased significantly compared with the cells without DP treatment ($p < 0.01$). At the same time, the results also showed that proliferation of cell enhanced evidently than DP-treated cells blocked by siRNA ERK ($p < 0.01$) (Fig. 2D).

In the presence of the ERK1/2 inhibitor PD98059, we clearly found that p-ERK decreased significantly than drug treated group without inhibitor treatment ($p < 0.01$), and was slightly increase compared with control group ($p > 0.05$) (Fig. 2E and F). Then DP-induced cell proliferation was abrogated under the treatment of DP ($p < 0.01$), but continued to be significantly enhanced compared with the control group ($p < 0.05$) (Fig. 2G). Taken together, our results indicated that DP promoted cell proliferation via phosphorylating the ERK signaling pathway.

3.3. DP induced rat wound healing

After establishing the rat trauma *in vivo* models, wounds were treated with either DP or Vaseline and DMSO (as control groups), and wound was recorded using a camera. There was no significant difference between the drugs treated groups and control group after three days of drug treatment. At day 7, the wound healing rate was significant increase in the DP-treated group compared with the control group (Fig. 3A and B, $p < 0.01$) and by day 14, the wound in the high-dose group had healed to a greater extent compared with the other groups. Moreover, we found that DMSO did not cause wound healing ($p < 0.01$ vs. DP-treated group; $p > 0.05$ vs. Vaseline group.). These findings confirmed that DP promoted wound healing in a dose-dependent manner. Amazingly, no obvious scars were found in eyes view when executed our experiment. Therefore we speculated that DP inclined not to trigger fibroblasts aberrant proliferation. In the future we will focus on the effects of DP on the scar in wound healing process.

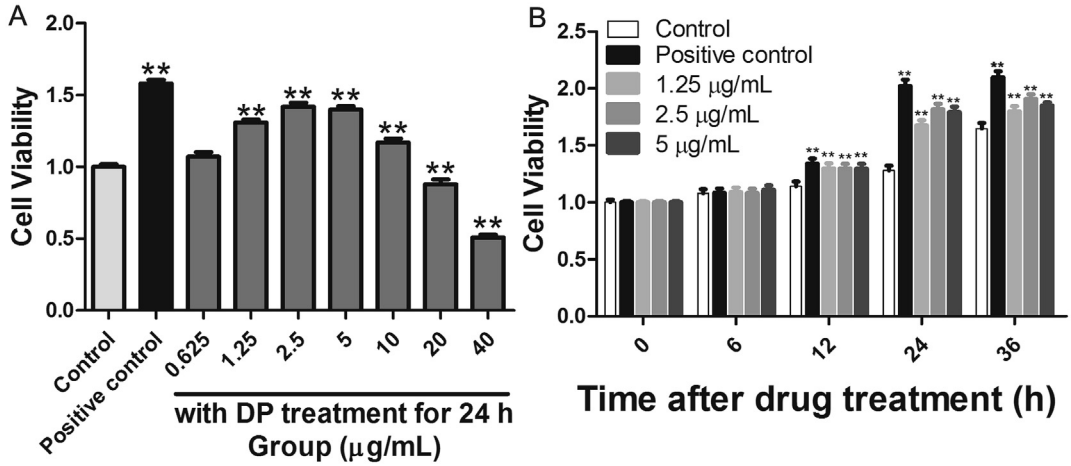

Fig. 1. Cell proliferation assays and cell migration assays. (A). Fibroblasts were treated with different concentrations (0–40 μg/mL) of DP and EGF (positive control group) for 24 h and cell viability was determined using CCK-8. **(B)**. DP acted on cells at 1.25, 2.5 and 5 μg/mL for 6, 12, 24 or 36 h. Cell viability was measured at the indicated time points. (Data are presented as means ± SD, n = 15 for each bar; *p < 0.05; **p < 0.01 vs. control group at same time).

3.4. DP enhanced fibroblast proliferation and upregulated p-ERK in skin tissue wounds

SERPINH1 antibody was used as a specific marker to identify fibroblasts in skin tissues. After 7 days of treatment with and without DP, skin samples were analyzed by immunohistochemistry. In Fig. 4A, the results showed that an increased number of SERPINH1-positive cells were found in DP treated groups ((b) low-, (c) medium-, and (d) high-dose groups) compared with the control group ((a) control group). Fibroblast density was calculated and showed in Fig. 4B. These findings indicated that DP significantly promoted the proliferation of fibroblasts in the wound tissue ($p < 0.01$) in a dose-dependent manner.

Significant upregulation of p-ERK were detected in the rat skin wounds of the DP-treatment groups compared with control group at day 7, we also found DP significantly upregulated p-ERK in the wound tissue ($p < 0.01$) in a dose-dependent manner (Fig. 4C and D).

4. Discussion

Wound healing is a complex biological process involving numerous cellular activities and molecules, and can be divided into three stages: initial inflammation, fibroblasts proliferation and migration, and final tissue reconstruction.[24] Fibroblasts proliferation and migration are critical during wound healing. Our experimental results showed that DP was effective in promoting the proliferation of fibroblasts. Fibroblasts are the most vital cells for extracellular matrix production and remodeling, and proliferation and migration of fibroblasts are beneficial for forming wound granulation tissues and further wound healing.[25] Moreover, we found that DP inhibited fibroblast proliferation at a concentration higher than 20 μg/mL. However, *in vivo* experiments, 2.5, 5 and 10 μg/mL DP ointments all promoted wound healing in dose-dependent manner. We speculated that in-vitro fibroblast cells were less tolerant than tissues (*in vivo* study). Many studies have demonstrated that the extracts of natural plants caused cell proliferation, playing a positive role when used within an optimal concentration range. However, negative effects using the same extracts are often observed when their concentrations are too high.[26] More recently, it was reported that the inhibitory effect of DP on cells increased caspase-9 expression and inhibited the expressions of PI3K/Akt and NF-kB.[27] Moreover, aberrant proliferation and activation of fibroblasts are closely associated with scar formation.[28] Interestingly, it has been recognized that being an important part of granulation tissue, collagen plays a pivotal role in striking a controlled delicate balance between fibroblasts proliferation and apoptosis, thereby regulating skin wound healing.[29]

ERK is one of the most widely studied proteins whose relationship with proliferation is now realized in many cell types. The ERK signaling pathway situated at the intersection of thousands of different cellular signals is highly complex and acts to modulate numerous cellular activities.[30] A further research is necessarily needed to identify whether DP directly or indirectly activates ERK. A large number of studies have revealed the pharmacological effects of many natural plant extracts on cells, and the natural plant extracts preferentially recognize the growth factor receptors on the cell surface, such as EGF receptor (EGFR), FGF receptor, PDGF receptor and so on. As previously described, flavonoids (dracorhodin is a flavonoid[31]) can activate EGFR, which triggers the Ras/Raf/MEK/MAPK pathway, the PI3-K/PTEN/Akt/mTOR pathway, and the STAT signaling cascade.[32] Similarly, in our study, we determined that DP upregulated ERK phosphorylation level, a member of MAPK family, therefore we speculated that DP-mediated p-ERK increase was influenced via EGFR molecular target activation. However, research work is going on in our lab, and we will investigate the effect of DP on EGFR and their involvement in proliferation. We also found that DP-induced cell proliferation was not inhibited completely by the treatment of siRNA and inhibitor. Thus, it is possible that ERK is not the only mediator for DP treatment. Therefore, the present research is valuable. In fact, an increasing number of signal transduction pathways involving ERK have been identified. The MEK/ERK pathway is involved in the differentiation of cells and the formation of collagen during tissue regeneration.[33] In a study by Fujiwara et al., L-arginine was found to promote fibroblast proliferation via activation of the amino acid receptor, GPRC6A first and of the ERK/cyclic-AMP response element binding (CREB) signaling pathway then.[34] These findings are consistent with our results. Furthermore, keratinocyte growth factor (KGF) and EGF have been reported to involve fibroblast proliferation.[35,36] KGF is weakly expressed in human skin but strongly upregulated in fibroblasts after skin injury. Because KGF is a highly specific and potent mitogen for keratinocytes,[37] this finding suggested that dermally derived KGF stimulated wound re-epithelialization in a paracrine manner. In another study, it has been reported that acemannan stimulates gingival fibroblast proliferation, which proliferate and secrete several

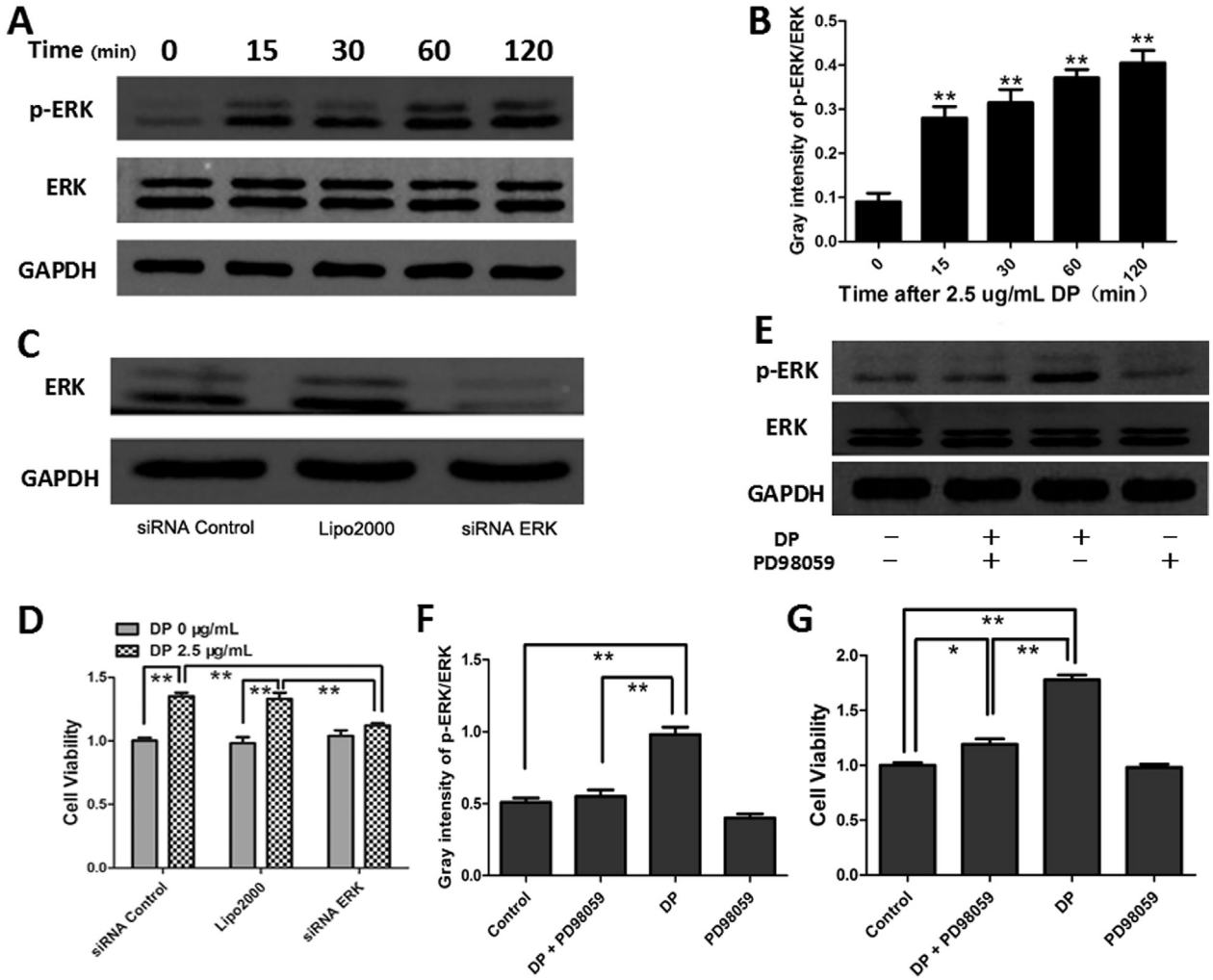

Fig. 2. Detection of the level of ERK phosphorylation. Cells at a 60% density were treated with or without 2.5 μg/mL DP for 0, 15, 30, 60 and 120 min. **(A)**. The activities of ERK, was analyzed by immunoblotting. Densitometry measurements for p-ERK was normalized to the amount of total ERK. Results were presented as the fold change compared with the control group. **(B)**. Gray intensity of p-ERK/ERK was measured using Image J software at different time points. **(C)**. Detection of ERK expression with or without the transfection of siRNA. NIH/3T3 fibroblasts were transfected with ERK siRNA, siRNA control or Lipo2000 for 48 h and then were used for experiment. **(D)**. Cell proliferation (treated for 24 h) was determined when the ERK signaling was blocked by RNA interference. **(E & F)**. Effects of ERK inhibitor (PD98059) on ERK signaling pathway in fibroblasts. The inhibitor was diluted with complete medium to indicated concentration and exposed to cells for 24 h. **(G)**. The cell viability (treated for 120 min) was examined by the action of the inhibitor, drug-inhibitor group ***(2.5 μg/mL DP + PD98059)*** was compared to the other groups (***(1) control group (without DP and inhibitor)***, (***2) inhibitor group (PD98059 only)***, (***3) drug-treated group (2.5 μg/mL DP only)***). (Data are presented as means ± SD, n = 5 for each bar, *p < 0.05 and **p < 0.01 vs. control group.).

growth factors and extracellular matrix, such as keratinocyte growth factor-1 (KGF-1), vascular endothelial growth factor (VEGF), and type I collagen, to generate new tissue.[38] Similarly, EGF plays an important role in the wound healing process by the paracrine mechanism of fibroblasts. Zhao demonstrated that EGF promoted the proliferation of fibroblasts.[23] In Lluïsa Miró's study, he confirmed that Aldosterone induced myofibroblast proliferation and EGF secretion to regulate epithelial colonic permeability.[39] Taken together, fibroblast proliferation is associated with EGF and KGF secretion. In our study, we determined that DP promoted fibroblast proliferation, thus, we speculate that DP could induced EGF and KGF secretion. Research work is going on in our lab, and we will investigate the DP's activity on such factors.

During wound healing of skin injuries, granulation tissues which contain newly formed vessels, macrophages, fibroblasts, and extracellular matrix (ECM) appeared at the wounded areas. Some of ECM, such as type III collagen, and the number of fibroblasts have been found to increase in skin at 7 days after injury.[40] Furthermore, at 14 days after injury, myofibroblasts, which express alpha-smooth muscle actin and have the capacity for active motility, have also been observed at the edge of the granulation tissue.[41] Immunohistochemical staining analysis showed that the number of SERPINH1-immunopositive fibroblasts gradually increased until the 14th day, and those at day 14 after injury reached the peak of the proliferative phase. This result demonstrated that DP could enhance fibroblast proliferation after skin damage, which provided a hypothesis that increased numbers of fibroblasts likely promote the formation of collagen and blood vessels during wound healing.[42,43]

In conclusion, DP, the stable form of Dracorhodin, alleviates *in vitro* fibroblast proliferation and migration and induces *in vivo* wound healing in rats. Therefore this study shall provide strong evidence for further research in clinical cases whose wounds are difficult to heal. This study gives a preliminary exploration of DP in wound repair. Further studies will be needed to examine the molecular target of drug action in order to give a deeper insight into this field.

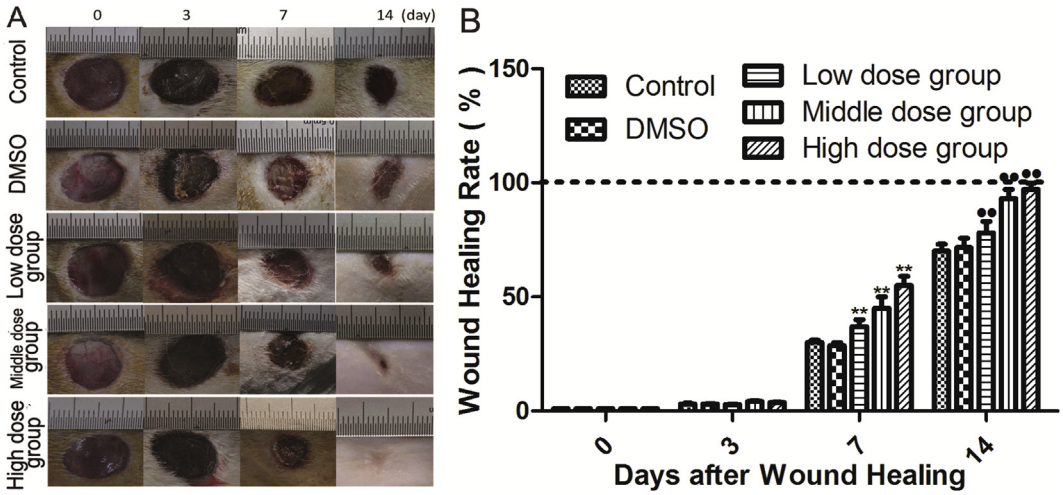

Fig. 3. Wound healing rate was calculate with or without DP treatment *in vivo* rat wound models. Wounds were photographed at day 0, 3, 7, and 14 in every group (control group (Vaseline), DMSO group, low- (50 μg/mL), middle- (100 μg/mL) and high- (200 μg/mL) dose DP groups). **(A)**. Photographs of wound at the specified times. **(B)**. The wound healing rate was calculated by IPP software (Data are presented as means ± SD, n = 20 for each bar, **/●●p < 0.01 vs. control group.).

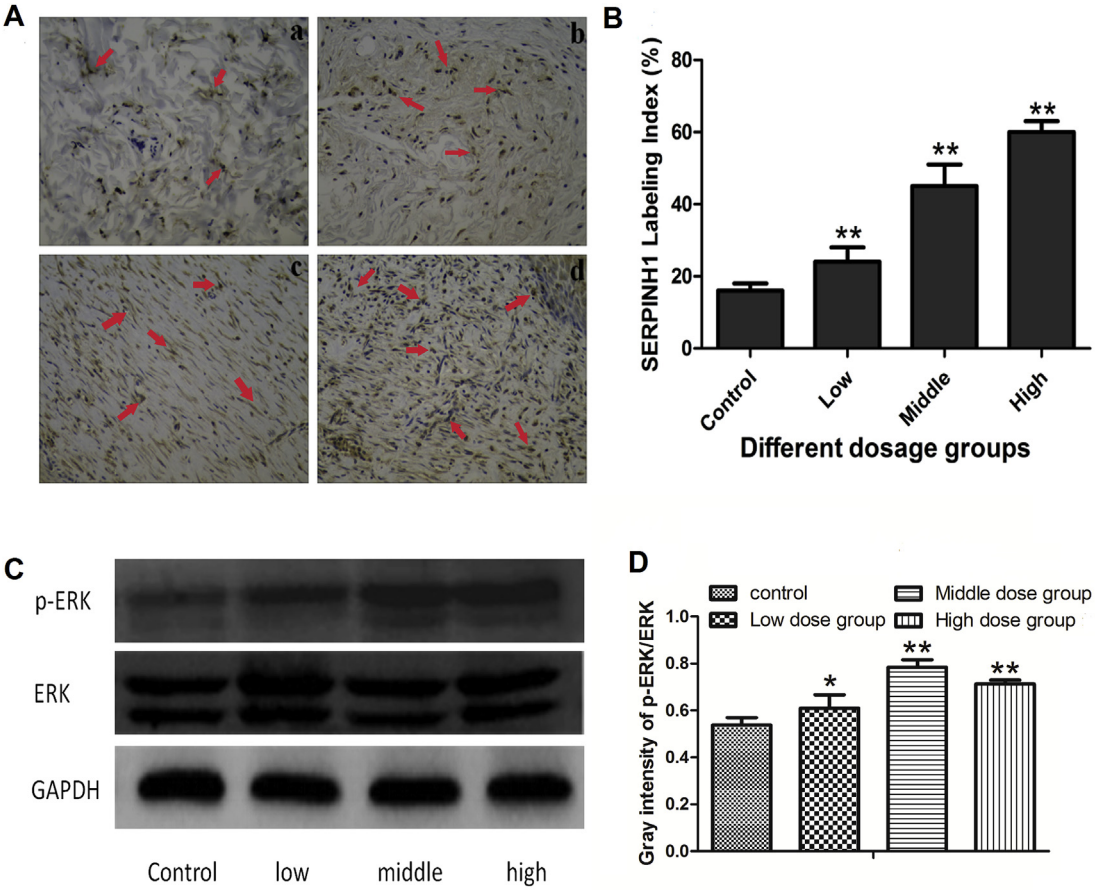

Fig. 4. Immunohistochemical analysis of SERPINH1 and p-ERK detection in wound tissues. Skin tissue samples in rat wound models were harvested and assessed immunohistochemically using SERPHINH1 antibody at day 7. **(A)**. Representative images of SERPHINH1 immunostaining in the wound granulation tissues in ***(a) control***, ***(b) low-***, ***(c) middle-***, and ***(d) high-dose groups***. **(B)**. Density of positive-cells was calculated as the mean number of positive cells in five randomly selected high-power fields of view in each images. (SERPHINH1-positive cells were marked by red arrows (➡). Data are presented as means ± SD, n = 20 for each bar, **p < 0.01 vs. control group. 200×). Rat Wound models were treated with and without DP for 7 days. The total protein was harvested from the wound granulation tissues in every rat. Western blot analysis was performed to examine p-ERK and ERK expression **(C & D)**. (Data are presented as means ± SD, n = 5 for each bar, *p < 0.05 and **p < 0.01 vs. control group.).

Conflicts of interest

The authors have declared that there is no conflict of interest.

Acknowledgement

This work was supported by Natural Science Foundation of China (No. 820065)

References

1. Wang J, Zhang CJ, Ni CW, et al. Haem-activated promiscuous targeting of artemisinin in *Plasmodium falciparum*. *Nat Commun*. 2015;6:10111.
2. Wong AS, Che CM, Leung KW. Recent advances in ginseng as cancer therapeutics: a functional and mechanistic overview. *Nat Prod Rep*. 2015;32(2):256.
3. Wojtyczka RD, Dziedzic A, Kępa M, et al. Berberine enhances the antibacterial activity of selected antibiotics against coagulase-negative Staphylococcus strains in vitro. *Molecules*. 2014;19(5):6583–6596.
4. Sverrisdóttir E, Lund TM, Olesen AE, Drewes AM, Christrup LL, Kreilgaard M. A review of morphine and morphine-6-glucuronide's pharmacokinetic–pharmacodynamic relationships in experimental and clinical pain. *Eur J Pharm Sci Off J Eur Fed Pharm Sci*. 2015;74:45–62.
5. Zhao JL, Lu Z, Dayanandan S, Nagaraju S, Liu DM, Li QM. Correction: tertiary origin and pleistocene diversification of dragon blood tree (Dracaena cambodiana-Asparagaceae) populations in the Asian tropical forests. *PLoS One*. 2013;8(4):e60102.
6. Yi T, Chen HB, Zhao ZZ, Yu ZL, Jiang ZH. Comparison of the chemical profiles and anti-platelet aggregation effects of two “Dragon's Blood” drugs used in traditional Chinese medicine. *J Ethnopharmacol*. 2011;133(2):796–802.
7. Risco E, Ghia FR, Iglesias J, et al. Immunomodulatory Activity and Chemical Characterisation of Sangre de Drago (Dragon's Blood) from Croton lechleri. *Planta Med*. 2003;69(9):785.
8. Li YS, Wang JX, Jia MM, Liu M, Li XJ, Tang HB. Dragon's blood inhibits chronic inflammatory and neuropathic pain responses by blocking the synthesis and release of substance P in rats. *J Pharmacol Sci*. 2012;118(1):43–54.
9. Gupta RK. Dragon's blood: botany, chemistry and therapeutic uses. *J Ethnopharmacol*. 2008;115(3):361.
10. Edward HG, de Oliveira LF, Quye A. Raman spectroscopy of coloured resins used in antiquity: dragon's blood and related substances. *Spectrochim Acta Part A Mol Biomol Spectrosc*. 2001;57(14):2831–2842.
11. Ubillas R, Jolad SD, Bruening RC, et al. SP-303, an antiviral oligomeric proanthocyanidin from the latex of Croton lechleri (Sangre de Drago). *Phytomed Int Phytother Phytopharm*. 1994;1(2):77–106.
12. Lopes MI, Saffi J, Echeverrigaray S, Henriques JA, Salvador M. Mutagenic and antioxidant activities of Croton lechleri sap in biological systems. *J Ethnopharmacol*. 2004;95(2–3):437–445.
13. Alonsocastro AJ, Ortizsánchez E, Domínguez F, et al. Antitumor effect of Croton lechleri Mull. Arg. (Euphorbiaceae). *J Ethnopharmacol*. 2012;140(2):438–442.
14. Li D, Hui R, Hu Y, Han Y, Guo S. Effects of extracts of Dragon's blood on fibroblast proliferation and extracellular matrix hyaluronic acid. *Zhonghua Zheng Xing Wai Ke Za Zhi = Zhonghua Zhengxing Waike Zazhi = Chin J Plast Surg*. 2015;31(1):53–57.
15. Li F, Jiang T, Liu W, Hu Q, Yin H. The angiogenic effect of dracorhodin perchlorate on human umbilical vein endothelial cells and its potential mechanism of action. *Mol Med Rep*. 2016;14(2).
16. Wong VW, Gurtner GC, Longaker MT. Wound healing: a paradigm for regeneration. *Mayo Clin Proc*. 2013;88(9):1022–1031.
17. Rolin GL, Binda D, Tissot M, et al. In vitro study of the impact of mechanical tension on the dermal fibroblast phenotype in the context of skin wound healing. *J Biomech*. 2014;47(14):3555–3561.
18. Jettanacheawchankit S, Sasithanasate S, Sangvanich P, Banlunara W, Thunyakitpisal P. Acemannan stimulates gingival fibroblast proliferation; expressions of keratinocyte growth factor-1, vascular endothelial growth factor, and type I collagen; and wound healing. *J Pharmacol Sci*. 2009;109(4):525.
19. Cui R, Lu Q, Teng Y, Li K, Li N. Chitosan promoted the corneal epithelial wound healing via activation of ERK pathway. *Curr Eye Res*. 2016:1–7.
20. Xu S, Zhao Y, Yu L, Shen X, Ding F, Fu G. Rosiglitazone attenuates endothelial progenitor cell apoptosis induced by TNF-α via ERK/MAPK and NF-κB signal pathways. *J Pharmacol Sci*. 2011;117(4):265.
21. Oka T, Ohta K, Kanazawa T, Nakamura K. Interaction between macrophages and fibroblasts during wound healing of burn injuries in rats. *Kurume Med J*. 2016;62(3–4):59.
22. Khanbanha N, Atyabi F, Taheri A, Talaie F, Mahbod M, Dinarvand R. Healing efficacy of an EGF impregnated triple gel based wound dressing: in vitro and in vivo studies. *BioMed Res Int*. 2014;2014(10):493732.
23. Zhao J, Li H, Liu J, Gong N, Chen L. The effects of cytokines in adipose stem cell-conditioned medium on the migration and proliferation of skin fibroblasts in vitro. *BioMed Res Int*. 2013;2013(3):578479.
24. Boateng JS, Matthews KH, Stevens HNE, Eccleston GM. Wound healing dressings and drug delivery systems: a review. *J Pharmaceut Sci*. 2008;97(8):2892–2923.
25. Decker CG, Wang Y, Paluck SJ, et al. Fibroblast growth factor 2 dimer with superagonist in vitro activity improves granulation tissue formation during wound healing. *Biomaterials*. 2015;81:157–168.
26. Ruszymah BH, Chowdhury SR, Manan NA, Fong OS, Adenan MI, Saim AB. Aqueous extract of Centella asiatica promotes corneal epithelium wound healing in vitro. *J Ethnopharmacol*. 2012;140(2):333–338.
27. Zhang P, Li J, Tang X, Zhang J, Liang J, Zeng G. Dracorhodin perchlorate induces apoptosis in primary fibroblasts from human skin hypertrophic scars via participation of caspase-3. *Eur J Pharmacol*. 2014;728(Complete):82–92.
28. Xiao YY, Fan PJ, Lei SR, Qi M, Yang XH. MiR-138/peroxisome proliferator-activated receptor β signaling regulates human hypertrophic scar fibroblast proliferation and movement in vitro. *J Dermatol*. 2015;42(5):485–495.
29. Bainbridge P. Wound healing and the role of fibroblasts. *J Wound Care*. 2013;22(8):410–412.
30. Cursons J, Gao J, Hurley DG, et al. Regulation of ERK-MAPK signaling in human epidermis. *BMC Syst Biol*. 2015;9(1):41.
31. Shen CC, Tsai SY, Wei SL, Wang ST, Shieh BJ, Chen CC. Flavonoids isolated from Draconis resina. *Nat Prod Res*. 2007;21(4):377.
32. Mikula M, Skrzypczak M, Goryca K, et al. Genome-wide co-localization of active EGFR and downstream ERK pathway kinases mirrors mitogen-inducible RNA polymerase 2 genomic occupancy. *Nucleic Acids Res*. 2016;44(21):10150–10164.
33. Hara T, Kakudo N, Morimoto N, Ogawa T, Lai F, Kusumoto K. Platelet-rich plasma stimulates human dermal fibroblast proliferation via a Ras-dependent extracellular signal-regulated kinase 1/2 pathway. *J Artif Organs*. 2016;19(4):1–6.
34. Fujiwara T, Kanazawa S, Ichibori R, et al. L-arginine stimulates fibroblast proliferation through the GPRC6A-ERK1/2 and PI3K/Akt pathway. *PLoS One*. 2014;9(3), e92168.
35. Yu A, Matsuda Y, Takeda A, Uchinuma E, Kuroyanagi Y. Effect of EGF and bFGF on fibroblast proliferation and angiogenic cytokine production from cultured dermal substitutes. *J Biomater Sci Polym Ed*. 2011;23(10):1315–1324.
36. Salvatore R, Laura L, Cristina S, Simonetta M, Rosaria TM, Maurizio B. Cholesteatoma-associated fibroblasts modulate epithelial growth and differentiation through KGF/FGF7 secretion. *Histochem Cell Biol*. 2012;138(2):251–269.
37. Werner S. Keratinocyte growth factor: a unique player in epithelial repair processes. *Cytokine Growth Factor Rev*. 1998;9(2):153–165.
38. Furuhashi I, Abe K, Sato T, Inoue H. Thrombin-stimulated proliferation of cultured human synovial fibroblasts through proteolytic activation of proteinase-activated receptor-1. *J Pharmacol Sci*. 2008;108(1):104.
39. Miró L, Pérez-Bosque A, Maijó M, Amat C, Naftalin RJ, Moretó M. Aldosterone induces myofibroblast EGF secretion to regulate epithelial colonic permeability. *Am J Physiol Cell Physiol*. 2013;304(9):918–926.
40. Natsuaki Y, Egawa G, Nakamizo S, et al. Perivascular leukocyte clusters are essential for efficient activation of effector T cells in the skin. *Nat Immunol*. 2014;15(11):1064–1069.
41. Kibe Y, Takenaka H, Kishimoto S. Spatial and temporal expression of basic fibroblast growth factor protein during wound healing of rat skin. *Br J Dermatol*. 2000;143(4):720–727.
42. Shabbir A, Cox A, Rodriguezmenocal L, Salgado M, Van BE. Mesenchymal stem cell exosomes induce proliferation and migration of normal and chronic wound fibroblasts, and enhance angiogenesis in vitro. *Stem Cells Dev*. 2015;24(14):1635.
43. Hata S, Okamura K, Hatta M, Ishikawa H, Yamazaki J. Proteolytic and non-proteolytic activation of keratinocyte-derived latent TGF-β1 induces fibroblast differentiation in a wound-healing model using rat skin. *J Pharmacol Sci*. 2014;124(2):230–243.

Journal of Pharmacological Sciences 136 (2018) 73–78

Contents lists available at ScienceDirect

Journal of Pharmacological Sciences

journal homepage: www.elsevier.com/locate/jphs

Full paper

Influence of chronic volume overload-induced atrial remodeling on electrophysiological responses to cholinergic receptor stimulation in the isolated rat atria

Xin Cao [a, c], Megumi Aimoto [a, c], Marie Fukumoto [b], Yoshinobu Nagasawa [a], Hikaru Tanaka [b], Akira Takahara [a, *]

[a] Department of Pharmacology and Therapeutics, Faculty of Pharmaceutical Sciences, Toho University, 2-2-1 Miyama, Funabashi, Chiba 274-8510, Japan
[b] Department of Pharmacology, Faculty of Pharmaceutical Sciences, Toho University, 2-2-1 Miyama, Funabashi, Chiba 274-8510, Japan

ARTICLE INFO

Article history:
Received 31 August 2017
Received in revised form
8 December 2017
Accepted 26 December 2017
Available online 16 January 2018

Keywords:
Aorto-venocaval shunt
Carbachol
Atrial fibrillation
Effective refractory period
Conduction velocity

ABSTRACT

Whereas molecular mechanisms of atrial fibrillation (AF) have been widely investigated, there is limited information regarding interrelation between chronic volume overload and parasympathetic nervous system in the pathophysiology of AF. In this study, we investigated the influence of abdominal aorto-venocaval shunt (AVS)-induced atrial remodeling on electrophysiological responses to cholinergic receptor stimulation in the isolated rat atria. Interstitial fibrosis, cardiomyocyte hypertrophy and atrial enlargement, known as structural arrhythmogenic substrates for AF, took place after one month of AVS operation. Carbachol at 0.1 and 1 μM shortened the effective refractory period, acting as functional arrhythmogenic substrates, but increased the conduction velocity both in the atria of the sham-operated and AVS rats. The extents of the electrophysiological responses to carbachol in the atria of the AVS rat were greater than those in the sham-operated ones. Also, the higher inducibility and longer duration of carbachol-mediated AF were detected in the AVS atria than those in the sham-operated ones. These results showed that chronic volume overload-induced atrial remodeling promoted electrophysiological responses to cholinergic receptor stimulation in the isolated atria of rats, suggesting possible synergistic actions between structural arrhythmogenic substrate in the remodeled atria and functional arrhythmogenic substrates modulated by parasympathetic nerve activity.

© 2018 The Authors. Production and hosting by Elsevier B.V. on behalf of Japanese Pharmacological Society. This is an open access article under the CC BY-NC-ND license (http://creativecommons.org/licenses/by-nc-nd/4.0/).

1. Introduction

Atrial fibrillation (AF) is one of the most common cardiac arrhythmias in clinical practice, which impacts on both life expectancy and quality of life.[1] Autonomic nervous system is well recognized as an important contributor in triggering and maintaining AF, of which activation of parasympathetic nerves shortens the atrial action potential duration and the effective refractory period, and increases dispersion of atrial repolarization,[2–4] thus creating functional arrhythmogenic substrates for AF.

Congestive heart failure and mitral valve diseases are also regarded as important risk factors for AF,[5] which can generate structural substrates through volume overload to the atria. The role of the parasympathetic nervous system or volume overload in the pathogenesis of AF has a long and rich history independently.[5,6] Whereas molecular control mechanisms of AF have been investigated widely, linked to gene expression, cell Ca^{2+} handling, and conduction disturbance,[7] interrelation between volume overload and parasympathetic nervous system in triggering and maintaining AF remains elusive. Recently, we established a rat model to deliver long-term volume overload to the heart by aorto-venocaval shunt (AVS) operation, where initiating trigger of AF, namely, increased automaticity in the pulmonary-vein myocardium could be found.[8] In that study, carbachol suppressed the spontaneous electrical activity in pulmonary-vein myocardium of AVS via a significant hyperpolarizing effect on the resting membrane potential, exerting an antiarrhythmic effect.[8] To clarify cholinergic modulation of arrhythmogenic properties in the atrium itself, we assessed the influence of chronic volume overload-induced atrial remodeling on

* Corresponding author.
E-mail address: akirat@phar.toho-u.ac.jp (A. Takahara).
Peer review under responsibility of Japanese Pharmacological Society.
[c] Equally contributed.

https://doi.org/10.1016/j.jphs.2017.12.009
1347-8613/© 2018 The Authors. Production and hosting by Elsevier B.V. on behalf of Japanese Pharmacological Society. This is an open access article under the CC BY-NC-ND license (http://creativecommons.org/licenses/by-nc-nd/4.0/).

electrophysiological responses to cholinergic receptor stimulation in the atria. This study may provide new insights into pathophysiology of interrelation between functional and structural substrates in AF.

2. Materials and methods

Experiments were performed by using 8-week-old male Wistar rats ($n = 37$), weighing approximately 150–200 g (Sankyo Labo Service, Tokyo, Japan). Animals were kept at 23 ± 1 °C under a 12-h light–dark cycle, where food and water were available *ad libitum*. All experiments were approved by the Animal Research Committee for Animal Experimentation at Faculty of Pharmaceutical Sciences of Toho University (No. 17-51-359) and performed in accordance with the Guidelines for the Care and Use of Laboratory Animal of Toho University.

Rats were randomly divided into two groups: sham group ($n = 19$) and AVS group ($n = 18$). Briefly, animals were anesthetized with pentobarbital sodium (50 mg/kg, i.p.). Then, rats in the AVS group received fistulation between the abdominal aorta and inferior vena cava by an 18-gauge needle, as described previously.[9] Rats in the sham group underwent similar operation procedure, but did not receive a fistulation. Four weeks later, histological and morphometric analyses in addition to electrophysiological testing were performed.

2.1. Histological examination

More than 4 weeks after the AVS surgery, the animals in the sham ($n = 2$) and AVS ($n = 2$) groups were anesthetized with pentobarbital sodium (50 mg/kg, i.p.). To prevent blood clotting, 1 mL of heparinized saline (100 IU/mL) was intravenously administered. Immediately after euthanization, beginning of the aorta was cannulated for retrograde perfusion with saline and vena cava was incised. The perfusion fixation with a 10% formalin neutral buffer solution was conducted through the cannula, and the segments were processed into paraffin blocks. Longitudinal sections ($n = 1$ for the sham group and $n = 1$ for the AVS group) in 4-μm-thick were cut that all four chambers of the heart were seen from the paraffinized tissue blocks. In addition, cross sections ($n = 1$ for the sham group and $n = 1$ for the AVS group) in 4-μm-thick were also cut from four chambers and mounted on charged slides. One slide each was stained with Masson trichrome to accentuate muscle and connective tissues. Microphotographs in the upper panel were taken by Aperio scanscope (Leica Microsystems K.K., Tokyo) at 4× (objective), and in the lower at 20× (objective).

2.2. Morphometric examination

For morphometric examination, the hearts were immediately dissected and blotted dry in the sham ($n = 8$) and AVS groups ($n = 8$). Right and left ventricles, interventricular septum, and atrium were separated and weighed. Body weight was also measured and used for normalization of heart masses (Table 1). The wall thickness was measured at the thickest part where was identified with naked eye.

2.3. Electrophysiological testing

The isolated atrial preparation consisted of the entire right and left atrium from sham ($n = 9$) and AVS ($n = 8$) groups, which was incubated with the Krebs–Henseleit solution of the following composition (in mM): NaCl 118.4, KCl 4.7, $CaCl_2$ 2.5, $MgSO_4$ 1.2, KH_2PO_4 1.2, $NaHCO_3$ 24.9, glucose 11.1, gassed with 95% O_2/5% CO_2 (pH 7.4 at 37 °C). Electrophysiological parameters were recorded as described previously.[10,11] Carbachol at 0.1 and 1 μM was added to isolated atria of the sham and AVS groups. After obtaining electrophysiological data of 1 μM carbachol, atropine at 10 μM was additionally applied to the atria ($n = 3$ for each group) to confirm association of muscarinic receptors. Briefly, the stimulating and recording electrodes for measuring intra-atrial conduction time were attached on the atrial epicardium close to the sinus nodal region and on the left atrial appendage, respectively. On the other hand, the stimulating electrode for burst pacing was attached on the septum of atria. Electrograms were amplified with a bioelectric amplifier (AB-621G; Nihon Kohden, Tokyo, Japan) and fed into a computer-based data acquisition system (PowerLab, ADInstruments, Castle Hill, Australia). The preparation was electrically driven at cycle lengths of 200, 150, or 100 ms using an electrical stimulator (SEN-7203, Nihon Kohden) and an isolator (SS-104J, Nihon Kohden) with rectangular pulses (about 1.5 times of the diastolic threshold voltage and 3-ms width). The effective refractory period of right atria was assessed by a pacing protocol consisting of ten beats of basal stimuli (S_1) in cycle lengths of 200, 150, or 100 ms followed by an extra stimulus (S_2) of various coupling intervals. The intra-atrial conduction time was measured as the difference between right and left atrial electrograms to calculate the intra-atrial conduction velocity. The pacing cycle lengths were set shorter than those during spontaneous sino–atrial activity, which were around 220–250 ms. Atrial tachyarrhythmia was induced by pacing at the septum of atrium with burst pacing (5 V output; 3-ms pulse width; 10-ms cycle length for 30 s) for 10 times. An episode of more than 3 continuous premature atrial contractions and/or atrial tachyarrhythmia such as AF and atrial flutter (AFL) lasted for 30 s were regarded as an incidence of AF/AFL. AF/AFL duration was expressed as an average of the 10 times of burst pacing. All experiments were performed at 36.5 ± 0.5 °C.

Table 1
Morphometric parameters.

Parameters	Sham	AVS
Body weight (g)	274 ± 6	282 ± 6
Heart weight (mg)	761 ± 29	1234 ± 48****
Heart weight (mg)/body weight (g)	2.8 ± 0.1	4.4 ± 0.2****
Atrial weight (mg)	78 ± 5	145 ± 11****
Ventricular weight (mg)	684 ± 26	1089 ± 43****
RV weight (mg)	131 ± 4	212 ± 13****
LV weight (mg)	553 ± 27	877 ± 33****
RV wall thickness (mm)	1.2 ± 0.0	1.7 ± 0.1***
Septal thickness (mm)	2.6 ± 0.2	3.4 ± 0.1****
LV wall thickness (mm)	3.8 ± 0.1	5.1 ± 0.2****

Data are presented as mean ± S.E.M. ($n = 8$ for each group). ***$P < 0.001$, ****$P < 0.0001$ vs. Sham. RV: right ventricle; LV: left ventricle; AVS: aorto-venocaval shunt.

2.4. Drugs

Carbachol and atropine sulfate were purchased from Sigma–Aldrich (catalog # 074K0777, St. Louis, MO, USA) and Wako Pure Chemical (catalog # 015-4853, Osaka), respectively, which were dissolved in distilled water. Small aliquots were added to the organ bath to obtain the desired final concentration. All the other chemicals were commercial products of the highest available quality. The concentration of carbachol was determined by previous studies, in which the low concentration (0.1 μM) was reported to produce physiological responses mimicking parasympathetic nerve activity at night or rest time.[8,12]

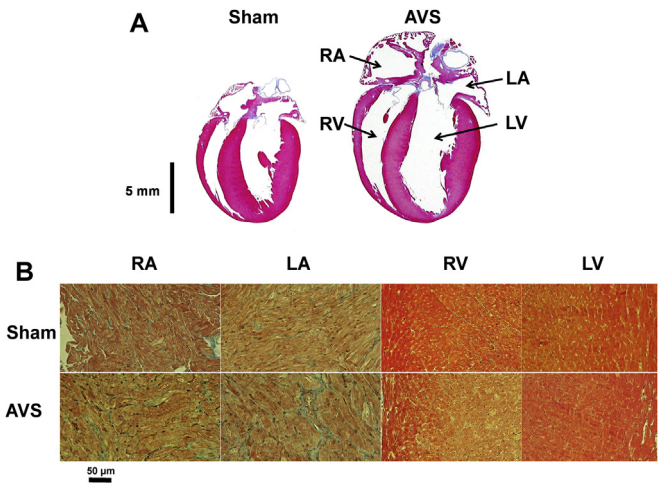

Fig. 1. Tissue sections of the heart after Masson's trichrome staining in the sham-operated ($n = 1$) and AVS ($n = 1$) rats. (A) Longitudinal sections showed a significant enlargement of both atrial and ventricles of the AVS rat one month after the operation. The vertical black bar indicates a scale of 5 mm. (B) Cross sections in sham group ($n = 1$) are shown in the upper panel, and the ones in AVS group ($n = 1$) corresponding to the upper ones are indicated in the lower panel. Note that atrial myocyte hypertrophy and fibrosis occurred in the AVS atria. The horizontal black bar indicates a scale of 50 μm. RA: right atrium; LA: left atrium; RV: right ventricle; LV: left ventricle; AVS: aorto-venocaval shunt.

2.5. Statistical analysis

All data are expressed as mean ± standard error of mean (S.E.M.). The statistical significances within a parameter were evaluated by one-way repeated-measures ANOVA followed by Contrasts for mean values comparison, whereas those between the groups were analyzed by unpaired *t*-test. A *P*-value less than 0.05 was considered significant.

3. Results

3.1. Histology of the heart

Typical photos of the heart obtained from the sham-operated and AVS rats are shown in Fig. 1. Macroscopic analysis (Fig. 1A) from longitudinal sections indicated a significant enlargement of both atrial and ventricles in the AVS rat. Microscopic study from cross sections revealed that atrial narrow myocytes were well aligned and surrounded by little interstitial tissue in the sham-operated rat, whereas atrial myocytes were enlarged and surrounded by fibrosis in the AVS rat (Fig. 1B). Similar morphological results were also obtained in another series of our experiment using the same animal model (data not shown).

3.2. Morphometric examination

Four weeks after the AVS surgery, the body weights in the sham and AVS groups were alike (Table 1), whereas significant differences were detected in the heart weight, the ratio of heart-weight/body-weight, atria and ventricle weights, wall thickness of right ventricle, left ventricle and septum between sham-operated and AVS animals (Table 1).

3.3. Electrophysiological testing

Fig. 2 shows typical traces of electrograms obtained from the right and left atrium in the sham-operated (left panel) and AVS rats (right panel), whereas Table 2 summarizes the control values of effective refractory period and conduction velocity in sham and AVS atria before carbachol application. The effective refractory period in the AVS group was significantly longer than those in the sham group. The conduction velocity in the AVS group was relatively less than those in the sham group, which did not achieve statistical significance. Figs. 3 and 4 summarize effects of carbachol

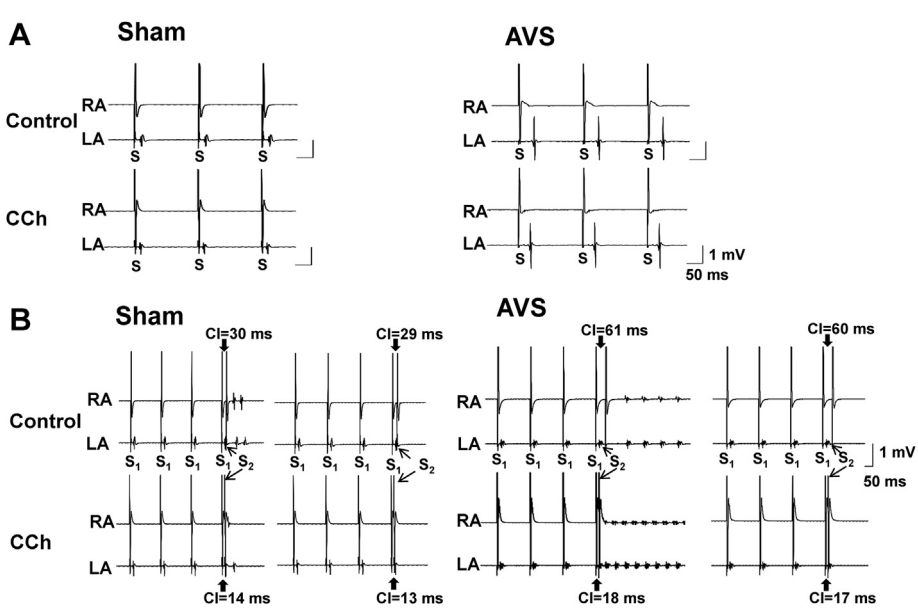

Fig. 2. Typical traces of electrograms obtained from atria in the sham-operated (left panel) and AVS (right panel) rats before and after application of carbachol at 1 μM. The preparation was electrically driven at a pacing cycle length of 200 ms. (A) Conduction velocity between the right and left atrium was delayed in the AVS rat than that in the sham-operated one. (B) Effective refractory period of the right atrium was longer in the AVS rat than that in the sham-operated one. Note that atrial tachyarrhythmia occurred in the AVS atria at coupling interval of 61 ms (before carbachol) and 18 ms (after carbachol). Conduction block and/or conduction delay appeared between right and left atria of AVS at coupling interval of 61 ms. S_1 and S_2 indicate the basal stimuli and an extra stimulus of various coupling intervals, respectively. CCh: carbachol; AF: atrial fibrillation, AFL: atrial flutter; S: electrical stimulation; CI: coupling interval; AVS: aorto-venocaval shunt; RA: right atrium; LA: left atrium.

Table 2
Electrophysiological parameters.

Parameters	PCL	Sham	AVS	
Effective refractory period (ms)	200 ms	42.6 ± 3.2	57.4 ± 4.8	$P < 0.05$
	150 ms	44.3 ± 3.4	58.4 ± 5.1	$P < 0.05$
	100 ms	46.4 ± 3.4	59.7 ± 5.5	$P = 0.12$
Conduction velocity (m/s)	200 ms	0.55 ± 0.12	0.46 ± 0.07	$P = 0.54$
	150 ms	0.54 ± 0.13	0.43 ± 0.07	$P = 0.48$
	100 ms	0.47 ± 0.11	0.33 ± 0.05	$P = 0.28$

Data are means ± S.E.M. ($n = 9$ for sham group and $n = 8$ for AVS group). AVS: aorto-venocaval shunt. PCL: pacing cycle length.

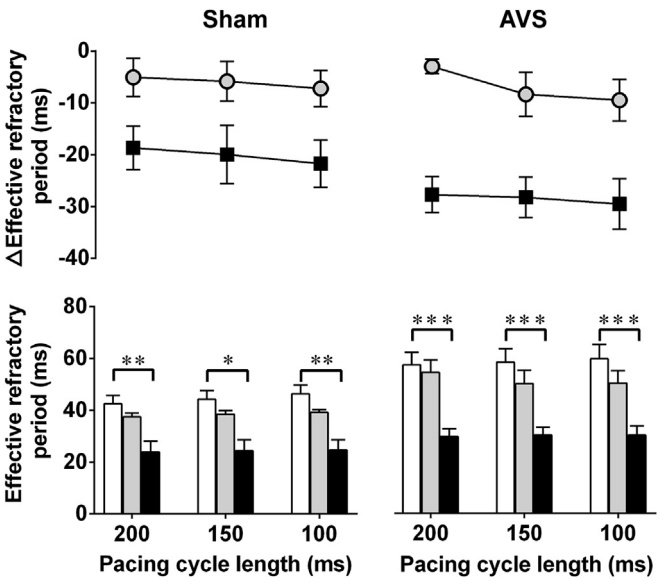

Fig. 3. Effective refractory period after carbachol application of the atria in the sham-operated ($n = 9$) and AVS ($n = 8$) rats. Effects of pre-drug control (white), carbachol at 0.1 (grey) and 1 μM (black) on atria effective refractory period were recorded at pacing cycle lengths of 200, 150 and 100 ms both in the sham-operated and AVS rats. Upper panel shows the extents of carbachol-induced changes. Data are presented as mean ± S.E.M. $^{*}P < 0.05$, $^{**}P < 0.01$, $^{***}P < 0.001$. AVS: aorto-venocaval shunt.

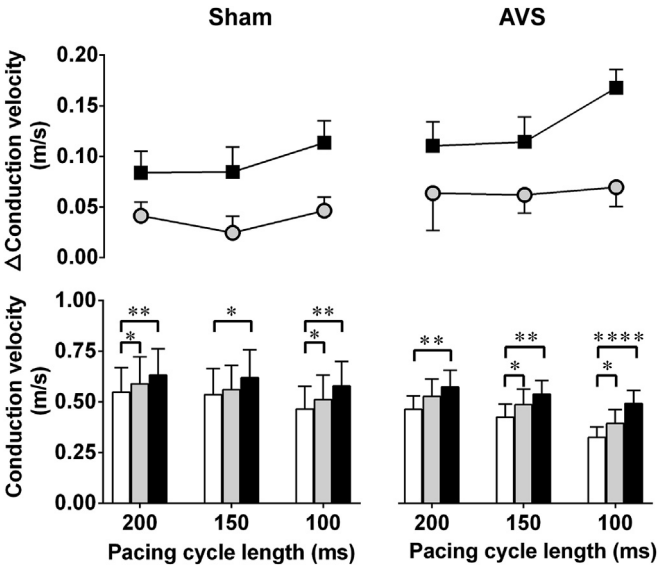

Fig. 4. Conduction velocity in the atria after carbachol application in the sham-operated ($n = 9$) and AVS ($n = 8$) rats. Effects of pre-drug control (white), carbachol at 0.1 (grey) and 1 μM (black) on the conduction velocity were recorded at pacing cycle lengths of 200, 150 and 100 ms both in the sham-operated and AVS rats. Upper panel shows the extents of carbachol-induced changes. Data are presented as mean ± S.E.M. $^{*}P < 0.05$, $^{**}P < 0.01$, $^{****}P < 0.0001$. AVS: aorto-venocaval shunt.

on the effective refractory period and conduction velocity, respectively, in the atria. Carbachol at 0.1 μM tended to shorten the effective refractory period in both sham and AVS atria, and at 1 μM it significantly shortened the effective refractory period at all pacing cycle lengths in both sham and AVS atria when compared with pre-drug control. Their extents were greater in the AVS atria than those in the sham atria (Fig. 3 upper). Carbachol at 0.1 μM significantly increased the conduction velocity in the AVS atria at pacing cycle lengths of 150 and 100 ms, and in sham atria at pacing cycle lengths of 200 and 100 ms when compared with pre-drug control. Carbachol at 1 μM significantly increased the conduction velocity at all pacing cycle lengths in both sham and AVS atria when compared with pre-drug control. Their extents were relatively greater in the AVS atria than those in the sham ones (Fig. 4 upper).

Typical traces of AFL induced by burst pacing in an AVS rat atrium before and after carbachol treatment are shown in Fig. 5A, and the AF/AFL inducibility as well as duration in both sham and AVS group is summarized in Fig. 5B. There were no significant differences in control values of AF/AFL inducibility or duration between the sham and AVS groups. Carbachol at 0.1 and 1 μM increased AF/AFL inducibility from 50% to 100% in the AVS atria, but hardly altered it in the sham atria. On the other hand, carbachol at 0.1 and 1 μM significantly prolonged the AF/AFL duration in the AVS atria when compared with pre-drug control, whereas hardly altered it in the sham atria.

Atropine at 10 μM reversed the carbachol (1 μM)-induced abbreviation of effective refractory period and acceleration of conduction velocity both in the sham and AVS atria ($n = 3$ for each group), and completely suppressed the carbachol (1 μM)-mediated AF/AFL in the AVS atria ($n = 3$).

4. Discussion

In this study, we assessed the influence of chronic volume overload-induced atrial remodeling on electrophysiological responses to cholinergic receptor stimulation in the atria. As shown in Fig. 1 and Table 1, interstitial fibrosis, cardiomyocyte hypertrophy and atrial enlargement, which are shown to be structural arrhythmogenic substrates for AF,[13] took place after one month of AVS operation. The electrophysiological responses to carbachol in the remodeled atria were directionally similar to those in the sham ones, but the extents were greater. Also, the higher inducibility and longer duration of carbachol-mediated AF/AFL were detected in the AVS atria than those in the sham ones.

4.1. Characteristics of AVS-remodeled atria

The effective refractory period in the AVS atrium was longer than that in the sham group (Table 2). In our previous study, the action potential duration of the pulmonary vein myocardium in the AVS rat is longer than that in the sham-operated rat (97.8 ms vs 64.6 ms).[8] Thus, similar electrophysiological change might be also involved in the AVS atria. On the other hand, the conduction velocity in the AVS atria tended to be decelerated, as shown in Fig. 2 and Table 2, which may be in part associated with interstitial fibrosis as observed both in the right and left atria of the AVS rat (Fig. 1). These characteristics of atrial conduction and refractoriness in the AVS rat are essentially in accordance with those in the atria of the canine model of congestive heart failure.[14] Generally, prolongation of effective refractory period is considered to be antiarrhythmic, whereas conduction delay is reported to promote reentry-based arrhythmias.[8] Since similar inducibility and duration of AF/AFL were observed in the sham and AVS atria in the absence of carbachol (Fig. 5, control), the antiarrhythmic property by the prolonged effective refractory period was likely to

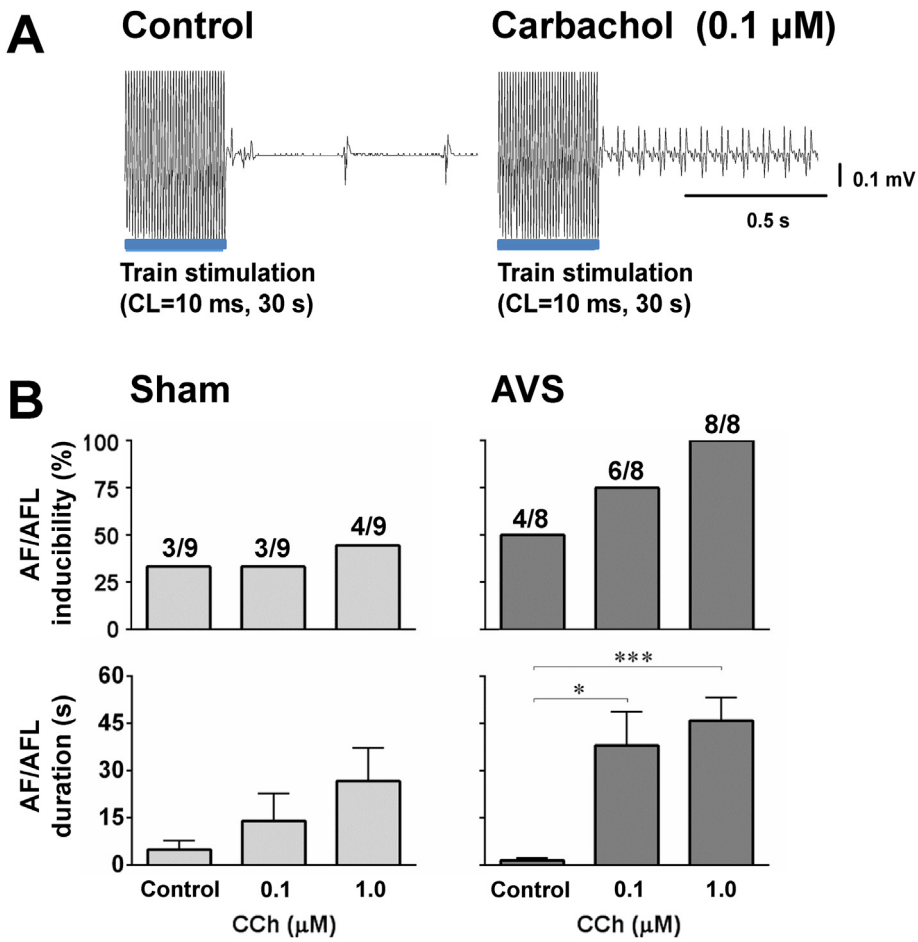

Fig. 5. Effects of carbachol on the burst pacing-induced AF/AFL. (A) Typical examples of electrograms after burst pacing (cycle length of 10 ms for 30 s) in the AVS atrium. Three beats of premature atrial contractions were triggered by the burst pacing before carbachol treatment (Control: upper left panel). A sustained episode of AFL was triggered by the burst pacing after 0.1 μM of carbachol application (Carbachol: upper right panel). (B) Inducibility and duration of AF/AFL by the burst pacing in the sham ($n = 9$) and AVS ($n = 8$) atria (lower panel) after carbachol (CCh: 0.1 and 1 μM) application. Data of AF/AFL duration are presented as mean ± S.E.M. $^{*}P < 0.05$, $^{***}P < 0.001$. AF: atrial fibrillation, AFL: atrial flutter, AVS: aorto-venocaval shunt.

counteract the proarrhythmic potential associated with arrhythmogenic substrates including reduced conduction velocity and interstitial fibrosis, as well as atrial enlargement.

4.2. Comparison of the effect of carbachol on the sham and AVS remodeled atria

Carbachol shortened the atrial effective refractory period in both sham-operated and AVS rats in a concentration-related manner, as shown in Fig. 3. Since abbreviation of the atrial effective refractory period is suggested to promote reentry-based arrhythmias,[2–4] the result may reflect the increment of AF/AFL duration in the presence of carbachol, as shown in Fig. 5. More interestingly, the extent of the changes by carbachol at the high concentration was greater in the atria of the AVS rat, suggesting that the cholinergic receptor stimulation completely counteracts component of the AVS-induced prolongation of the atrial effective refractory period through activation of I_{KACh}. Similar electrophysiological responses to carbachol have been reported in the isolated pulmonary vein myocardium.[8] Since the observation may be important to better understand pathophysiology of AF associated with activation of parasympathetic nerves, further investigation will be awaited for determining relationship between progress of atrial remodeling and proarrhythmic properties.

In this study, carbachol increased the inter-atria conduction velocity in a concentration-related manner both in the sham-operated and AVS atria, which was relatively greater in the atria of the AVS rat, as shown in Fig. 4. Our previous study has demonstrated that the resting membrane potential in the pulmonary vein myocardium of the AVS rat was less negative than that of the sham-operated rat and that carbachol more potently hyperpolarized the resting membrane potential in that of the AVS rat.[8] Thus, the similar mechanism[15] might exist in the atria of the AVS rat, leading to the recovery of sodium channels becoming increasingly rapid. Importantly, the accelerated conduction velocity is considered as antiarrhythmic, which may partly counteract proarrhythmic actions by carbachol, associated with the greater abbreviation of atrial effective refractory period, in the AVS rat.

Although we confirmed that the atrial electrophysiological responses to carbachol were mediated by muscarinic receptors using atropine, putative mechanisms underlying the differences of responsiveness to carbachol between sham and AVS models are still unclear. Previous cellular electrophysiological studies have revealed that I_{KACh} can be enhanced by increases in protein kinase C protein expression, intracellular Na^+ concentration and 1,2-diacylglycerol as well as acidosis,[17–20] whereas myocardial acute stretch by volume overload may reduce I_{KACh} activity,[21] as summarized in Fig. 6. It has been shown that constitutively active I_{KACh} is enhanced in the atrial myocytes from patients with chronic AF, whereas carbachol-activated I_{KACh} in such patients is less than that in patients with sinus rhythm.[16] In addition, activity of I_{KACh} has been shown to be altered by amplitude of inward rectifier K^+ current I_{K1}.[7]

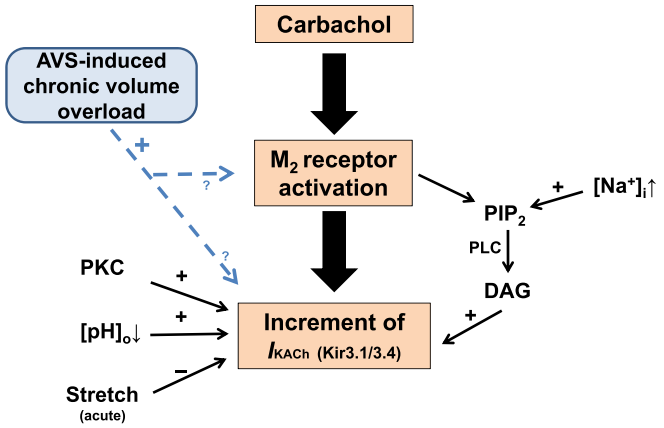

Fig. 6. Schematic summary figure of our experiments. Previous cellular electrophysiological studies have revealed that I_{KACh} can be enhanced by increases in PKC protein expression, intracellular Na^+ concentration and DAG as well as acidosis,[16–19] whereas myocardial acute stretch by volume overload may reduce I_{KACh} activity.[20] The present study may suggest possibility that chronic volume overload to the heart may alter intracellular signal transduction associated with electrophysiological responses to carbachol, leading to enhanced vulnerability to atrial fibrillation. PIP_2: phosphatidylinositol 4,5-bisphosphate; PKC: protein kinase C; DAG: 1,2-diacylglycerol; PLC: phospholipase C; AVS: aorto-venocaval shunt.

Based on these investigations, further experiments dealing with molecular control mechanisms of I_{KACh} are needed to elucidate proarrhythmic mechanisms existing in the atria of AVS rats.

5. Conclusion

In conclusion, the present study showed that chronic volume overload-induced atrial remodeling promoted electrophysiological responses to cholinergic receptor stimulation in the isolated atria of rats, suggesting possible synergistic actions between structural arrhythmogenic substrate in the remodeled atria and functional arrhythmogenic substrates modulated by parasympathetic nerve activity. The observation may be important to better understand pathophysiology of AF associated with activation of parasympathetic nerves.

Conflict of interest statement

The authors declare no conflicts of interest.

Acknowledgments

This study was supported in part by JSPS KAKENHI (#15K08598).

References

1. Skielboe AK, Bandholm TQ, Hakmann S, Mourier M, Kallemose T, Dixen U. Cardiovascular exercise and burden of arrhythmia in patients with atrial fibrillation – a randomized controlled trial. *PLoS One*. 2017;12, e0170060. https://doi.org/10.1371/journal.pone.0170060. eCollection 2017.
2. Chen PS, Tan AY. Autonomic nerve activity and atrial fibrillation. *Heart Rhythm*. 2007;4:S61–S64.
3. Schauerte P, Scherlag BJ, Pitha J, et al. Catheter ablation of cardiac autonomic nerves for prevention of vagal atrial fibrillation. *Circulation*. 2000;102:2774–2780.
4. Liu L, Nattel S. Differing sympathetic and vagal effects on atrial fibrillation in dogs: role of refractoriness heterogeneity. *Am J Physiol*. 1997;273:H805–H816.
5. Deroubaix E, Folliguet T, Rücker-Martin C, et al. Moderate and chronic hemodynamic overload of sheep atria induces reversible cellular electrophysiologic abnormalities and atrial vulnerability. *J Am Coll Cardiol*. 2004;44:1918–1926.
6. Chen PS, Chen LS, Fishbein MC, Lin SF, Nattel S. Role of the autonomic nervous system in atrial fibrillation: pathophysiology and therapy. *Circ Res*. 2014;114:1500–1515.
7. Nattel S, Heijman J, Voigt N, Wehrens XHT, Dobrev D. The molecular pathophysiology of atrial fibrillation. In: Zipes D, Jalife J, Stevenson W, eds. *Cardiac Electrophysiology: From Cell to Bedside*. 7th ed. Philadelphia, PA: Elsevier; 2017:396–408.
8. Hamaguchi S, Tsuneoka Y, Tanaka A, et al. Manifestation of automaticity in the pulmonary-vein myocardium of rats with abdominal aorto-venocaval shunt. *J Pharmacol Sci*. 2015;128:212–215.
9. Garcia R, Diebold S. Simple, rapid, and effective method of producing aorto-caval shunts in the rat. *Cardiovasc Res*. 1990;24:430–432.
10. Takahara A, Takeda K, Tsuneoka Y, Hagiwara M, Namekata I, Tanaka H. Electrophysiological effects of the class Ic antiarrhythmic drug pilsicainide on the guinea-pig pulmonary vein myocardium. *J Pharmacol Sci*. 2012;118:506–511.
11. Takahara A, Takeda K, Hagiwara M, Tanaka H. Electrophysiological effects of the antiarrhythmic drug bepridil on the guinea-pig pulmonary vein myocardium. *Biol Pharm Bull*. 2013;36:311–315.
12. Iizuka H. Cardiac effects of acetylcholine and its congeners. *Nihon Yakurigaku Zasshi*. 1983;81:441–449.
13. Li D, Melnyk P, Feng J, et al. Effects of experimental heart failure on atrial cellular and ionic electrophysiology. *Circulation*. 2000;101:2631–2638.
14. Li D, Fareh S, Leung TK, Nattel S. Promotion of atrial fibrillation by heart failure in dogs: atrial remodeling of a different sort. *Circulation*. 1999;100:87–95.
15. Hasuo H, Koketsu K, Minota S. Indirect effects of acetylcholine on the electrogenic sodium pump in bull-frog atrial muscle fibres. *J Physiol*. 1988;399:519–535.
16. Dobrev D, Friedrich A, Voigt N, et al. The G protein-gated potassium current $I_{K,ACh}$ is constitutively active in patients with chronic atrial fibrillation. *Circulation*. 2005;112:3697–3706.
17. Dent MR, Dhalla NS, Tappia PS. Phospholipase C gene expression, protein content, and activities in cardiac hypertrophy and heart failure due to volume overload. *Am J Physiol Heart Circ Physiol*. 2004;287:H719–H727.
18. Makary S, Voigt N, Maguy A, et al. Differential protein kinase C isoform regulation and increased constitutive activity of acetylcholine-regulated potassium channels in atrial remodeling. *Circ Res*. 2011;109:1031–1043.
19. Voigt N, Friedrich A, Bock M, et al. Differential phosphorylation-dependent regulation of constitutively active and muscarinic receptor-activated $I_{K,ACh}$ channels in patients with chronic atrial fibrillation. *Cardiovasc Res*. 2007;74:426–437.
20. Stevens EB, Shah BS, Pinnock RD, Lee K. Bombesin receptors inhibit G protein-coupled inwardly rectifying K^+ channels expressed in Xenopus oocytes through a protein kinase C-dependent pathway. *Mol Pharmacol*. 1999;55:1020–1027.
21. Hibino H, Inanobe A, Furutani K, Murakami S, Findlay I, Kurachi Y. Inwardly rectifying potassium channels: their structure, function, and physiological roles. *Physiol Rev*. 2010;90:291–366.

Journal of Pharmacological Sciences 136 (2018) 79–85

Contents lists available at ScienceDirect

Journal of Pharmacological Sciences

journal homepage: www.elsevier.com/locate/jphs

Full paper

The activity of organic anion transporter-3: Role of dexamethasone

Haoxun Wang, Chenchang Liu, Guofeng You*

Department of Pharmaceutics, Rutgers, The State University of New Jersey, Piscataway, NJ 08854, USA

ARTICLE INFO

Article history:
Received 30 October 2017
Received in revised form
18 December 2017
Accepted 28 December 2017
Available online 2 February 2018

Keywords:
Organic anion transporter
Drug transport
Regulation
Dexamethasone
Serum and glucocorticoid-inducible kinase

ABSTRACT

Human organic anion transporter-3 (hOAT3) is richly expressed in the kidney, where it plays critical roles in the secretion, from the blood to urine, of clinically important drugs, such as anti-viral therapeutics, anti-cancer drugs, antibiotics, antihypertensives, and anti-inflammatories. In the current study, we examined the role of dexamethasone in hOAT3 transport activity in the kidney HEK293 cells. Cis-inhibition study showed that dexamethasone exhibited a concentration-dependent inhibition of hOAT3-mediated uptake of estrone sulfate, a prototypical substrate for the transporter, with IC_{50} value of 49.91 μM. Dixon plot analysis revealed that inhibition by dexamethasone was competitive with a Ki = 47.08 μM. In contrast to the cis-inhibition effect of dexamethasone, prolonged incubation (6 h) of hOAT3-expressing cells with dexamethasone resulted in an upregulation of hOAT3 expression and transport activity, kinetically revealed as an increase in the maximum transport velocity V_{max} without meaningful alteration in substrate-binding affinity K_m. Such upregulation was abrogated by GSK650394, a specific inhibitor for serum- and glucocorticoid-inducible kinases (sgk). Dexamethasone also enhanced sgk1 phosphorylation. Our study demonstrated that dexamethasone exhibits dual effects on hOAT3: it is a competitive inhibitor for hOAT3-mediated transport, and interestingly, when entering the cells, it stimulates hOAT3 expression and transport activity through sgk1.

© 2018 The Authors. Production and hosting by Elsevier B.V. on behalf of Japanese Pharmacological Society. This is an open access article under the CC BY-NC-ND license (http://creativecommons.org/licenses/by-nc-nd/4.0/).

1. Introduction

Organic anion transporter-3 (OAT3) belongs to a class of organic anion transporters (OATs) consisting of over 10 membrane proteins. OAT3 is expressed at the basolateral membrane of the renal proximal tubule cells and plays a critical role in the secretion of many clinical drugs, including anti-HIV therapeutics, anti-tumor drugs, antibiotics, antihypertension drugs, and anti-inflammatories.[1–6]

We previously established that OATs are subjected to the regulation by the serum- and glucocorticoid-inducible kinases (sgk).[7–9] Sgk consists of three serine/threonine kinase isoforms sgk1, sgk2 and sgk3. These kinases regulate many cellular processes such as Na^+ balance, osmoregulation, cell survival, and proliferation.[10–16] They also play important roles in oncology, diabetes, and obesity.[17] Sgk1 and sgk3 are expressed ubiquitously, whereas sgk2 is restricted to tissues such as liver, kidney, pancreas, and brain. We previously demonstrated that sgk1 and sgk2 stimulate OAT activity by weakening the association of OAT with a ubiquitin ligase Nedd4-2, which leads to a deceleration of ubiquitin-dependent OAT internalization from the plasma membrane to intracellular compartments. As a result, the amount of OAT at the cell surface is enhanced and OAT transport activity is increased.[7,8]

Glucocorticoids are hormones that regulate numerous physiological activities related with metabolic, cardiovascular, and inflammatory processes.[18] Excess of glucocorticoids contribute to obesity, hyperlipidemia, hypertension, and glucose intolerance.[19] Glucocorticoids have been used for the treatment of diarrhea related to inflammatory bowel diseases and nontropical sprue.[20] Several studies have shown that one of the signaling molecule downstream glucocorticoids is sgk.[21–23] In the current study, we investigated the role of dexamethasone, a synthetic glucocorticoid, in OAT3 expression and transport activity.

2. Materials and methods

2.1. Materials

The HEK293 cells were purchased from ATCC (Manassas, VA). [^{3}H]-labeled estrone sulfate ([^{3}H]-ES) was purchased from

* Corresponding author. Department of Pharmaceutics, Rutgers, The State University of New Jersey, 160 Frelinghuysen Road, Piscataway, NJ 08854, USA.
E-mail address: gyou@pharmacy.rutgers.edu (G. You).
Peer review under responsibility of Japanese Pharmacological Society.

https://doi.org/10.1016/j.jphs.2017.12.011
1347-8613/© 2018 The Authors. Production and hosting by Elsevier B.V. on behalf of Japanese Pharmacological Society. This is an open access article under the CC BY-NC-ND license (http://creativecommons.org/licenses/by-nc-nd/4.0/).

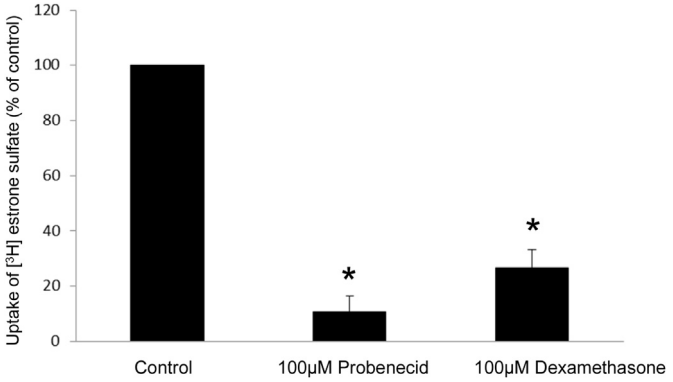

Fig. 1. Cis-inhibition of hOAT3-mediated [^{3}H]-ES uptake by dexamethasone. 4-min uptake of 300 nM [^{3}H]-ES in the presence of dexamethasone (100 μM) or probenecid (100 μM) was measured. Each data point represented only carrier-mediated transport after subtraction of values from parental cells. Uptake activity was expressed as percentage of uptake measured in control cells from three independent experiments. Results shown are means ± S.E. of three separate experiments. *P < 0.05.

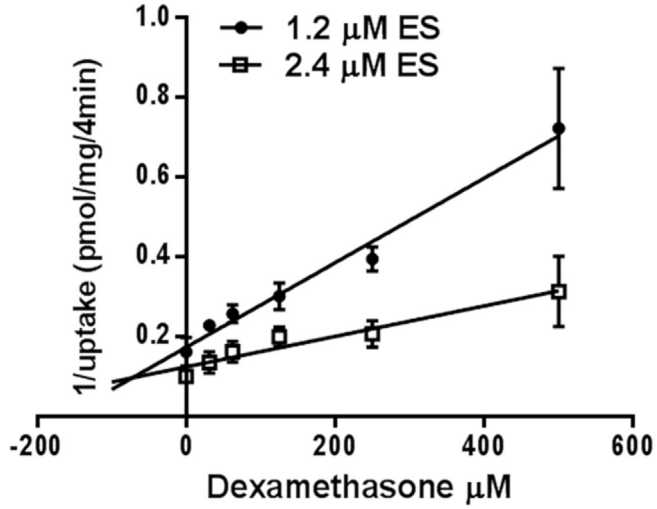

Fig. 3. Dixon plot analysis of the inhibitory effects of dexamethasone on hOAT3-mediated transport. [^{3}H]-ES uptake (1.2 μM and 2.4 μM) was determined at 4 min in the presence of varying concentrations of dexamethasone. Each data point represented only carrier-mediated transport after subtraction of values from parental cells. Results shown are means ± SE percentage of uptake measured in control cells. The data were fitted by linear regression and K_i was calculated.

PerkinElmer (Waltham, MA). cDNA for mouse Flag-tagged sgk1 was generously provided by Dr. Alan C. Pao from the Department of Medicine, Stanford University, (Stanford, CA). Dexamethasone and all other reagents were purchased from Sigma–Aldrich (St Louis, MO).

2.2. Cell culture and transient transfection

Parental HEK293 cells were grown in Dulbecco's modified Eagle's medium (DMEM) (Corning, Corning, NY) supplemented with 10% fetal bovine serum (Gibco, Grand Island, NY) at 37 °C in 5% CO_2. Lipofectamine 2000 (Invitrogen, Carlsbad, CA) was used for transfection of cDNAs following the manufacturer's instructions. 48 h after transfection, the cells were used for further experiments. Cells stably expressing hOAT3 were maintained in DMEM medium supplemented with 0.2 mg/ml G418 (Invitrogen, Carlsbad, CA), and 10% fetal bovine serum.

2.3. Transport measurement

The transport activity of hOAT3 was determined by measuring [^{3}H]-ES uptake into hOAT3-expressing cells. The uptake solution consists of phosphate-buffered saline (PBS) with 1 mM $CaCl_2$ and 1 mM $MgCl_2$ (PBS/CM) (137 mM NaCl, 2.7 mM KCl, 4.3 mM Na_2HPO_4, 1.4 mM KH_2PO_4, 0.1 mM $CaCl_2$ and 1 mM $MgCl_2$, pH 7.4) and [^{3}H]-ES (300 nM). At the time points indicated, uptake was terminated by removing the uptake solution followed by washing with ice-cold PBS twice. The cells were then lysed in 0.2 N NaOH, neutralized with 0.2 N HCl and transferred into scintillation vials for liquid scintillation counting.

2.4. Cell surface biotinylation

The expression level of hOAT3 at the cell surface was examined by using a biotinylation strategy. The cells in monolayer culture were washed with ice-cold PBS and then incubated with 1 ml of NHS-SS-biotin (0.5 mg/ml in PBS/CM) on ice for two consecutive 20 min periods under gentle shaking. Biotinylation was stopped by rinsing with 100 mM glycine in PBS/CM. Afterwards, the cell extracts were prepared in lysis buffer (10 mM Tris/HCl, 150 mM NaCl, 1 mM EDTA, 0.1% SDS, 1% Triton X-100 with 1/100 protease inhibitor cocktail) for 30 min at 4 °C and cleared by centrifugation at 16,000×*g* at 4 °C. The supernatant was mixed with streptavidin-agarose beads (Pierce, Rockford, IL) to isolate cell surface proteins. Membrane-expressed hOAT3 was detected by SDS-PAGE and

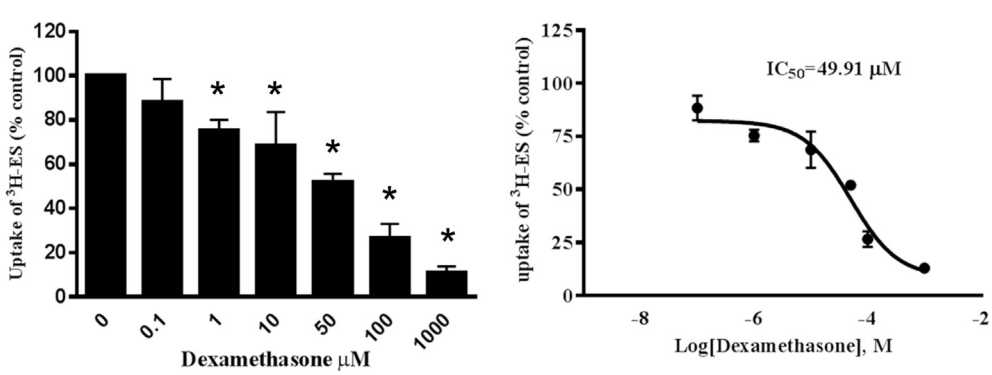

Fig. 2. Concentration dependence of dexamethasone inhibition on hOAT3-mediated uptake. hOAT3-expressing cells were incubated for 4 min with 300 nM [^{3}H]-ES in the presence of various concentrations of dexamethasone. Each data point represented only carrier-mediated transport after subtraction of values from parental cells. Uptake activity was expressed as percentage of uptake measured in control cells from three independent experiments. Results shown are means ± S.E. of three separate experiments. *P < 0.05. The line represents a best fit of data using nonlinear regression analysis.

immunoblotting with an anti-myc antibody (epitope myc was tagged to hOAT3).

2.5. Electrophoresis and immunoblotting

The protein samples were separated on 7.5% SDS-PAGE minigels (Bio-Rad, Hercules, CA) and electroblotted on to polyvinylidene difluoride (PVDF) membranes (Bio-Rad, Hercules, CA). The blots were blocked with 5% nonfat dry milk for 1–2 h in PBS-Tween 20 (PBST; 0.05% Tween-20 in PBS) at room temperature, washed and incubated overnight at 4 °C with appropriate primary antibodies. The primary antibodies included mouse anti-E cadherin (Abcam, Cambridge, MA), rabbit anti-sgk1 (Cell Signaling, Danvers, MA), mouse anti-myc (Roche, Indianapolis, IN), mouse anti-β-actin, and mouse anti-P-sgk1 (S422) (Santa Cruz, Santa Cruz, CA). The blots were then incubated with horseradish peroxidase-conjugated secondary antibodies, followed by detection with a SuperSignal West Dura Extended Duration Substrate kit (Pierce, Rockford, IL). The FluorChem 8000 imaging system (Alpha Innotech Corp., San Leandro, CA) was applied to quantify the nonsaturating, immunoreactive protein bands.

2.6. Concentration-dependent inhibition studies

Inhibition studies were performed at varying concentrations of Dexamethasone. hOAT3 specific uptake was obtained by subtracting [^{3}H]-ES uptake into parental cells from the uptake into hOAT3-expressing cells. The IC_{50} (concentration of the drugs required to inhibit 50% of ES uptake) was determined by nonlinear regression using GraphPad Prism.

2.7. Dixon plot

The mechanism of inhibition was determined by linear regression analysis of reciprocal saturable uptake (1/v) for different substrate concentrations (1.2 μM or 2.4 μM ES) as a function of inhibitor concentration. hOAT3 uptake was determined at 4 min in both the absence and presence of varying concentrations of dexamethasone. The specific uptake was obtained by subtracting [^{3}H]-ES uptake into parental cells from the uptake into hOAT3-expressing cells. The data were analyzed by linear regression with GraphPad Prism. Inhibition constant Ki was obtained by fitting the data with Eq. (1),[24–26] where C is the concentration of substrates (μM) and K_m is the Michaelis constant (μM). An IC_{50} is a relative value, which depends on the concentrations of the transporter, substrate and inhibitor with other experimental conditions used in the assay, while K_i is an intrinsic, thermo-dynamic quantity that is independent of the substrate but depends on the transporter and inhibitor. For

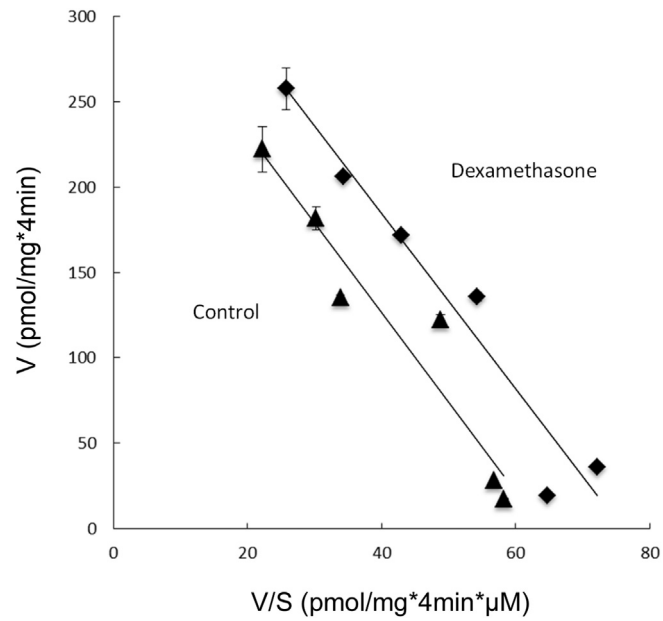

Fig. 5. Kinetic analysis of hOAT3-mediated ES transport. Kinetic characteristics were determined at substrate concentration ranging from 0.05 to 10 μM (ES, 4-min uptake) after pretreatment of dexamethasone for 6 h (10 nM). The data represent uptake into hOAT3-expressing cells minus uptake into control cells (parental cells). Values are mean ± S.E. ($n = 3$). Transport kinetic values were calculated using the Eadie–Hofstee transformation.

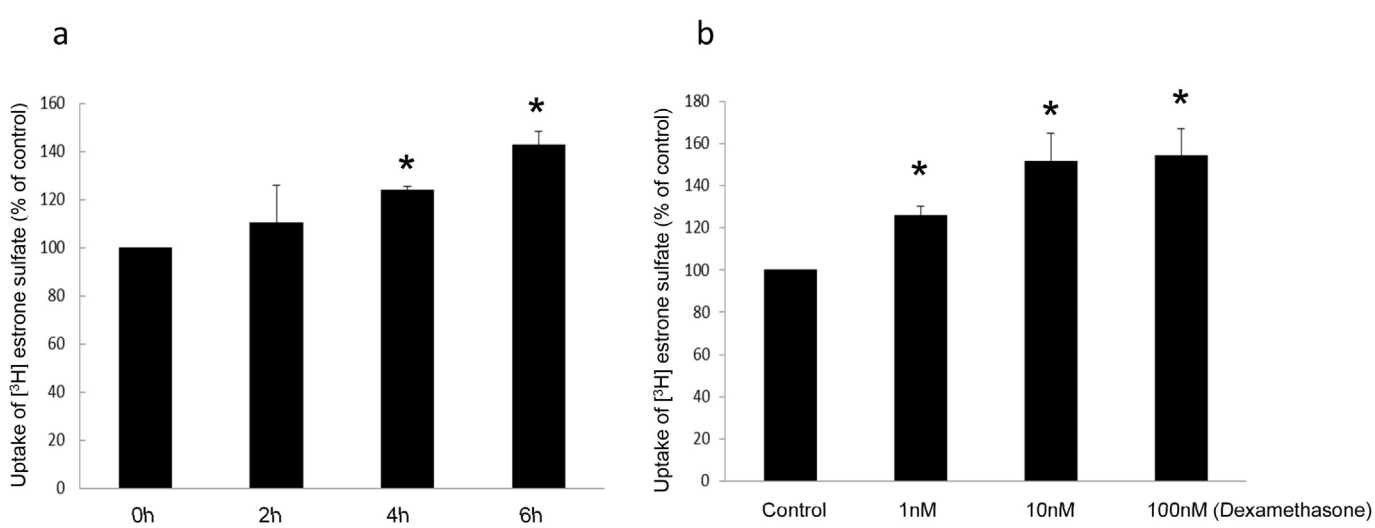

Fig. 4. Long-term treatment of hOAT3-expressing cells with dexamethasone stimulates hOAT3 transport activity. (a). Time dependence. hOAT3-expressing cells were pretreated with dexamethasone (10 nM) for 2, 4 and 6 h. 4-min uptake of [^{3}H]-ES (300 nM) was then measured. Uptake activity was expressed as a percentage of the uptake measured in control cells. The data represent uptake into hOAT3-expressing cells minus uptake into mock cells (parental cells). Values are mean ± S.E. (n = 3). *P < 0.05. (b). Dose dependence. hOAT3-expressing cells were pretreated for 6 h with dexamethasone at varies doses. 4-min uptake of [^{3}H]-ES (300 nM) was then measured. Uptake activity was expressed as a percentage of the uptake measured in control cells. The data represent uptake into hOAT3-expressing cells minus uptake into control cells (parental cells). Values are mean ± S.E. (n = 3). *P < 0.05.

competitive inhibitors, the relationship between IC_{50} and K_i is stated in equation below.

$$K_i = \frac{IC_{50}}{1 + C/K_m} \quad (1)$$

2.8. Data analysis

Each experiment was repeated at least three times. Student's paired t-tests were used to perform statistical analysis. A value of $P < 0.05$ was considered significant.

3. Results

3.1. Cis-inhibition of hOAT3-mediated estrone sulfate (ES) uptake by dexamethasone

Cis-inhibition studies were performed in hOAT3-expressing HEK293 cells. The 4-min uptake of [^{3}H]-ES (300 nM) in the presence of dexamethasone (100 μM) or probenecid (100 μM) were measured. Probenecid is a known competitive inhibitor for OATs. As shown in Fig. 1, dexamethasone exhibited ~80% inhibition of ES uptake, similar to the inhibitory potency of probenecid.

3.2. Dose-dependent effects of dexamethasone on hOAT3-mediated transport

Dose response curve was then constructed to evaluate the effectiveness of dexamethasone as an inhibitor of hOAT3 uptake. 4-min uptake of [^{3}H]-ES (300 nM) was measured in the presence of 0.1–1000 μM dexamethasone. Our result showed that dexamethasone inhibited hOAT3-mediated ES uptake in a concentration-dependent manner with IC_{50} values of 49.91 μM (Fig. 2). IC_{50} value is the concentrations at which 50% inhibition is achieved.

3.3. Dixon plot analysis

To further characterize the mechanism of inhibition and to determine the K_i values (inhibition constant), uptake in the presence and absence of dexamethasone was analyzed via Dixon plot (Fig. 3). Dexamethasone demonstrated a competitive mechanism of

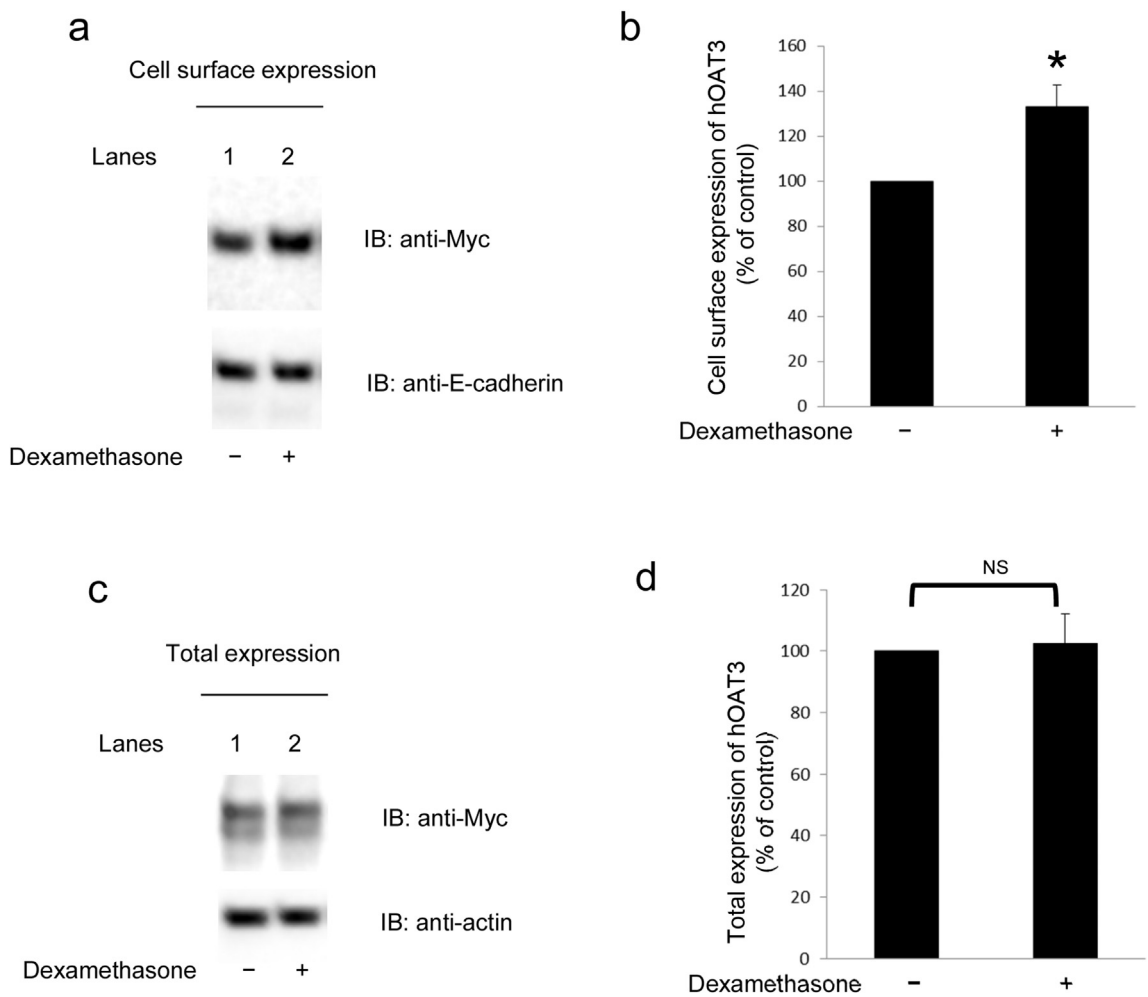

Fig. 6. Effect of dexamethasone on hOAT3 expression. (a). *Top panel:* Cell surface expression of hOAT3. hOAT3-expressing cells were pretreated with the dexamethasone (10 nM, 6 h). Cells were labeled with biotin. Biotinylated cell surface proteins were separated with streptavidin beads, followed by immunoblotting (IB) with an anti-myc antibody (hOAT3 was tagged with epitope myc for immunodetection). *Bottom panel:* The expression of cell surface protein marker E-cadherin. The same blot from the top panel was re-probed with anti- E-cadherin antibody. (b). Densitometry plot of results from Fig. 6a, top panel as well as from other experiments. The values are mean ± S.E. (n = 3). *P < 0.05. (c). *Top panel:* Total cell expression of hOAT3. hOAT3-expressing cells were pretreated with the Dexamethasone (10 nM, 6 h). Cells were lysed, followed by immunoblotting (IB) with an anti-myc antibody. *Bottom panel:* Total cell expression of cellular protein marker β-actin. The same blot from top panel was re-probed with anti-β-actin antibody. (d). Densitometry plot of results from Fig. 6c, top panel as well as from other experiments. The values are mean ± S.E. (n = 3). *P < 0.05.

inhibition of [^{3}H]-ES uptake by hOAT3 (as the lines for substrate concentrations converge above the x axis). We then determined the inhibition constant K_i by fitting the data to a competitive inhibition model, as described by Eq. (1). The K_m values of OAT3 for ES was 5 μM, the inhibition constant (K_i) of dexamethasone was then estimated as 47.08 μM.

3.4. Long-term treatment of hOAT3-expressing cells with dexamethasone stimulates hOAT3 transport activity

The above studies (Figs. 1–3) were designed by measuring the 4-min uptake of [^{3}H]-ES (300 nM) in the presence of dexamethasone (100 μM). However, the long-term effect of dexamethasone on hOAT3 is not known. In the current experiment, we pretreated hOAT3-expressing cells with dexamethasone for 0–6 h, followed by measuring [^{3}H]-ES uptake. Our results showed that long-term treatment of hOAT3-expressing cells with dexamethasone resulted in a stimulation of hOAT3-mediated [^{3}H]-ES uptake with 40% stimulation after 6 h pretreatment (Fig. 4a). Dexamethasone also induced a dose-dependent stimulation of hOAT3 mediated transport with 6 h pretreatment (Fig. 4b). To examine the mechanism of dexamethasone-induced stimulation of hOAT3 activity, we determined hOAT3-mediated [^{3}H]-ES uptake at different substrate (ES) concentrations. An Eadie-Hofstee analysis of the derived data (Fig. 5) showed that treatment of hOAT3-expressing cells with dexamethasone resulted in an increased maximal transport velocity V_{max} of hOAT3 (330 ± 24 pmol $mg^{-1}\cdot 4\ min^{-1}$ with control cells and 387 ± 29 pmol $mg^{-1}\cdot 4\ min^{-1}$ with cells transfected with dexamethasone) with no significant change in the substrate-binding affinity K_m of the transporter (5.07 ± 0.49 μM with control cells and 5.08 ± 0.51 μM with cells transfected with dexamethasone).

3.5. Effect of dexamethasone on hOAT3 expression

An increased Vmax (Fig. 5) could be a result from either an increased number of the transporter at the cell surface or an increased transporter turnover number. We conducted experiments that differentiate between these possibilities by measuring transporter expression both at the cell surface and in the total cell lysates. We showed that dexamethasone treatment resulted in an increased cell surface expression of hOAT3 without affecting the total cell expression of the transporter (Fig. 6).

3.6. Sgk inhibitor GSK650394 abrogates the stimulatory effect of dexamethasone on hOAT3 transport activity

Several studies have shown that one of the signaling molecule downstream glucocorticoids is the serum- and glucocorticoid-inducible kinases (sgk). In this experiment, we examined whether sgk mediates the effect of dexamethasone on hOAT3. We treated hOAT3-expressing cells with dexamethasone with or without a sgk-selective inhibitor GSK650394, followed by the measurement of hOAT3-mediated uptake of [^{3}H]-ES. As shown in Fig. 7, dexamethasone stimulated hOAT3-mediated transport ~40% in control cells, whereas such stimulation was blocked in the presence of GSK650394.

3.7. Dexamethasone enhanced sgk1 phosphorylation

Previous investigations[23,27,28] reported that activation of sgk1 is dependent upon the phosphorylation of this kinase, at least in part, by phosphorylating sgk1 at serine residue 422 (Ser 422). Thus, we examined the effect of dexamethasone on the phosphorylation levels of sgk1. hOAT3-expressing cells were pretreated with dexamethasone for 6 h (10 nM). Treated cells were then lysed, followed by immunoblotting (IB) with anti-phospho-sgk1-specific antibody. Our results showed that dexamethasone significantly enhanced the level of sgk1 phosphorylation as compared to that of the control (Fig. 8a) without change in the total expression of sgk1 (Fig. 8c). The expression level of cellular protein marker β-actin was also not changed.

4. Discussion

Organic anion transporters (OATs) are critical players in the therapeutic efficacy and toxicity of many drugs. Therefore, uncovering how OATs are regulated at the molecular and cellular levels is clinically and pharmacologically significant. The current investigation revealed that dexamethasone, a synthetic glucocorticoid, has a significant role in modulating hOAT3 expression and transport activity.

Glucocorticoids are known to affect a variety of renal functions. Glucocorticoid excess can lead to metabolic alkalosis and potassium depletion.[29] In addition, glucocorticoids such as dexamethasone have been shown to specifically regulate, through glucocorticoid receptors, a set of transporters/exchangers (e.g. Na^+:HCO_3^- cotransporter, Na^+/H^+ exchanger) in renal proximal tubules, where OATs are expressed.[22,30,31]

We chose to perform our investigation in human kidney HEK293 cells, a widely-used cell model for answering mechanistic questions of many renal transport processes.[32–35] Therefore, our studies in these cells will provide insights into the future investigation in evaluating whether similar regulation is working *in vivo*.

From our investigation, we gained several pieces of valuable information. Dexamethasone has dual effects on hOAT3 transport activity. First, when co-present with hOAT3 substrate for a brief period of time (4 min), dexamethasone acts as an inhibitor for hOAT3-mediated transport (Fig. 1). Further characterization of the inhibition mechanism by Dixon plot revealed that the dexamethasone is a competitive inhibitor (Fig. 3). Such mode of inhibition is that the binding of the inhibitor to the active site on the transporter excludes the binding of the substrate and *vice versa*. The IC_{50} value

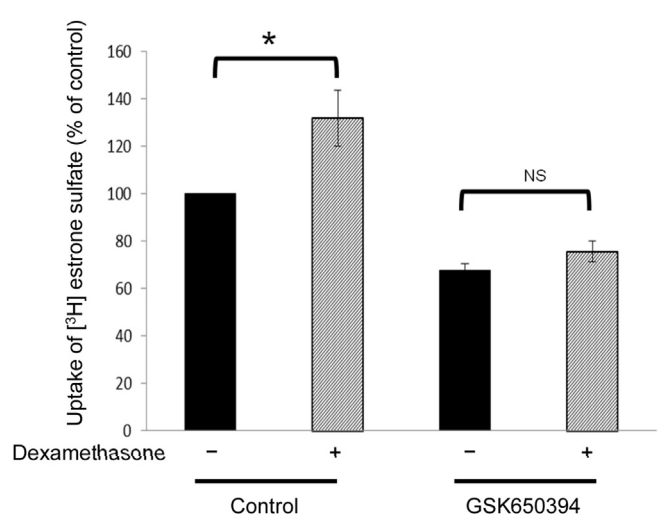

Fig. 7. Sgk inhibitor GSK650394 abrogates the stimulatory effect of dexamethasone on hOAT3 transport activity. hOAT3-expressing cells were incubated for 6 h with 10 nM dexamethasone in the presence and absence of sgk inhibitor GSK650394 (100 nM). After washing the cells, 4-min uptake of [^{3}H]-ES (300 nM) was measured. Uptake activity was expressed as a percentage of the uptake measured in control cells. The data represent uptake into hOAT3-expressing cells minus uptake into mock cells (parental HEK293 cells). The values are mean ± S.E. (n = 3). *P < 0.05.

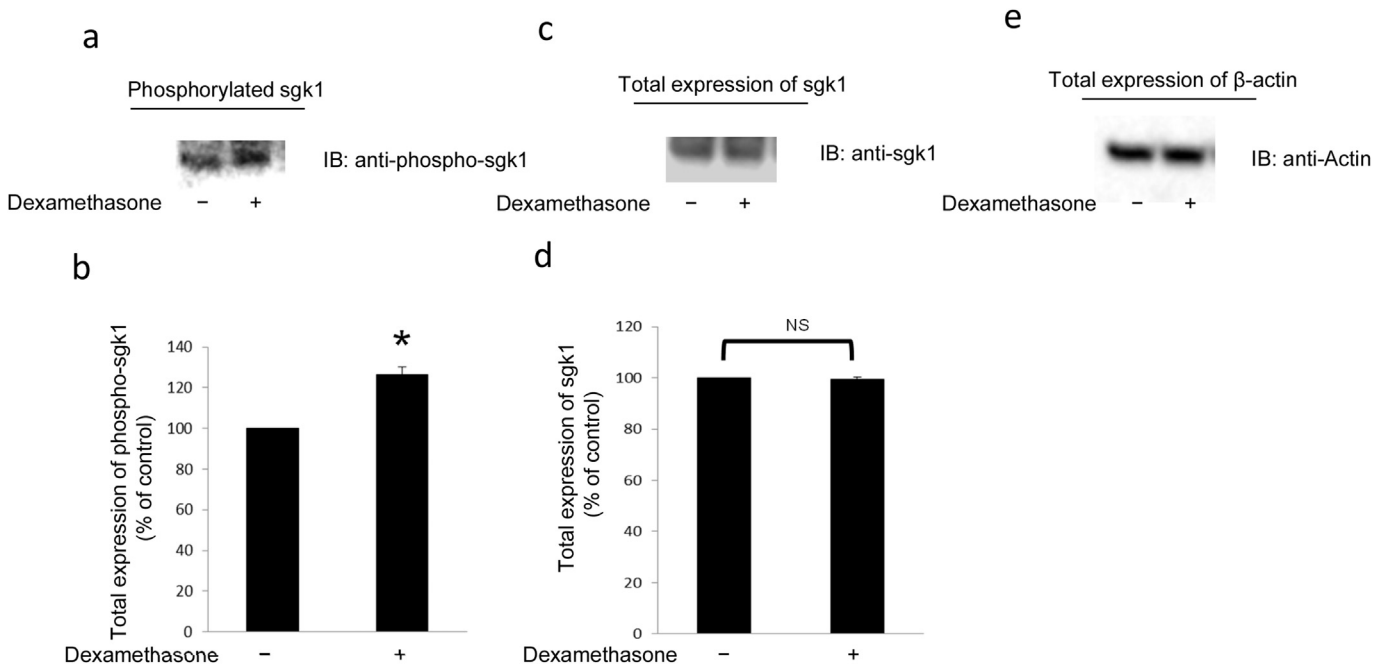

Fig. 8. Dexamethasone phosphorylates sgk1. (a) Total cell expression of phospho-sgk1. hOAT3-expressing cells were pretreated with dexamethasone (10 nM, 6 h). Cells were lysed, followed by immunoblotting (IB) with anti-phospho-sgk1(Ser422)-specific antibody. (b) Densitometry plot of results from Fig. 8a, as well as from other experiments. The values are mean ± SE (n = 3). (c) The same blot from Fig. 8a was re-probed with anti-sgk1. (d) Densitometry plot of results from Fig. 8c as well as from other experiments. The values are mean ± SE (n = 3). (e) The same blot from Fig. 8a was re-probed with anti-β-actin antibody. β-actin is a cellular protein marker.

of dexamethasone for hOAT3 determined in the present study is 49.91 μM (Fig. 2). This is the concentrations at which 50% inhibition was achieved. The maximum plasma concentration (C_{max}) of dexamethasone is 0.16 μM (64.4 μg/L), as suggested by spoorenberg et al.[36] Corrected by unbound fraction value of 0.272,[37] the unbound maximum plasma concentration ($C_{u,max}$) of dexamethasone is ~0.045 μM. A $C_{u,max}/IC_{50}$ value greater than 0.1 would indicate a potential for drug–drug interaction.[38] The $C_{u,max}/IC_{50}$ value of dexamethasone for hOAT3 was <0.1. Therefore, the propensity for dexamethasone to cause drug–drug interaction through inhibition of hOAT3 is low.

Interestingly, long-term treatment of hOAT3-expressing cells at the clinically relevant concentration of dexamethasone (10 nM), displayed an opposite effect of dexamethasone on hOAT3 transport activity. Instead of an inhibitory role, pretreatment of hOAT3-expressing cells with dexamethasone for 6 h resulted in a 40% stimulation of hOAT3 activity (Fig. 4). The stimulation of hOAT3 transport activity by dexamethasone correlated with an enhanced hOAT3 expression at the cell surface. One of the signaling pathways downstream of dexamethasone is the serum- and glucocorticoid-inducible kinases (sgk) pathway. Our lab previously demonstrated that sgk stimulates OAT expression and activity by weakening the interaction of OAT with a ubiquitin ligase Nedd4-2 and therefore preventing Nedd4-2-dependent OAT internalization from the cell surface.[7–9] To examine the role of sgk in the effect of dexamethasone on hOAT3, we pretreated hOAT3-expressing cells with dexamethasone in the presence or absence of sgk-specific inhibitor GSK650394. We showed that GSK650394 abrogated stimulatory effect of dexamethasone on hOAT3 transport activity, suggesting that dexamethasone exerts its effect on hOAT3 through the activation of sgk (Fig. 7). This conclusion was further reinforced by our results showing that dexamethasone enhanced sgk phosphorylation (Fig. 8). Phosphorylation of sgk was previously reported to be a prerequisite for the activation of this kinase.[23,28] Based on previously published work, dexamethasone diffuses passively into cells,[39] stimulates PI3K signaling pathway through binding to glucocorticoid receptor,[22] which leads to the phosphorylation of SGK1 and enhancement of SGK1 activity.

Dexamethasone is a synthetic glucocorticoid. Because of its potent anti-inflammatory and immunosuppressant effect, it has been widely used to treat inflammatory and autoimmune conditions, such as rheumatic problems, and severe allergies.[40] What is more, it is often used with chemotherapy in cancer patient to counteract certain side effects of their antitumor treatments.[41] Our *in vitro* study showed that at a clinical relevant concentration (10 nM), long-term treatment with dexamethasone stimulated hOAT3 transport activity, suggesting that hOAT3-mediated drug elimination might be affected if a hOAT3 substrate/drug is taken with dexamethasone simultaneously. The *in vivo* study aiming at identifying the effect of dexamethasone on hOAT3 activity is currently being carried out in our lab.

In summary, current study uncovered dual roles of dexamethasone in hOAT3 transport activity: dexamethasone can act as a competitive inhibitor for hOAT3-mediated transport. Interestingly, once entering the cells, dexamethasone activates sgk1, which leads to an enhanced hOAT3 expression at the cell surface and an enhanced hOAT3 transport activity.

Conflict of interest

The authors have declared that there is no conflict of interest.

Acknowledgment

This work was supported by grant (to Dr. Guofeng You) from National Institute of General Medical Sciences (R01-GM079123).

References

1. You G. Structure, function, and regulation of renal organic anion transporters. *Med Res Rev*. 2002;22:602–616.
2. Srimaroeng C, Perry JL, Pritchard JB. Physiology, structure, and regulation of the cloned organic anion transporters. *Xenobiotica*. 2008;38:889–935.

3. Dantzler WH, Wright SH. The molecular and cellular physiology of basolateral organic anion transport in mammalian renal tubules. *Biochim Biophys Acta*. 2003;1618:185–193.
4. VanWert AL, Gionfriddo MR, Sweet DH. Organic anion transporters: discovery, pharmacology, regulation and roles in pathophysiology. *Biopharm Drug Dispos*. 2010;31:1–71.
5. Ahn SY, Nigam SK. Toward a systems level understanding of organic anion and other multispecific drug transporters: a remote sensing and signaling hypothesis. *Mol Pharmacol*. 2009;76:481–490.
6. Terada T, Inui K. Gene expression and regulation of drug transporters in the intestine and kidney. *Biochem Pharmacol*. 2007;73:440–449.
7. Wang H, Xu D, Toh MF, Pao AC, You G. Serum- and glucocorticoid-inducible kinase SGK2 regulates human organic anion transporters 4 via ubiquitin ligase Nedd4-2. *Biochem Pharmacol*. 2016;102:120–129.
8. Wang H, You G. SGK1/Nedd4-2 signaling pathway regulates the activity of human organic anion transporters 3. *Biopharm Drug Dispos*. 2017;38:449–457.
9. Xu D, Huang H, Toh MF, You G. Serum- and glucocorticoid-inducible kinase sgk2 stimulates the transport activity of human organic anion transporters 1 by enhancing the stability of the transporter. *Int J Biochem Mol Biol*. 2016;7:19–26.
10. Chen SY, Bhargava A, Mastroberardino L, et al. Epithelial sodium channel regulated by aldosterone-induced protein sgk. *Proc Natl Acad Sci U S A*. 1999;96:2514–2519.
11. Naray-Fejes-Toth A, Canessa C, Cleaveland ES, Aldrich G, Fejes-Toth G. sgk is an aldosterone-induced kinase in the renal collecting duct. Effects on epithelial na+ channels. *J Biol Chem*. 1999;274:16973–16978.
12. Rozansky DJ, Wang J, Doan N, et al. Hypotonic induction of SGK1 and Na+ transport in A6 cells. *Am J Physiol Ren Physiol*. 2002;283:F105–F113.
13. Waldegger S, Barth P, Forrest Jr JN, Greger R, Lang F. Cloning of sgk serine-threonine protein kinase from shark rectal gland – a gene induced by hypertonicity and secretagogues. *Pflugers Arch*. 1998;436:575–580.
14. Leong ML, Maiyar AC, Kim B, O'Keeffe BA, Firestone GL. Expression of the serum- and glucocorticoid-inducible protein kinase, Sgk, is a cell survival response to multiple types of environmental stress stimuli in mammary epithelial cells. *J Biol Chem*. 2003;278:5871–5882.
15. Buse P, Tran SH, Luther E, Phu PT, Aponte GW, Firestone GL. Cell cycle and hormonal control of nuclear-cytoplasmic localization of the serum- and glucocorticoid-inducible protein kinase, Sgk, in mammary tumor cells. A novel convergence point of anti-proliferative and proliferative cell signaling pathways. *J Biol Chem*. 1999;274:7253–7263.
16. Pao AC, Bhargava A, Di Sole F, et al. Expression and role of serum and glucocorticoid-regulated kinase 2 in the regulation of Na^+/H^+ exchanger 3 in the mammalian kidney. *Am J Physiol Ren Physiol*. 2010;299:F1496–F1506.
17. Tessier M, Woodgett JR. Serum and glucocorticoid-regulated protein kinases: variations on a theme. *J Cell Biochem*. 2006;98:1391–1407.
18. Dallman MF, la Fleur SE, Pecoraro NC, Gomez F, Houshyar H, Akana SF. Minireview: glucocorticoids–food intake, abdominal obesity, and wealthy nations in 2004. *Endocrinology*. 2004;145:2633–2638.
19. Schacke H, Docke WD, Asadullah K. Mechanisms involved in the side effects of glucocorticoids. *Pharmacol Ther*. 2002;96:23–43.
20. Yang YX, Lichtenstein GR. Corticosteroids in Crohn's disease. *Am J Gastroenterol*. 2002;97:803–823.
21. Di Pietro N, Panel V, Hayes S, et al. Serum- and glucocorticoid-inducible kinase 1 (SGK1) regulates adipocyte differentiation via forkhead box O1. *Mol Endocrinol*. 2010;24:370–380.
22. Wang D, Zhang H, Lang F, Yun CC. Acute activation of NHE3 by dexamethasone correlates with activation of SGK1 and requires a functional glucocorticoid receptor. *Am J Physiol Cell Physiol*. 2007;292:C396–C404.
23. Miyata S, Koyama Y, Takemoto K, et al. Plasma corticosterone activates SGK1 and induces morphological changes in oligodendrocytes in corpus callosum. *PLoS One*. 2011;6:e19859.
24. Akarawut W, Smith DE. Competitive inhibition of p-aminohippurate transport by quinapril in rabbit renal basolateral membrane vesicles. *J Pharmacokinet Biopharm*. 1998;26:269–287.
25. Burlingham BT, Widlanski TS. An intuitive look at the relationship of K-i and IC50: a more general use for the Dixon plot. *J Chem Educ*. 2003;80:214–218.
26. Cer RZ, Mudunuri U, Stephens R, Lebeda FJ. IC50-to-Ki: a web-based tool for converting IC50 to Ki values for inhibitors of enzyme activity and ligand binding. *Nucleic Acids Res*. 2009;37:W441–W445.
27. Alamares-Sapuay JG, Martinez-Gil L, Stertz S, Miller MS, Shaw ML, Palese P. Serum- and glucocorticoid-regulated kinase 1 is required for nuclear export of the ribonucleoprotein of influenza A virus. *J Virol*. 2013;87:6020–6026.
28. Chen W, Chen Y, Xu BE, et al. Regulation of a third conserved phosphorylation site in SGK1. *J Biol Chem*. 2009;284:3453–3460.
29. Christy NP, Laragh JH. Pathogenesis of hypokalemic alkalosis in Cushing's syndrome. *N Engl J Med*. 1961;265:1083–1088.
30. Ali R, Amlal H, Burnham CE, Soleimani M. Glucocorticoids enhance the expression of the basolateral Na^+:HCO_3- cotransporter in renal proximal tubules. *Kidney Int*. 2000;57:1063–1071.
31. Dagan A, Gattineni J, Cook V, Baum M. Prenatal programming of rat proximal tubule Na^+/H^+ exchanger by dexamethasone. *Am J Physiol Regul Integr Comp Physiol*. 2007;292:R1230–R1235.
32. Zeng Y, Zhang R, Wu J, et al. Organic anion transporter 1 (OAT1) involved in renal cell transport of aristolochic acid I. *Hum Exp Toxicol*. 2012;31:759–770.
33. Xue X, Gong LK, Maeda K, et al. Critical role of organic anion transporters 1 and 3 in kidney accumulation and toxicity of aristolochic acid I. *Mol Pharm*. 2011;8:2183–2192.
34. Rodiger M, Zhang X, Ugele B, et al. Organic anion transporter 3 (OAT3) and renal transport of the metal chelator 2,3-dimercapto-1-propanesulfonic acid (DMPS). *Can J Physiol Pharmacol*. 2010;88:141–146.
35. El-Sheikh AA, Greupink R, Wortelboer HM, et al. Interaction of immunosuppressive drugs with human organic anion transporter (OAT) 1 and OAT3, and multidrug resistance-associated protein (MRP) 2 and MRP4. *Transl Res*. 2013;162:398–409.
36. Spoorenberg SM, Deneer VH, Grutters JC, et al. Pharmacokinetics of oral vs. intravenous dexamethasone in patients hospitalized with community-acquired pneumonia. *Br J Clin Pharmacol*. 2014;78:78–83.
37. Lanevskij K, Dapkunas J, Juska L, Japertas P, Didziapetris R. QSAR analysis of blood-brain distribution: the influence of plasma and brain tissue binding. *J Pharm Sci*. 2011;100:2147–2160.
38. International Transporter C, Giacomini KM, Huang SM, et al. Membrane transporters in drug development. *Nat Rev Drug Discov*. 2010;9:215–236.
39. Furu K, Kilvik K, Gautvik KM, Haug E. The mechanism of [3H] dexamethasone uptake into prolactin producing rat pituitary cells (GH3 cells) in culture. *J Steroid Biochem*. 1987;28:587–591.
40. Caceres-del-Carpio J, Costa RD, Haider A, Narayanan R, Kuppermann BD. Corticosteroids: triamcinolone, dexamethasone and fluocinolone. *Dev Ophthalmol*. 2016;55:221–231.
41. Franco M, William L, Poon P, Azad A. Dexamethasone for cancer-related fatigue. *J Clin Oncol*. 2014;32:608–609.

Journal of Pharmacological Sciences 136 (2018) 86–92

Contents lists available at ScienceDirect

Journal of Pharmacological Sciences

journal homepage: www.elsevier.com/locate/jphs

Full paper

Changes of electrocardiogram and hemodynamics in response to dipyridamole: In vivo comparative analyses using anesthetized beagle dogs and *microminipigs*

Kentaro Ando [a, b, 1], Akira Takahara [c, 1], Yuji Nakamura [a, 1], Takeshi Wada [a, d], Koki Chiba [b], Ai Goto [b], Nur Jaharat Lubna [b], Mihoko Hagiwara-Nagasawa [a], Hiroko Izumi-Nakaseko [a], Kiyotaka Hoshiai [a, e], Yasuki Akie [a, e], Atsuhiko T. Naito [a, b], Atsushi Sugiyama [a, b, *]

[a] *Department of Pharmacology, Faculty of Medicine, Toho University, 5-21-16 Omori-nishi, Ota-ku, Tokyo 143-8540, Japan*
[b] *Department of Pharmacology, Toho University Graduate School of Medicine, 5-21-16 Omori-nishi, Ota-ku, Tokyo 143-8540, Japan*
[c] *Department of Pharmacology and Therapeutics, Faculty of Pharmaceutical, Sciences, Toho University, 2-2-1 Miyama, Funabashi-shi, Chiba 274-8510, Japan*
[d] *Department of Cardiology, Juntendo University Urayasu Hospital, 2-1-1 Tomioka, Urayasu-shi, Chiba 279-0021, Japan*
[e] *CMIC Pharma Science Co., Ltd., Bioresearch Center, 10221 Kobuchisawa-cho, Hokuto-shi, Yamanashi 408-0044, Japan*

ARTICLE INFO

Article history:
Received 30 October 2017
Received in revised form
25 December 2017
Accepted 9 January 2018
Available online 2 February 2018

Keywords:
Dipyridamole
Collateral arteries
Coronary steal
ST-segment depression

ABSTRACT

Microminipigs are expected as a novel animal model for cardiovascular pharmacological experiments. Since inherent vulnerability of coronary circulation of *microminipigs* has not been characterized, we performed dipyridamole-stress test to both *microminipigs* and beagle dogs, and compared the results. Dipyridamole in doses of 0.056 and 0.56 mg/kg were intravenously infused over 10 min (n = 4 for each animal). Dipyridamole decreased the systolic/diastolic blood pressures and double product in dogs as well as in *microminipigs*; but it did not significantly alter the heart rate or the global balance between the myocardial oxygen demand and supply in either animal. While organic coronary arterial stenosis was not detected in either animal, dogs have well-developed epicardial intracoronary networks unlike *microminipigs*. Like in humans, dipyridamole did not affect the ST segment of *microminipigs*, whereas it substantially depressed that in dogs. The results indicate the onset of subendocardial ischemia by dipyridamole in dogs may be partly associated with their well-developed native coronary collateral channels. *Microminipigs* would be more useful to evaluate the drugs which may affect the coronary circulation in the pre-clinical study than dogs.

© 2018 The Authors. Production and hosting by Elsevier B.V. on behalf of Japanese Pharmacological Society. This is an open access article under the CC BY-NC-ND license (http://creativecommons.org/licenses/by-nc-nd/4.0/).

1. Introduction

An extraordinarily small-sized miniature pig; namely, *microminipig*, weighing approximately 7 kg at 6 months of age when they are young mature, was developed by Fuji Micra, Inc. (Shizuoka) as an alternative non-rodent experimental animal model to dogs and monkeys for life science research.[1,2] We have pharmacologically characterized this animal under the halothane anesthesia as an *in vivo* experimental model for safety pharmacology study. The extent of drug-induced cardiovascular responses was generally greater in *microminipigs* than in dogs because of its unique pharmacokinetic profile including smaller effective volume of distribution of drugs and less body fat content; greater basal sympathetic tone with less great reflex-mediated increase; and/or smaller repolarization reserve.[3–5] Importantly, we encountered some cases of *microminipigs* showing reversible ST-segment elevation/depression, occasionally resulting in the onset of lethal arrhythmias during the preparation period for the studies.[6,7] Since these phenomena were not observed in dogs under the same anesthetic condition, coronary regulation might be different between *microminipigs* and dogs.

* Corresponding author. Department of Pharmacology, Faculty of Medicine, Toho University, 5-21-16 Omori-nishi, Ota-ku, Tokyo 143-8540, Japan. Fax: +81 3 5493 5413.
E-mail address: atsushi.sugiyama@med.toho-u.ac.jp (A. Sugiyama).
Peer review under responsibility of Japanese Pharmacological Society.
[1] Equally contributed.

https://doi.org/10.1016/j.jphs.2018.01.002
1347-8613/© 2018 The Authors. Production and hosting by Elsevier B.V. on behalf of Japanese Pharmacological Society. This is an open access article under the CC BY-NC-ND license (http://creativecommons.org/licenses/by-nc-nd/4.0/).

Dipyridamole-stress test has been clinically performed for the diagnosis of patients with coronary artery disease.[8] Infusion of dipyridamole inhibits the intracellular adenosine reuptake and thereby increases the plasma concentration of adenosine. Adenosine then dilates the coronary artery of the healthy myocardium and increases the blood flow, but in turn blood flow into the diseased coronary artery becomes 'stolen', resulting in ischemia of the damaged myocardium.

Dipyridamole-stress test does not affect the ST segment in healthy subjects; however, it induces the ST-segment elevation/depression in the patients with coronary artery disease. In this study, we compared and characterized the coronary circulation between healthy *microminipigs* and dogs with the dipyridamole-stress test under electrocardiographic monitoring.

2. Materials and methods

Beagle dogs and *microminipigs* were obtained from Kitayama Labes Co., Ltd. (Nagano) and Fuji Micra, Inc. respectively. They were kept in individual cages on a 12 h light (6:00–18:00)-dark (18:00–6:00) cycle. The ventilation provided a total air exchange rate of 10–15 times per hour. The room temperature was maintained at 23 ± 2 °C, and relative humidity was 50 ± 30%. All experiments were approved by Toho University Animal Care and User Committee (14-54-151, 14-51-275) and performed in accordance with the Guidelines for the Care and Use of Laboratory Animals of Toho University.

2.1. Cardiovascular effects of dipyridamole in dogs

Experiments were performed using 2 male and 2 female beagle dogs weighing 10.7 ± 0.6 kg. The dogs were initially anesthetized with thiopental sodium (30 mg/kg, i.v.). After intubation with a cuffed endotracheal tube (Portex®; Smiths Medical, London, UK), 1.0% halothane vaporized with 100% oxygen was inhaled with a volume-limited ventilator (SN-480-3; Shinano Manufacturing Co., Ltd., Tokyo). Tidal volume and respiratory rate were set at 20 mL/kg and 15 breaths/min, respectively. Two sets of clinically available catheter sheath (FAST-CATH™ 406108; St. Jude Medical, Inc., Minnetonka, MN, USA) were used; one was placed into the right femoral artery, whereas the other was set in the right femoral vein. To prevent blood clotting, heparin calcium (100 IU/kg) was intravenously administered through a flush line of the catheter sheath placed at the right femoral vein. Blood pressure was measured at a flush line of the catheter sheath placed at the right femoral artery. The double product was calculated with the following equation: double product = systolic blood pressure × heart rate, which reflects the cardiac oxygen consumption rate.[8] The ratio of double product to diastolic blood pressure was also calculated to estimate the balance between cardiac oxygen supply and demand (demand/supply ratio = double product/diastolic blood pressure). The lead I, II and III electrocardiograms were continuously monitored, and the lead II was used for electrocardiographic analysis. Corrected QT interval (QTc) was calculated with Van de Water's formula: $QTc = QT - 0.087 \times (RR - 1000)$,[9] where a unit of the RR interval was given in ms. The ST-segment depression was measured both at 80 ms after the J point and at the bottom of T wave based on the previous report.[8,10]

2.2. Cardiovascular effects of dipyridamole in microminipigs

Experiments were performed using 4 male *microminipigs* weighing 9.2 ± 0.3 kg. They were pre-anesthetized with ketamine (16 mg/kg, i.m.) and xylazine (1.6 mg/kg, i.m.). A 24G cannula was introduced into a superficial auricular vein for anesthetic injection of 1 mg/kg of propofol. After intubation with a cuffed endotracheal tube (Portex®; Smiths Medical), 1.0% halothane vaporized with 100% oxygen was inhaled with a volume-limited ventilator (SN-480-3; Shinano Manufacturing, Co., Ltd.). Tidal volume and respiratory rate were set at 10 mL/kg and 15 breaths/min, respectively. Two sets of catheter sheath (FAST-CATH™ 406108; St. Jude Medical, Inc.) were used; one was placed into the right or left femoral artery, and the other was set in the right or left femoral vein. To prevent blood clotting, heparin calcium (100 IU/kg) was intravenously administered through a flush line of the catheter sheath placed at the femoral vein. Cardiovascular variables were analyzed in the same manner as described for dogs.

2.3. Experimental protocol

The heart rate, blood pressure and electrocardiogram were monitored with a polygraph system (RM-6000, Nihon Kohden Corporation, Tokyo) and analyzed by using a real-time fully automatic data analysis system (WinVAS3 ver 1.1R24; Physio-Tech Co., Ltd., Tokyo). Each measurement of electrocardiogram was made based upon the mean of three recordings of consecutive complexes. Since in preliminary experiments with the halothane-anesthetized beagle dogs (n = 2), infusion of dipyridamole in a dose of 0.56 mg/kg over 10 min markedly depressed the ST segment, the doses of 0.056 and 0.56 mg/kg were selected for this study.[8] After the basal assessment, dipyridamole in a dose of 0.056 mg/kg was intravenously infused over 10 min, and each variable was recorded at 10, 20 and 30 min for dogs and at 5, 10, 15, 20 and 30 min for *microminipigs* after the start of the administration. Then, dipyridamole in a dose of 0.56 mg/kg was infused over 10 min and each variable was assessed at 10, 20 and 30 min for dogs and at 5, 10, 15, 20, 30, 45 and 60 min for *microminipigs* after the start of the infusion. After the assessment of cardiovascular effects of dipyridamole was completed, their hearts were excised to macroscopically examine the morphology of coronary arteries.

2.4. Drugs

Dipyridamole (Persantin® Injection, Boehringer Ingelheim Japan Inc., Tokyo) was used, which was diluted with saline in concentrations of 0.056 and 0.56 mg/mL. The following drugs were purchased: thiopental sodium (Ravonal® for injection, Mitsubishi Tanabe Pharma Co., Osaka), halothane (Fluothane®, Takeda Pharmaceutical Company Ltd., Osaka), ketamine (Ketalar®, Daiichi Sankyo Company Ltd., Tokyo), xylazine (Seractal®, Bayer Yakuhin Ltd., Osaka), propofol (Diprivan®, AstraZeneca K.K., Osaka) and heparin calcium (Caprocin®, Sawai Pharmaceutical Co. Ltd., Osaka).

2.5. Statistical analyses

Data are expressed as the mean ± S.E.M. The statistical significances within a variable were evaluated by one-way, repeated-measures analysis of variance (ANOVA) followed by Contrasts as a post-hoc test for mean values comparison, whereas those between the groups were analyzed with an unpaired *t*-test. A P value < 0.05 was considered to be statistically significant.

3. Results

Cardiohemodynamic collapse or lethal ventricular arrhythmia was not observed during the experimental period for dogs or *microminipigs*. Organic coronary arterial stenosis was not macroscopically detected in the left anterior descending, circumflex or right coronary artery of either animal. Notably, dogs have more and larger epicardial coronary arteries along with collateral networks than *microminipigs*, as depicted in Fig. 1.

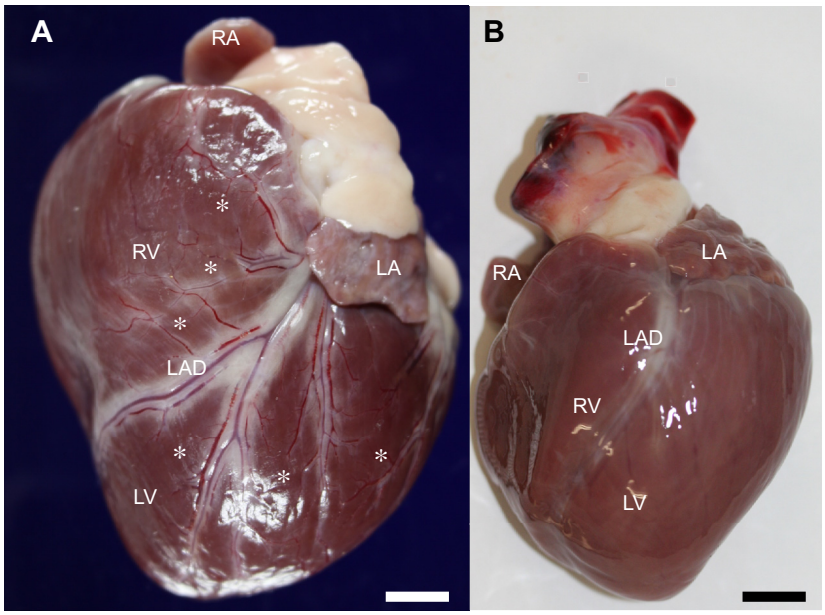

Fig. 1. Macroscopic view of coronary arteries of a beagle dog (A) and *microminipig* (B). The dog's heart has more and larger epicardial coronary arteries along with collateral networks (asterisks) than *microminipig*'s one. White and black scales indicate 1 cm. RA: right atrium; LA: left atrium; RV: right ventricle; LV: left ventricle; and LAD: left anterior descending artery.

3.1. Effects on the heart rate, blood pressure, double product and demand/supply ratio

The time courses of changes in the heart rate, systolic/diastolic blood pressures, double product and demand/supply ratio in dogs and *microminipigs* are summarized in Fig. 2 left and right panels, respectively. Their pre-drug control values (C) for dogs were 119 ± 3 beats/min, 139 ± 12/99 ± 9 mmHg, 16592 ± 1552 mmHg·beats/min, and 169 ± 9, whereas those for *microminipigs* were 87 ± 5 beats/min, 84 ± 6 and 58 ± 6 mmHg, 7255 ± 677 mmHg·beats/min and 126 ± 9, respectively. The pre-drug control values in beagle dogs and *microminipigs* were within the range that can be expected from our previous studies,[3–5,10–12] each of which was smaller in *microminipigs* than in dogs.

In dogs, the low dose of 0.056 mg/kg infusion of dipyridamole did not alter any of these variables. The high dose of 0.56 mg/kg decreased the systolic blood pressure for 10–20 min, diastolic blood pressure for 10–30 min and double product for 10–20 min, whereas no significant change was detected in the heart rate or demand/supply ratio. On the other hand, in *microminipigs*, the low and high doses decreased the systolic and diastolic blood pressures, and double product for 5–30 min and for 5–60 min, respectively, whereas no significant change was observed in the heart rate or demand/supply ratio.

Maximum changes (percent) in the systolic/diastolic blood pressures and the double product from the pre-drug control values were observed at 10 min after the high dose in both animals, which were −12/−16 mmHg (−8/−16%) and −1867 mmHg·beats/min (−11%) for dogs, and −25/−20 mmHg (−31/−34%) and −2903 mmHg·beats/min (−40%) for *microminipigs*, respectively.

3.2. Effects on the electrocardiographic variables

The time courses of changes in the PR interval, QRS width, QT interval and QTc in dogs and *microminipigs* are summarized in Fig. 3 left and right panels, respectively. Their pre-drug control values (C) for dogs were 97 ± 6, 66 ± 8, 271 ± 11 and 314 ± 10 ms, whereas those for *microminipigs* were 114 ± 3, 92 ± 3, 374 ± 7 and 400 ± 8 ms, respectively. The pre-drug control values in beagle dogs and *microminipigs* were within the range that can be expected from our previous studies[3–5,10–12] each of which was longer in *microminipigs* than in dogs, although significant difference was not detected in the PR interval.

In dogs, the low dose prolonged the QTc for 10–20 min, whereas no significant change was detected in the other variables. The high dose prolonged the QT interval and QTc for 10–30 min, whereas no significant change was detected in the other variables. Then again in *microminipigs*, the low and high doses prolonged the PR interval for 20–30 min and for 5–60 min, respectively, whereas no significant change was detected in the other variables.

3.3. Effects on the ST segment

Typical tracings of the electrocardiogram at the basal control and 10 min after the high dose are superimposed for a dog and *microminipig* in Fig. 4A, whereas the time courses of changes in the ST-segment level (ΔST) in lead II electrocardiogram are summarized in Fig. 4B. In dogs, 2 out of 4 showed downsloping morphology of ST segment, whereas the other two revealed upsloping or horizontal one, respectively at the basal control. The low dose hardly altered the ST-segment level, whereas the high dose significantly depressed it for 10–30 min. Meanwhile in *microminipigs*, 3 out of 4 showed horizontal morphology of ST segment, whereas another revealed downsloping one at the basal control. The low or high dose did not significantly alter the ST-segment level. The ST-segment depression was not also observed in the other limb leads of *microminipigs*.

4. Discussion

In this study, we tried to pharmacologically characterize the inherent vulnerability of coronary circulation of *microminipigs* in comparison with that of beagle dogs. Dipyridamole depressed the ST segment in dogs in spite of the absence of either a

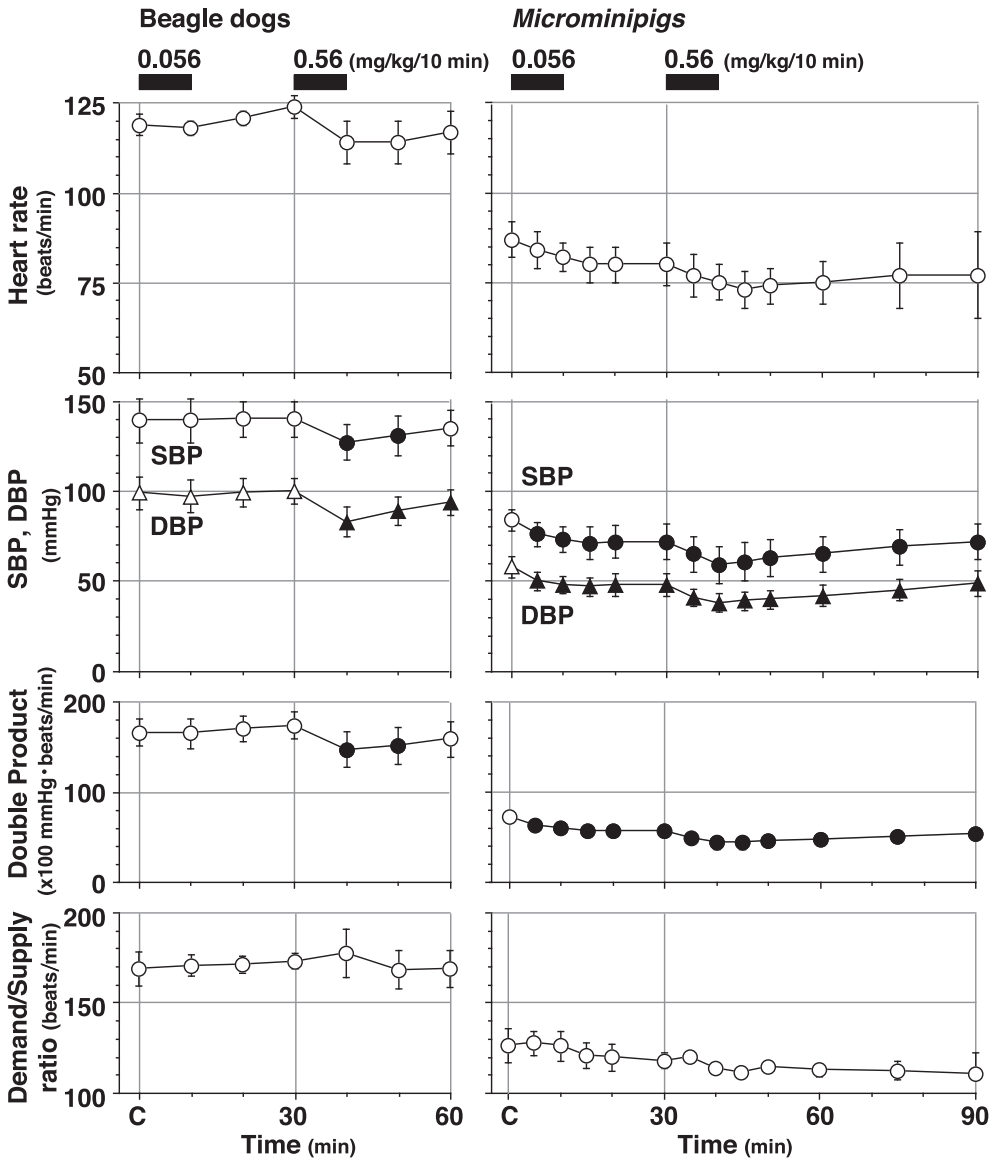

Fig. 2. The time courses of changes in the heart rate, systolic blood pressure (SBP), diastolic blood pressure (DBP), double product and double product to diastolic blood pressure ratio (Demand/Supply ratio) in beagle dogs (left panels) and *microminipigs* (right panels). Data are shown as mean ± S.E.M. (n = 4 for each animal group). The closed symbols represent significant differences from respective basal control values (C) by $P < 0.05$.

macroscopically-detectable, stenotic lesion in large coronary arteries or an imbalance between the cardiac oxygen demand and supply, but such ischemic change was not observed in *microminipigs*, indicating the presence of marked differences in the anatomical structure and functional regulation of coronary arteries between the two species.

4.1. Rationale of the dose of dipyridamole

The standard intravenous infusion doses of dipyridamole for the pharmacological stress test of ischemic heart diseases are described to be 0.56 mg/kg over 4 min or 0.75 mg/kg over 10 min during electrocardiographic monitoring.[8] We selected intravenous doses of 0.056 and 0.56 mg/kg over 10 min based on the preliminary study, although the peak plasma concentration of dipyridamole can be expected to be lower in this protocol than that achieved by the recommended ones due to longer infusion period or lower dosage. However, since blood volume/body weight was known to be 85 mL/kg in beagle dogs and 65 mL/kg in minipigs,[13] the plasma concentration might be greater in *microminipigs* than in dogs when the same dose of a drug in mg/kg basis was given and the metabolic speed of dipyridamole was similar.

4.2. Effects on the cardiohemodynamic variables

Dipyridamole decreased the systolic/diastolic blood pressures and double product in dogs as well as in *microminipigs*, but it did not significantly alter the heart rate. Hypotensive action can be considered to be induced through an activation of adenosine A_{2A} receptors.[14] In previous studies using dogs[15] and pigs[16] with dipyridamole, qualitatively similar responses were observed in the heart rate and double product to this study, although their doses, infusion speeds and anesthetics were different from ours. Currently observed, dipyridamole-induced decrements in the systolic/

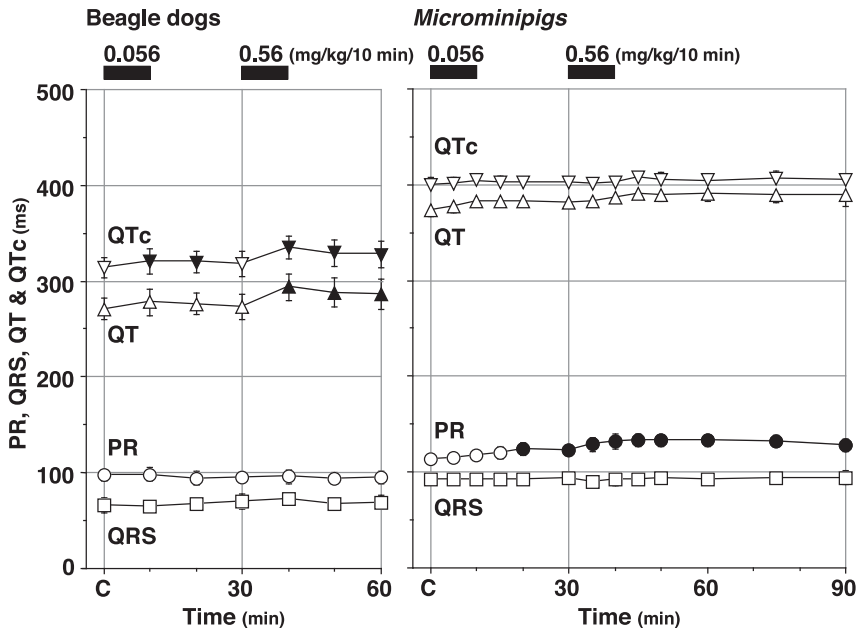

Fig. 3. The time courses of changes in the PR interval (PR), QRS width (QRS), QT interval (QT) and QT corrected by Van de Water's formula (QTc) in beagle dogs (left panels) and *microminipigs* (right panels). Data are shown as mean ± S.E.M. (n = 4 for each animal group). The closed symbols represent significant differences from respective basal control values (C) by $P < 0.05$.

diastolic blood pressures as well as the double product were greater in *microminipigs* than in dogs, although their pre-drug control values in *microminipigs* were statistically smaller than in dogs. However, the demand/supply ratio was not altered in either animal, indicating that the global balance between the myocardial oxygen demand and supply could be kept within the physiological range after the administration of dipyridamole.

4.3. Effects on the electrocardiographic variables

Dipyridamole prolonged the PR interval in *microminipigs*, which can be explained as an adenosine A_1 receptor-mediated action,[14] and in accordance with its clinically reported effect on the atrio-His conduction time.[17] In contrast, the atrioventricular nodal conduction in dogs was hardly altered by dipyridamole possibly due to the following 2 reasons. One is that the extent of hypotension-induced, reflex-mediated increase of sympathetic tone was shown to be greater in dogs than in *microminipigs*[3,4]; and the other is that the plasma drug concentration could be smaller in dogs than in *microminipigs*, as discussed above. Meanwhile, dipyridamole did not change the QRS width in dogs or *microminipigs*, indicating a lack of inhibitory actions on Na^+ channels, which is in accordance with the clinical investigation.[17] Importantly, dipyridamole prolonged the QT interval/QTc in dogs, which was not observed in *microminipigs*. Dipyridamole has been reported to hardly inhibit K^+ channels including a human ether-à-go-go related gene related K^+ channel ($IC_{50} \gg 100$ μM),[18] suggesting that the drug will not directly delay the ventricular repolarization process. One can speculate that dipyridamole-induced prolongation of the QT interval/QTc in dogs might be secondarily caused by the ST-segment depression, which could be confirmed on the tracing of electrocardiogram in Fig. 4A (left).

4.4. Effects on the ST segment

In dogs, dipyridamole depressed the ST segment of the lead II electrocardiogram, reflecting the onset of subendocardial ischemia, since the magnitude of ST-segment depression denotes the degree of subendocardial ischemia.[8,10] Meanwhile in *microminipigs*, dipyridamole did not depress the ST segment like in healthy human subjects. It has been reported that pigs have very few and small intramural collaterals which deliver little flow, but that dogs have many large and primarily epicardial collateral vessels.[19–21] Similar macroscopic findings were confirmed in beagle dogs and *microminipigs*, respectively. Thus, dipyridamole-induced subendocardial ischemia in dogs might partly depend on a so-called, coronary steal possibly through their well-developed native coronary collateral channels, suggesting that the intracoronary collaterals could not necessarily provide functional benefit in some particular conditions.

4.5. Limitation of this study

There are several limitations in this study. First, we could not directly evaluate coronary circulation after dipyridamole treatment, but just compared macroscopic anatomy of epicardial coronary arteries in canine hearts with that in *microminipig's* ones. Therefore, we may be unable to conclude with certainty that the dipyridamole-induced ST-segment depression was caused by coronary steal via larger epicardial arterial network in dogs' hearts. Second, there were some differences in QRS-complex morphology between dogs and *microminipigs* in the control condition; namely, dogs showed qR pattern, whereas *microminipigs* showed rS pattern. It has been reported that Purkinje-ventricular junctions can be identified only in subendocardium in humans, dogs and rabbits, whereas they may be present transmurally in sheep and pigs.[22] Also, there was a marked difference in apical shape of the heart between dogs and *microminipigs*, which was round in the former, but was prominent in the latter, as shown Fig. 1. These electrophysiological and morphological differences may partly explain the characteristics of QRS-complex morphology of each animal, which might have affected the direct comparison of ST-segment level. Third, it would be possible that a downsloping ST depression was secondary to T-wave change induced by dipyridamole, although T-

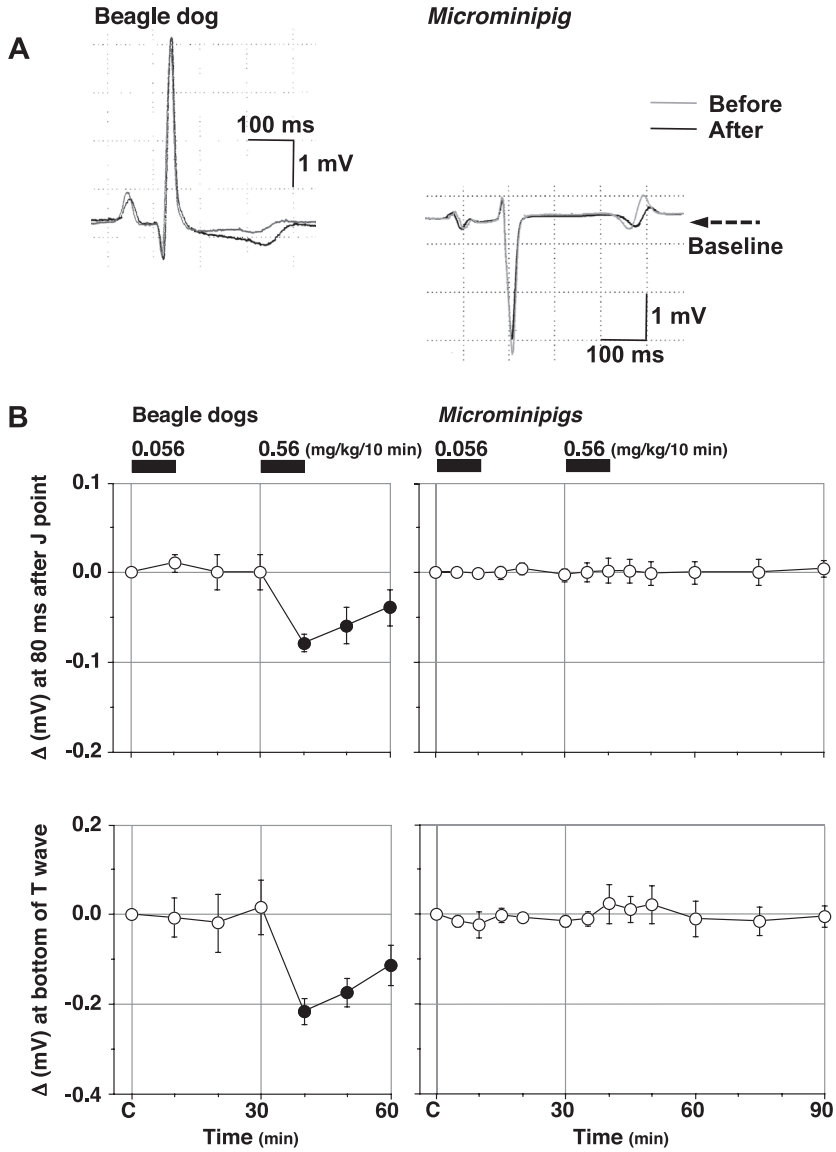

Fig. 4. Effects of dipyridamole on the ST-segment level. (A) Typical tracings of the lead II electrocardiogram in a beagle dog (left panel) and *microminipig* (right panel) before (gray) and 10 min (black) after the start of infusion of 0.56 mg/kg of dipyridamole. (B) The time courses of changes in the ST-segment level (Δ) are summarized. Note that significant depression of ST-segment level was observed in dogs, which was not observed in *microminipigs*. Data are shown as mean ± S.E.M. (n = 4 for each animal group). The closed symbols represent significant differences from respective basal control values (C) by $P < 0.05$.

wave change by itself may also reflect the myocardial ischemia. Finally, since we usually performed pharmacological assessments in these animals >2 h after the induction of general anesthesia to confirm the stability of cardiohemodynamic condition, we suppose that the initially administered pre-anesthetic agents may hardly influence the basal hemodynamic parameters just before the administration of drugs. However, we cannot totally rule out the possibility that the pre-anesthetic agents might have affected the basal values of hemodynamic parameters in these animals from the results of this study.

5. Conclusion

The ST segment was not depressed in intact *microminipigs* by the dipyridamole-stress test like in healthy human subjects, suggesting favorable invulnerability against the dipyridamole administration and their similarity in anatomical structure and functional regulation of coronary arteries. Meanwhile, dipyridamole depressed the ST segment in normal dogs unlike in intact *microminipigs*, indicating that the well-developed native coronary collateral channels in dogs might have played some roles in the onset of myocardial ischemia as inherent vulnerability of coronary circulation. Thus, *microminipigs* would be more useful to evaluate the drugs which may affect the coronary circulation in the pre-clinical study than dogs.

Conflict of interest statement

The authors declare no conflicts of interest.

Acknowledgments

This study was supported in part by JSPS KAKENHI Grant number JP16K08559 and AMED Grant number AS2116907E. The

authors thank Dr. Yoshioki Satoh, Dr. Hiroshi Iwasaki, Dr. Hiro Eda, Dr. Katsuhito Kashiwagi, Ms. Misako Nakatani and Mrs. Yuri Ichikawa for their technical assistance.

References

1. Kaneko N, Itoh K, Sugiyama A, Izumi Y. Microminipig, a non-rodent experimental animal optimized for life science research: preface. *J Pharmacol Sci*. 2011;115:112–114.
2. Sugiyama A, Nakamura Y, Akie Y, et al. Microminipig, a non-rodent experimental animal optimized for life science research. In vivo proarrhythmia models of drug-induced long QT syndrome: development of chronic atrioventricular block model of microminipig. *J Pharmacol Sci*. 2011;115:122–126.
3. Yokoyama H, Nakamura Y, Saito H, et al. Pharmacological characterization of microminipig as a model to assess the drug-induced cardiovascular responses for non-clinical toxicity and/or safety pharmacology studies. *J Toxicol Sci*. 2017;42:93–101.
4. Matsukura S, Nakamura Y, Cao X, et al. Characterization of microminipigs as an in vivo experimental model for cardiac safety pharmacology. *J Pharmacol Sci*. 2017;133:103–109.
5. Cao X, Wada T, Nakamura Y, et al. Sensitivity and reliability of halothane-anesthetized microminipigs to assess risk for drug-induced long QT syndrome. *Basic Clin Pharmacol Toxicol*. 2017;121:465–470.
6. Matsukura S, Nakamura Y, Ohara H, et al. Feasible induction of coronary artery vasospasm occurred during cardiac catheterization in a microminipig. *J Vet Med Sci*. 2016;78:873–876.
7. Cao X, Nakamura Y, Aoki T, et al. Coronary artery vasospasms in a *microminipig* occurred after placing an ameroid constrictor. *J Vet Med Sci*. 2016;78:1213–1216.
8. Ellestad MH. *Stress testing, principles and practice*. 4th ed. Philadelphia, PA: F.A. Davis Company; 1996.
9. Van de Water A, Verheyen J, Xhonneux R, Reneman RS. An improved method to correct the QT interval of the electrocardiogram for changes in heart rate. *J Pharmacol Methods*. 1989;22:207–217.
10. Sugiyama A, Hashimoto K. Antiischemic effects of CP-060S, an inhibitor of pathologically modified sodium channels, assessed in the canine experimental model of angina pectoris. *J Cardiovasc Pharmacol*. 1999;33:70–77.
11. Sugiyama A. Sensitive and reliable proarrhythmia in vivo animal models for predicting drug-induced torsades de pointes in patients with remodelled hearts. *Br J Pharmacol*. 2008;154:1528–1537.
12. Matsukura S, Nakamura Y, Cao X, et al. Anti-atrial fibrillatory versus proarrhythmic potentials of amiodarone: a new protocol for safety evaluation in vivo. *Cardiovasc Toxicol*. 2017;17:157–162.
13. Diehl KH, Hull R, Morton D, et al. A good practice guide to the administration of substances and removal of blood, including routes and volumes. *J Appl Toxicol*. 2001;21:15–23.
14. Layland J, Carrick D, Lee M, Oldroyd K, Berry C. Adenosine: physiology, pharmacology, and clinical applications. *JACC Cardiovasc Interv*. 2014;7:581–591.
15. Sakanashi M, Noguchi K, Kato T, et al. Investigation on the effect of dipyridamole and papaverine on regional blood flow and cardiac hemodynamics in anesthetized dogs. *Arzneimittelforschung*. 1989;39:1119–1123.
16. Segar DS, Ryan T, Sawada SG, Johnson M, Feigenbaum H. Pharmacologically induced myocardial ischemia: a comparison of dobutamine and dipyridamole. *J Am Soc Echocardiogr*. 1995;8:9–14.
17. Bubiński R, Markiewicz K, Cholewa M, Górski L, Gawor Z, Kuś W. Electrophysiologic effects of intravenous dipyridamole. *Int J Cardiol*. 1989;24:327–335.
18. Yunomae K, Ichisaki S, Matsuo J, et al. Effects of phosphodiesterase (PDE) inhibitors on human ether-a-go-go related gene (hERG) channel activity. *J Appl Toxicol*. 2007;27:78–85.
19. Eckstein RW. Coronary interarterial anastomoses in young pigs and mongrel dogs. *Circ Res*. 1954;2:460–465.
20. Patterson RE, Kirk ES. Analysis of coronary collateral structure, function, and ischemic border zones in pigs. *Am J Physiol*. 1983;244:H23–H31.
21. Bertho E, Gagnon G. A comparative study in three dimension of the blood supply of the normal interventricular septum in human, canine, bovine, porcine, ovine and equine heart. *Dis Chest*. 1964;46:251–262.
22. Lelovas PP, Kostomitsopoulos NG, Xanthos TT. A comparative anatomic and physiologic overview of the porcine heart. *J Am Assoc Lab Anim Sci*. 2014;53:432–438.

Journal of Pharmacological Sciences 136 (2018) 93–96

Contents lists available at ScienceDirect

Journal of Pharmacological Sciences

journal homepage: www.elsevier.com/locate/jphs

Short communication

LPA5 signaling is involved in multiple sclerosis-mediated neuropathic pain in the cuprizone mouse model

Ryoko Tsukahara [a], Shinji Yamamoto [b], Keisuke Yoshikawa [b], Mari Gotoh [c, d], Tamotsu Tsukahara [a], Hiroyuki Neyama [a], Satoshi Ishii [e], Noriyuki Akahoshi [e], Keisuke Yanagida [f], Hayakazu Sumida [f], Masatake Araki [g], Kimi Araki [g], Ken-ichi Yamamura [g], Kimiko Murakami-Murofushi [c], Hiroshi Ueda [a, *]

[a] Department of Pharmacology and Therapeutic Innovation, Nagasaki University Graduate School of Biomedical Sciences, Nagasaki, Japan
[b] Department of Pharmacology, Faculty of Medicine, Saitama Medical University, Saitama, Japan
[c] Endowed Research Division of Human Welfare Sciences, Ochanomizu University, Tokyo, Japan
[d] Institute for Human Life Innovation, Ochanomizu University, Tokyo, Japan
[e] Department of Immunology, Akita University Graduate School of Medicine, Akita, Japan
[f] Department of Biochemistry and Molecular Biology, Graduate School of Medicine, The University of Tokyo, Tokyo, Japan
[g] Institute of Resource Development and Analysis, Kumamoto University, Kumamoto, Japan

ARTICLE INFO

Article history:
Received 13 September 2017
Received in revised form
29 December 2017
Accepted 9 January 2018
Available online 2 February 2018

Keywords:
LPA5
Neuropathic pain
Multiple sclerosis

ABSTRACT

Lysophosphatidic acid (LPA) and LPA1 receptor signaling play a crucial role in the initiation of peripheral nerve injury-induced neuropathic pain through the alternation of pain-related genes/proteins expression and demyelination. However, LPA and its signaling in the brain are still poorly understood. In the present study, we revealed that the LPA5 receptor expression in corpus callosum elevated after the initiation of demyelination, and the hyperalgesia through Aδ-fibers following cuprizone-induced demyelination was mediated by LPA5 signaling. These data suggest that LPA5 signaling may play a key role in the mechanisms underlying neuropathic pain following demyelination in the brain.

© 2018 The Authors. Production and hosting by Elsevier B.V. on behalf of Japanese Pharmacological Society. This is an open access article under the CC BY-NC-ND license (http://creativecommons.org/licenses/by-nc-nd/4.0/).

Lysophosphatidic acid (LPA), one of lipid mediators, was identified as a key initiator of neuropathic pain via activation of multiple signaling pathways in peripheral nerve system.[1] LPA and LPA1 receptor signaling initiate the neuropathic pain following partial sciatic nerve ligation in mice.[1] LPA1 signaling is also involved in the demyelination of dorsal roots and upregulation of pain-related genes/proteins such as calcium channel α2δ1, ephrinB1, and protein kinase Cγ.[1,2] Besides, it has been reported that LPA5-mediated signaling plays a role in the development of neuropathic pain after peripheral nerve injury.[3] Murai et al. also reported that LPA5 signaling transmits pain signals in the spinal cord.[4] However, the mechanisms of LPA signaling underlying demyelination as well as neuropathic pain in the brain are still unclear.

Multiple sclerosis (MS) is a chronic autoimmune disorder affecting the CNS through demyelination and neurodegeneration.[5] It has been reported that closely-related bioactive lipid, sphingosine 1-phosphate (S1P) and its signaling are involved in the progression of demyelination in MS.[6] S1P receptor modulator fingolimod (FTY720) is currently approved for the treatment of MS, which inhibits S1P signaling results in ameliorating demyelination in patients with MS.[6] However, the mechanisms of neuropathic pain following demyelination in MS are not fully understood. This led us to hypothesize that LPA signaling may be associated with neuropathic pain in MS. In this study, we investigated whether LPA signaling is involved in neuropathic pain in MS using cuprizone (CPZ)-induced MS model.[7]

For animal study, C57BL/6J mice were obtained from TEXAM corporation (Nagasaki, Japan). To generate *Lpar5*-KO mice, we used a gene trap clone (Ayu21-B206) of KTPU8 mouse embryonic stem cells, in which the trap vector pU-21B is integrated into *Lpar5*.[8] In the Ayu21-B206 clone (http://egtc.jp/action/access/clone_detail?id=21-B206), 5′-RACE data showed the trap vector pU-21B was integrated into the first intron upstream of the open reading frame-containing exon of *Lpar5*. The precise genomic integration site of pU-21B was determined by long PCR and sequencing. Sequence comparison with the assembled mouse genome revealed that the integration occurred in the first intron of *Lpar5* at chr6:

* Corresponding author. Department of Pharmacology and Therapeutic Innovation, Graduate School of Biomedical Sciences, Nagasaki University, 1-14 Bunkyo–machi, Nagasaki 852-8521, Japan. Fax: +81 95 819 2420.
E-mail address: ueda@nagasaki-u.ac.jp (H. Ueda).
Peer review under responsibility of Japanese Pharmacological Society.

https://doi.org/10.1016/j.jphs.2018.01.001
1347-8613/© 2018 The Authors. Production and hosting by Elsevier B.V. on behalf of Japanese Pharmacological Society. This is an open access article under the CC BY-NC-ND license (http://creativecommons.org/licenses/by-nc-nd/4.0/).

125078165 (GRCm38/mm10). We established a mouse line (B6; CB-*Lpar5*$^{Gt(pU-21B)206Imeg}$) from the Ayu21-B206 clone. Then, mice were backcrossed to the C57BL/6N background for 8 generations. With genomic DNA from tail biopsies, mice were genotyped by PCR for *Lpar5* alleles. The PCR primers for detection of the *Lpar5* WT allele were 5′-gtttatctgtacaccagacagc-3′ and 5′-gacaggctaatgctacgcttg-3′, and those for the *Lpar5*-KO allele were 5′-gtttatctgtacaccagacagc-3′ and 5′-cacatccatgctgaggatgag-3′, yielding 457- and 490-bp products, respectively. Mice used in this study were kept in a room maintained at 21 ± 2 °C and 55 ± 5% relative humidity with a 12 h light/dark cycle. All animal experiments were approved by the Nagasaki University Animal Care Committee, and complied with the fundamental guidelines for the proper conduct of animal experiments and related activities in academic research institutions under the jurisdiction of the Ministry of Education, Culture, Sports, Science and Technology, Japan.

As for CPZ model, mice were fed ad libitum a powdered diet (CLEA Japan, Tokyo) containing 0.2% bis-cyclohexanone oxaldihydrazone (cuprizone; Merck KGaA, Darmstadt, Germany) for 5 weeks. Mice were euthanized, and tissue from the corpus callosum was collected for RNA extraction as previously reported.[9] For histology, mice were intracardially perfused with 4% paraformaldehyde in phosphate buffered saline (PBS). Brains were postfixed overnight in 4% paraformaldehyde in PBS, and subsequently cryoprotected in 30% sucrose solution in PBS.

For quantitative real-time PCR (Q-PCR), RNA was extracted from the corpus callosum (n = 6 per group) using ISOGEN (NIPPON GENE CO, Japan) following the manufacturer's instructions. The extracted RNA was reverse transcribed using a PrimeScript RT reagent kit (TAKARA BIO INC, Japan). Q-PCR was performed using the 7900 Sequence Detection System (Applied Biosystems) with the following conditions: 95 °C for 30 s, followed by 40 cycles of 5 s at 95 °C and 34 s at 60 °C. The primer sets used for Q-PCR were as follows: phosphoglycerate kinase 1 (PGK1) forward: 5′-ctgctgttccaagcatcaaa-3′ and reverse: 5′-gcatcttttcccttcccttc-3'; *Lpar1* forward: 5′-caccagcctgacagcttct-3′ and reverse: 5′-ctgtagaggggtgccatgtt-3'; *Lpar2* forward: 5′-tctccatcaaaggctggttc-3′ and reverse: 5′-tccaagtcacagaggcagtg-3'; *Lpar3* forward: 5′-ctggccaatttgctggttat-3′ and reverse: 5′-tgaagaaggccaggaggtt-3'; *Lpar4* forward: 5′-aacctggccctctctgattt-3′ and reverse: 5′-cgatcggaagggatagacaa-3'; *Lpar5* forward: 5′-tcagcgatgaactgtggaag-3′ and reverse: 5′-acgaagcacagcaggaagat-3'; *Lpar6* forward: 5′-tcatctgtgccctcaaagtg-3′ and reverse: 5′-cacagcaatgcaaacgatct-3'. The gene expression was calculated by using ΔΔCT method. The results were normalized to the expression levels of PGK1. Relative changes in gene expression were described as a percentage of the expression in control.

To evaluate the paw withdrawal response, electrical stimulation-induced paw withdrawal (EPW) test was performed. Electrical stimuli with a frequency of 5, 250, and 2000 Hz were applied to the right hindpaw to activate C-, Aδ-, and Aβ-fibers, respectively.[10] Electrodes were fastened to the plantar and insteps of mice. Transcutaneous nerve stimuli with each of the three sine-wave pulses were applied using a Neurometer CPT/C system (Neurotron Inc., Baltimore, MD). The minimum intensity (μA) at which each mouse withdrew its paw was defined as the current stimulus threshold.

For histological analysis, coronal brain sections (25 μm thick) were cut on a cryostat (LEICA CM1900, Wetzlar, Germany). Sections were stained for myelin using Black Gold II (Histo-Chem, Jefferson,

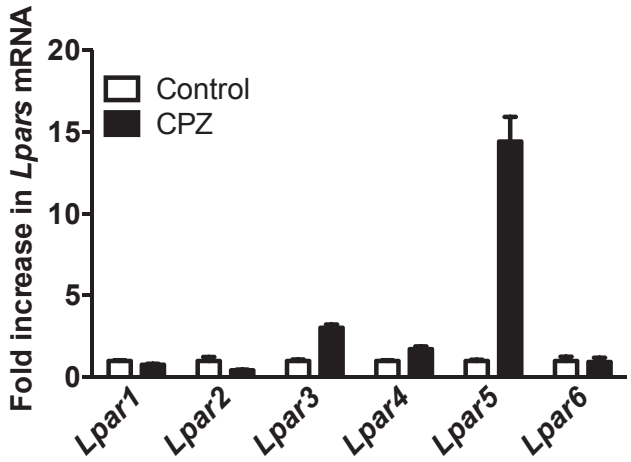

Fig. 1. The expression level of LPA receptors in corpus callosum. The expression levels of LPA receptors (*Lpar1-6*) were determined by Q-PCR in corpus callosum before and after 5-weeks cuprizone (CPZ) exposure.

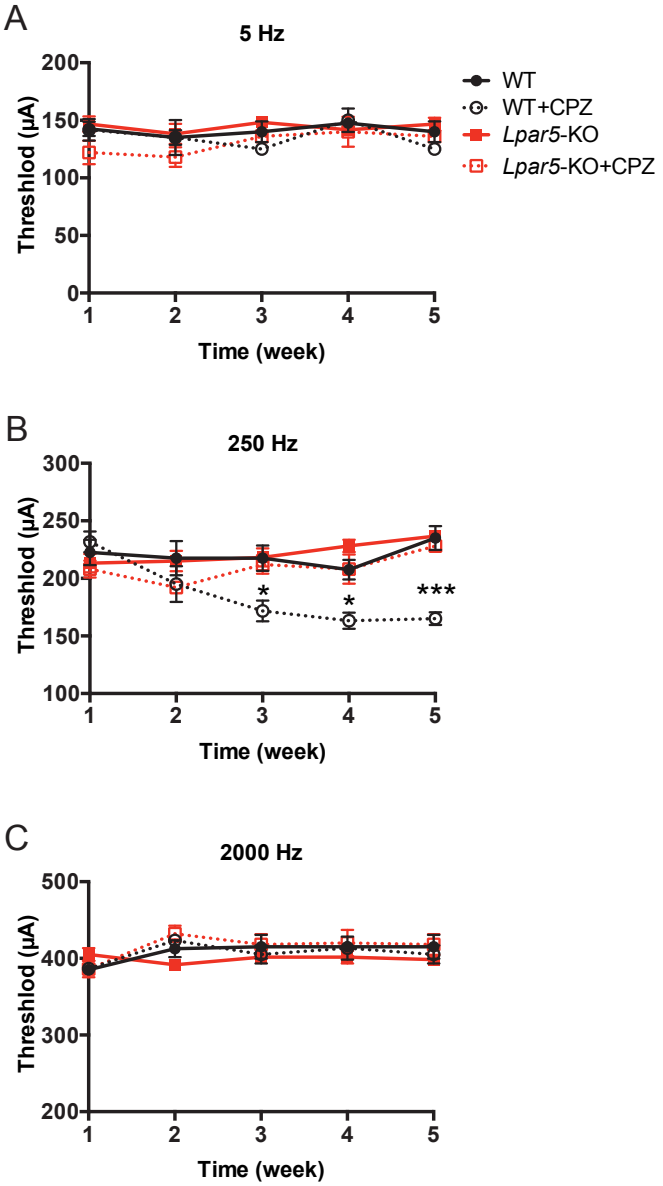

Fig. 2. LPA5 receptor signaling was involved in neuropathic pain through the stimulation of Aδ-fiber. The threshold levels were measured every week after CPZ-exposure in WT and *Lpar5*-KO mice as well as WT and *Lpar5*-KO mice with normal diet using EPW test. The values represent the minimum intensity (μA) required to produce a paw withdrawal response to electrical stimulation with 5 Hz for C-fiber (A), 250 Hz for Aδ-fiber (B), and 2000 Hz for Aβ– fiber (C). *$p < 0.05$ (versus WT). ***$p < 0.001$ (versus WT).

AR) according the manufacturer's instructions.[11] The stained sections were selected between Bregma −0.22 mm and −0.58 mm, and photographed at 10× magnification on KEYENCE BZ-X700 microscope (Keyence Corporation, Japan). Images were imported into ImageJ 1.46r to measure the mean optical density (OD) within the middle of the corpus callosum. The OD of the tissue-free area was used as a background. The resulting ODs for myelin in each mouse were normalized against values in unchallenged mice using the following formula: myelin score (%) = (density reading/unchallenged density average) × 100.

The data were analyzed by one-way ANOVA followed by Newman–Keuls post hoc test or two-way ANOVA followed by Dunnett's test using GraphPad Prism (Graphpad Software Inc.). The results were expressed as the mean ± SEM.

We first investigated whether demyelination in the brain affects the expression of LPA receptors (*Lpar1-6*) using CPZ-induced demyelination model mice. As shown in Fig. 1, the expression level of *Lpar5* in the corpus callosum markedly increased about 15-fold after CPZ-exposure for 5 weeks. Less increase was observed in *Lpar3* and *Lpar4* expression, while there was no increase in *Lpar1*, *Lpar2* and *Lpar6* expression.

It is known that several neuropathies including MS are accompanied with demyelinating disorders in CNS.[12] To examine whether CPZ-induced demyelination causes neuropathic pain, we performed the pain behavioral study in the EPW test using three different frequencies of electrical stimulation. As shown in Fig. 2, significant decrease in the pain threshold to 250 Hz (Aδ-fibers) stimulation started at 2 weeks and reached maximum at 3–5 weeks after CPZ-exposure, while there was no significant change in the threshold to 5 or 2000 Hz in WT mice. In *Lpar5*-KO mice, on the other hand, the hyperalgesia to 250 Hz stimulation was abolished, while no change was observed in the case with 5 and 2000 Hz. These results indicate that CPZ-mediated demyelination and LPA5-mediated signaling are correlated with the hyperalgesia through Aδ-fibers.

Next, we examined the effect of LPA5 receptor on the progression of demyelination using *Lpar5*-KO mice, since *Lpar5* expression was elevated after CPZ exposure. We fed CPZ-containing diet to the mice for 5 weeks, and myelin content in the corpus callosum was quantified using Black-Gold II staining. In WT mice, the corpus callosum appeared to retain sufficient myelin content (Fig. 3A). In contrast, WT mice exposed to CPZ showed demyelination in the corpus callosum (Fig. 3B). Similarly, *Lpar5*-KO mice with CPZ diet

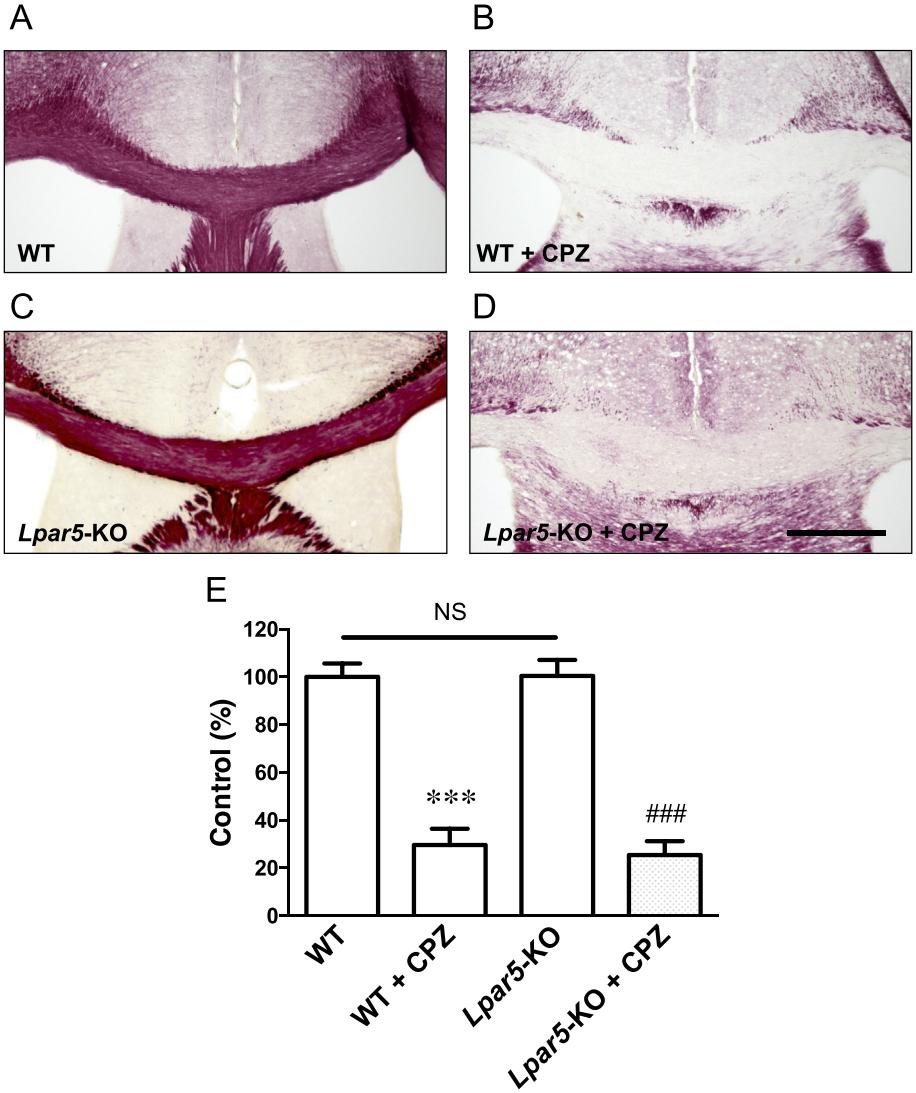

Fig. 3. LPA5 had no effect on the CPZ-induced demyelination. Representative images of coronal brain sections at the level of the fimbria demonstrate progressive demyelination in the corpus callosum after 5 weeks of CPZ-exposure. Black-Gold II staining was performed in WT (A), WT + CPZ (B), *Lpar5*-KO (C), and *Lpar5*-KO + CPZ (D) groups. Myelin densities in the corpus callosum were compared with those of controls and expressed as a percentage using the ImageJ analysis program (E). Data represent mean ± SEM. N = 4 for WT, n = 5 for *Lpar5*-KO + CPZ, and n = 6 for WT + CPZ and *Lpar5*-KO. Scale bar = 500 mm ***$p < 0.001$ (versus WT) and ###$p < 0.001$ (versus *Lpar5*-KO). NS means no significant.

showed demyelination and the degree of demyelination was equivalent to that in WT mice (Fig. 3D and E). These results indicate that LPA5 has no effect on the progression of demyelination induced by CPZ.

In this study, we found that the hyperalgesia through Aδ-fibers followed by CPZ-induced demyelination is mediated by LPA5 signaling, while LPA5 has no effect on the progression of demyelination in the corpus callosum in CPZ-induced MS model. CPZ is reported to cause a selective toxicity to mature oligodendrocytes leading to apoptosis and demyelination in the brain.[13] As no significant change was observed in the basal threshold to 2000 Hz (Aβ-fibers)-stimulation (Fig. 2C), it is unlikely that CPZ affects the peripheral myelinated fibers in terms of sensory threshold. The present findings that LPA5 is involved in the hyperalgesia, but not in the cause of demyelination in the MS model, are consistent with the report that *Lpar5*-KO mice lose the peripheral neuropathic pain following partial sciatic nerve ligation, but do not affect the demyelination of dorsal root.[2] Regarding the source of LPA, there are reports that the protein level and enzyme activity of LPA-producing enzyme autotaxin are elevated in the cerebrospinal fluid of MS patients.[14,15] As such, it is interesting to speculate that both upregulated LPA5 expression and demyelination-related increase in brain LPA levels are involved in the CPZ-induced LPA5-mediated neuropathic pain. We have proposed the hypothesis that LPA5-mediated hyperalgesia in mice with peripheral nerve injury may be related to the phosphorylation of cAMP response element–binding protein,[2] followed by the up-regulation of brain-derived neurotrophic factor and down-regulates KCC2 levels and exerts a functional switch of the GABA/glycine receptor from inhibitory to stimulatory.[16] Further study to examine whether LPA is produced by CPZ-induced demyelination and LPA5 mediates the BDNF up-regulation will be required as the next subject.

Conflict of interest

All authors declare no conflict of interest.

Acknowledgement

This study was supported in part by Grants-in-Aid for Scientific Research (A) on Innovative Areas from the Ministry of Education, Culture, Sports, Science and Technology, Japan (26253077) (to HU), and the Platform for Drug Discovery, Informatics, and Structural Life Science project supported by the Japan Agency for Medical Research and Development (16am0101012j0005) (to HU). We acknowledge EGCT, Kumamoto University as a source of *Lpar5*-KO mice.

References

1. Inoue M, Rashid MH, Fujita R, Contos JJ, Chun J, Ueda H. Initiation of neuropathic pain requires lysophosphatidic acid receptor signaling. *Nat Med*. 2004;10(7):712–718.
2. Ueda H. Lysophosphatidic acid signaling is the definitive mechanism underlying neuropathic pain. *Pain*. 2017;158(Suppl 1):S55–S65.
3. Lin ME, Rivera RR, Chun J. Targeted deletion of LPA5 identifies novel roles for lysophosphatidic acid signaling in development of neuropathic pain. *J Biol Chem*. 2012;287(21):17608–17617.
4. Murai N, Hiyama H, Kiso T, et al. Analgesic effects of novel lysophosphatidic acid receptor 5 antagonist AS2717638 in rodents. *Neuropharmacology*. 2017;126:97–107.
5. Bramow S, Frischer JM, Lassmann H, et al. Demyelination versus remyelination in progressive multiple sclerosis. *Brain*. 2010;133(10):2983–2998.
6. Groves A, Kihara Y, Chun J. Fingolimod: direct CNS effects of sphingosine 1-phosphate (S1P) receptor modulation and implications in multiple sclerosis therapy. *J Neurol Sci*. 2013;328(1–2):9–18.
7. Torkildsen O, Brunborg LA, Myhr KM, Bo L. The cuprizone model for demyelination. *Acta Neurol Scand Suppl*. 2008;188:72–76.
8. Araki M, Nakahara M, Muta M, et al. Database for exchangeable gene trap clones: pathway and gene ontology analysis of exchangeable gene trap clone mouse lines. *Dev Growth Differ*. 2014;56(2):161–174.
9. Taylor LC, Puranam K, Gilmore W, Ting JP, Matsushima GK. 17beta-estradiol protects male mice from cuprizone-induced demyelination and oligodendrocyte loss. *Neurobiol Dis*. 2010;39(2):127–137.
10. Matsumoto M, Xie W, Ma L, Ueda H. Pharmacological switch in Abeta-fiber stimulation-induced spinal transmission in mice with partial sciatic nerve injury. *Mol Pain*. 2008;4:25.
11. Yamamoto S, Yamashina K, Ishikawa M, et al. Protective and therapeutic role of 2-carba-cyclic phosphatidic acid in demyelinating disease. *J Neuroinflammation*. 2017;14(1):142.
12. O'Connor AB, Schwid SR, Herrmann DN, Markman JD, Dworkin RH. Pain associated with multiple sclerosis: systematic review and proposed classification. *Pain*. 2008;137(1):96–111.
13. Kipp M, Clarner T, Dang J, Copray S, Beyer C. The cuprizone animal model: new insights into an old story. *Acta Neuropathol*. 2009;118(6):723–736.
14. Hammack BN, Fung KY, Hunsucker SW, et al. Proteomic analysis of multiple sclerosis cerebrospinal fluid. *Mult Scler*. 2004;10(3):245–260.
15. Zahednasab H, Balood M, Harirchian MH, Mesbah-Namin SA, Rahimian N, Siroos B. Increased autotaxin activity in multiple sclerosis. *J Neuroimmunol*. 2014;273(1–2):120–123.
16. Coull JA, Beggs S, Boudreau D, et al. BDNF from microglia causes the shift in neuronal anion gradient underlying neuropathic pain. *Nature*. 2005;438(7070):1017–1021.